On the estimation of near-surface atmospheric refraction using scanning radar

Shinju Park

Degree of Doctor of Philosophy

Department of Atmospheric and Oceanic Sciences
McGill University

Montreal, Quebec, Canada

October, 2010

A thesis submitted McGill University in partial fulfillment of the requirements of the degree of Doctor of Philosophy

DEDICATION

"Determined and persistent"

-anonymous but Ph.D-

사랑하는 부모님께, i pel Marc

To the audience in Burnside 825

ABSTRACT

Near-surface atmospheric refraction, often characterized by the quantity refractivity, affects the propagation of the radar beam, yet it is poorly measured due to its complex pattern. The aim of this thesis is to characterize the structure of near-surface refractivity and its errors.

The refractivity retrieval in the horizontal is obtained from the radar phase measurements that can be affected systematically by the variability of ground target heights over complex terrain coupled with propagation conditions. This study characterizes such factors statistically and reproduces the expected uncertainty (noisiness) by simulating phase for the assessment of the radar refractivity retrieval. However, the noisiness of simulated phase is much smaller compared with that of observations suggesting that such factors are incapable of characterizing moving ground targets and thus insufficient to fully explain the phase noisiness.

The vertical structure of refractivity is, on the other hand, characterized in order to inform about low-level propagation conditions. The coverage of radar ground echo observed at low elevation angles is affected by the path of the radar beam determined with the vertical gradient of refractivity. Hence, this study simulates the coverage of ground targets with given vertical gradient of refractivity and compares it with the observed one. The best match between the simulation and observation is used to determine the radar estimate of refractivity changes in the vertical. The results are validated with the estimates from several sounding instruments. Although the identification of ground targets is required for better performance, this novel technique shows certain skill in extracting additional low-level atmospheric information out of radar measurements from ground targets.

In both studies, the characterization of ground targets observed by radar plays a critical role: on one hand, it allows us to extract the structure of the near-ground refractivity, but on the other hand it limits the quality of the refractivity retrieval and the estimation of the vertical gradient of refractivity.

ABRÉGÉ

Près de la surface terrestre, la réfraction atmosphérique affecte la propagation des ondes radars. Cette caractéristique de l'atmosphère, qu'on nomme la réfractivité, est spatialement complexe et mal connue. Dans cette thèse, la structure de la réfractivité ainsi que ses erreurs sont caractérisés.

La réfractivité est mesurée à partir du déphasage des échos radars provenant de cibles terrestres. Ce déphasage est une fonction de la complexité du terrain ainsi que des conditions de propagations. Ces deux facteurs sont analysés statistiquement afin de simuler l'incertitude attendue (le bruit) de la phase des échos radars affectant les mesures de réfractivité. Les simulations ainsi conduites possèdent un niveau de bruit sur la phase beaucoup plus petit que celui des mesures instrumentales. Cette observation suggère que le bruit sur la phase causé par le terrain et les conditions de propagation a un impact limité sur les mesures de réfractivité comparé au bruit provenant d'autres sources tel que les cibles mobiles.

Dans un deuxième temps, la structure verticale de la réfractivité est étudiée afin de déduire les conditions de propagation en basse altitude. L'étendue des échos de sol observés à faibles élévations est affectée par la trajectoire des ondes radars qui à son tour est affectée par le gradient vertical de la réfractivité. Cette étude simule l'étendue des échos de sols en supposant différents gradients de réfractivité. Les gradients qui mènent à la meilleure ressemblance entre l'étendue des échos simulée et observée sont utilisés pour estimer les gradients réels de l'atmosphère. La validation des résultats est ensuite faite par comparaison avec d'autres instruments. Malgré le fait que les échos de sols doivent être identifiés pour une performance optimale, cette nouvelle technique démontre la possibilité d'inférer de nouvelles informations sur l'atmosphère en basse altitude à partir d'échos radars provenant de cibles terrestres.

Dans ces deux études, la caractérisation des échos de sols joue un rôle critique: d'une part, elle permet de déduire la structure de la réfractivité près de la surface, d'une autre elle impose des limites sur la performance des algorithmes de mesures de réfractivité et de son gradient vertical.

CONTRIBUTION OF AUTHORS

Chapters 2-3 consist of papers published and submitted to the *Journal of Atmospheric and Oceanic Technology.* These manuscripts present the research I have performed for my Ph.D and are co-authored by Frédéric Fabry. As my supervisor, he contributed to the proposed research through numerous discussions and edited each manuscript several times.

STATEMENT OF ORIGINALITY

The contributions of this thesis to original knowledge are:

- For the first time, the error sources of the refractivity retrieval algorithm are systematically examined. When the algorithm uses phase measurement returned from ground targets for the retrieval, several unrealistic factors are assumed. Little research has been done on these factors that can affect real phase measurements. In this paper, two accessible sources are used for testing their sensitivity to phase uncertainty: *the variation of target heights over complex terrain and propagation conditions.*
- To quantify the uncertainty of phase observation, *phase simulation is performed for the first time by including the factors mentioned above into the original algorithm.* This framework also provides an easy way to validate the simulated results with observed ones.
- The simulation of radar phase measurements required *a statistical generation of ground targets within the radar domain and at the resolution of the bin.* This is based on the analysis of ground echo intensity maps. Intensity is obtained from the analysis of the raw signal and averaged [in terms of what is referred here as the "Norm of I and Q (*NIQ*)"] to amplify the stationary feature of ground targets. *Such attempt in quantifying ground echo intensity spurred new signal processing techniques by several independent researches to improve the identification of ground targets that is required for radar data quality control.* Because *NIQ* is a more primitive quantity to indicate the signal coherency, it does not always succeed in the identification of ground. *Nevertheless, this study still shows its usefulness for the first time.*

- *Propagation conditions at surface level are uniquely obtained from ground echo observation at 0° elevation angle.* Although such low-level radar scans contain echoes with meteorological value, their use is limited due to the contamination of ground echoes and thus avoided. *This study shows an alternative way of using ground echoes to extract atmospheric information near the surface* that is usually sampled at very coarse resolutions from expensive conventional measurements.
- For the robust validation of radar estimated low-level propagation conditions, various instrument estimates are intercompared. And the *impact of such propagation conditions on the positioning of the radar beam has been systematically evaluated during the experiment IHOP_2002.*

ACKNOWLEDGMENTS

First of all, I would like to thank my supervisor, Frédéric Fabry for his genuine and encouraging guidance on the research as well as for his financial support awarded from the Canadian Foundation for Climate and Atmospheric Sciences. Special thanks go to Isztar Zawadzki who challenged me with very fundamental and insightful questions on the research and presenting skills during the group meetings, and Marc Berenguer who patiently listened and provided feedback on scientific, technical and writing problems.

I want to thank the audiences who attended the radar group meetings, whose comments and interaction were enjoyable and sometimes painful; however, in the end, it was for sure fruitful. Special thanks to Barry Turner, Wanda Szyrmer, Kaoshen Chung, and Gyuwon Lee as well as Aldo Bellon and Alamelu Kilambi for their encouragement and feedback.

Although I stayed most of time at Burnside Hall, I had met many and great friends who took me out of the building and shared the fun life. Thanks especially to Lily Ioannidou, Barbara Winter, Irena Ivanova, Charmaine Franklin, Keith Ngan, Catherine Heyraud.

Most of the analysis in the thesis was performed with data collected from the IHOP_2002 field experiment. I would like to thank Frédéric for providing me the chance to participate in this great opportunity and meeting many people in the same research area. Among others, I enjoyed meeting Rita Roberts, James Wilson, Tammy Weckwerth, and Alan Seed who encouraged me during several conferences.

During the wrapping up this thesis, I stayed in several places. First, I thank Daniel Sempere-Torres who kindly let me stay in his lab in Barcelona and his students who welcomed me, and Dominique Robert and Isztar Zawadzki at their inspirational house in Montreal. Also, I am very grateful to Dominik Jacques for his kind help to submit the thesis on my behalf and to translate the abstract into French.

Finally, I thank my mother, Jungsuk Choi, who has listened once every week about my life's highs and lows and my father, Myungho Park, who inspired me to live my way. And, this thesis work would not have been possible without the fun, critics and love from my friend, colleague, and husband, Marc Berenguer.

TABLE OF CONTENTS

LIST OF FIGURES

CHAPTER 1

Introduction

Atmospheric refraction is often described as the phenomenon that deviates electromagnetic waves from straight lines in the air. This is a consequence of changes in propagation speed due to the non-uniform distribution of atmospheric gases and hydrometeors. Strictly speaking, refraction also includes the attenuation of the amplitude of the wave. For radar waves propagating in the troposphere, where most of weather occurs and affects human life, refraction results in changes in (1) path and traveling time of rays (i.e., the radar phase) between radar and targets, and (2) backscattered power at the receiver (Collier 1996; Briggs 2004; Sizun 2005). Refraction is generally expressed in terms of the complex refractive index $m = n - ik$, where n is defined as the ratio of the speed of microwave in vacuum to that in air (Battan 1973). The imaginary part $-ik$ is associated with the absorption of the material in the air and is an important factor for studying clouds and precipitation (Battan 1973; Sauvageot 1992). This dissertation mostly focuses on the study of n at microwave frequencies, which will hereafter be referred to as the *refractive index*, and its variation in the lower troposphere.

1.1 Atmospheric refraction of microwaves

The refractive index n is very close to 1 and thus is commonly replaced by refractivity $N = (n - 1)\, 10^6$; e.g., for a standard atmosphere, N~300 instead of n=1.0003 (Doviak and Zrnić 1993). Despite the small departures of n from unity, its variation significantly affects radio propagation and radar observations. According to Bean and Dutton (1968), refractivity N in the troposphere and at microwave frequencies can be well approximated as a function of pressure (*P:* hPa), temperature (*T*: K) and water vapor pressure (*e*: hPa);

$$N = 77.6\frac{P}{T} + 373000\frac{e}{T^2}. \tag{1.1}$$

Hence, *N* can be estimated from available atmospheric measurements obtained with surface weather stations, towers, or radiosonde soundings. For example, Fig. 1-1 shows the near surface profile of *N* computed from a radiosonde sounding of *P*, *T*, and *e* (panels a-c) launched in the morning.

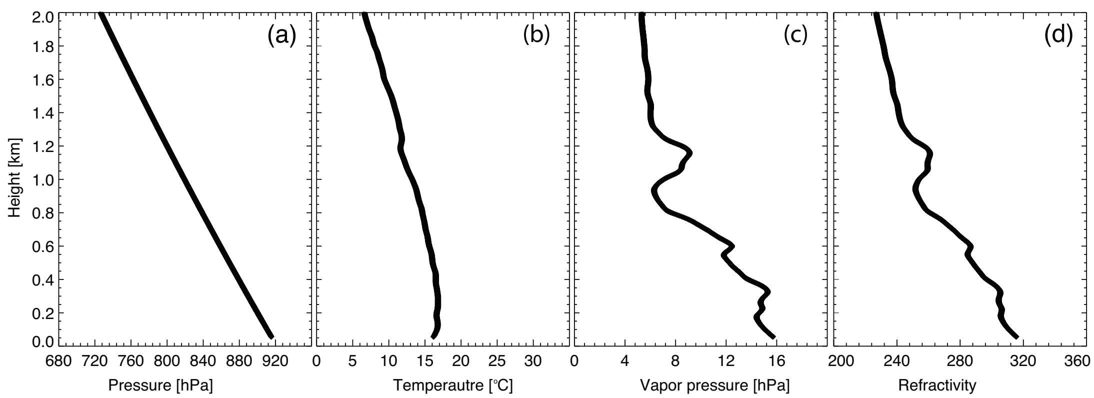

Fig. 1-1: An example of atmospheric soundings at 11:33 UTC (7:33 local standard time) on 14 June 2002 in the Southern Great Plains, Oklahoma. (see Figs. 1-4 and 1-5 for the exact location where this sounding was launched and Fig. 2-2 for orography around): (a) pressure in hPa, (b) temperature in Celsius, and (c) water vapor pressure in hPa, and (d) refractivity up to 2 km above the ground.

We can first see in Fig. 1-1 that these variables generally decrease with height, though some fluctuations in *N* evidently appear due to the variations in water vapor and temperature. These *N* fluctuations have an impact on the path of the radar beam according to Snell's law. In particular, the vertical variation of *N* determines the beam bending toward or away from the ground (Doviak and Zrnić 1993). However, because detailed information about the refractivity field is rarely available in real-time, refractivity is usually assumed to decrease linearly with height. Then, Fig. 1-2 illustrates the example of the beam bending that can determine the radar horizon and, thus, the visibility of targets.

a) $N_1 > N_2$: normal conditions b) $N_1 >> N_2$: anomalous conditions

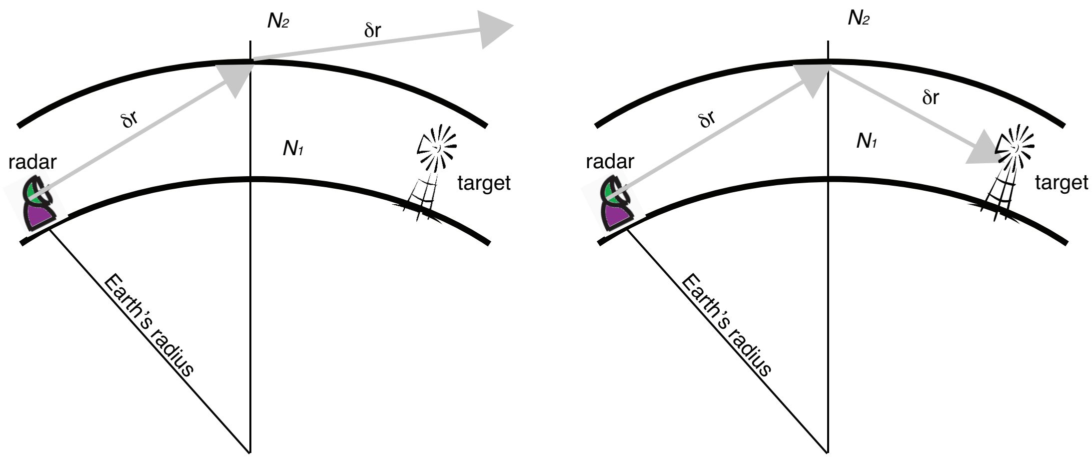

Fig. 1-2: Illustration of a radar ray (grey arrow) trajectory along range increment (δr) under the assumption that the spherical atmosphere is stratified in height with different N_1 and N_2. (a) We refer the normal conditions as N_1 (near surface) is larger than N_2 considering the decrease of N in the vertical. According to Snell's law, i.e., $(10^{-6}N_1+1)\ \sin\theta_1=(10^{-6}N_2+1)\ \sin\theta_2$ where θ is the incident angle of the ray, the ray bends downward but still away from the ground target. (b) If N_1 becomes much larger than N_2 (e.g., nocturnal cooling near surface), the negative vertical gradient of N becomes much larger. Such anomalous conditions allow the ray to bend toward the ground and to detect the ground target invisible in the normal conditions.

Such characteristics of the beam propagation are well known to affect the quality of scanning radar data. Namely, the more the beam bends, the more ground echoes appear especially at low elevation angles, contaminating radar Quantitative Precipitation Estimates (QPE), velocity measurements, and so on (e.g., Steiner and Smith 2002; Berenguer et al. 2006; Cho et al. 2006; Vasiloff et al. 2007 and references therein). Also, due to the lack of near-ground *dN/dh* estimates based on conventional sounding observations, the value of *dN/dh* is often approximated to -40 km^{-1} obtained under standard atmosphere (Doviak and Zrnić 1993) and used in numerous operational volumetric scanning radar analyses (e.g., Germann et al. 2006; Bellon et al. 2007; Tabary 2007; Berenguer and Zawadzki 2008). However, this simple approximation, referred often as the normal propagation condition, can introduce some errors in the precise positioning of detected targets (e.g., Bech et al. 1993; Skolnik 2001; Ge et al. 2010). For example, Fig. 1-3 illustrates the dependence of radar ray height along range on different propagation conditions. If the targets are detected under superrefractive conditions, but the analysis assumes still the normal condition, it is possible to cause ray height errors of 1~2 km at 100~ 200 km in range.

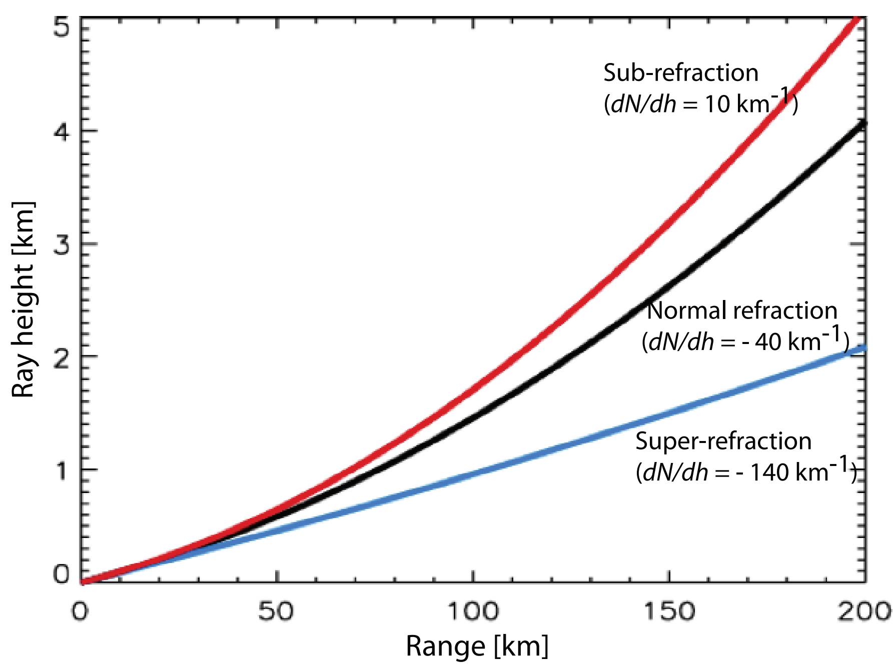

Fig. 1-3: Ray height as a function of range under different propagation conditions: the larger $-dN/dh$ becomes, the more the ray is bent toward the ground, and thus the smaller the ray height for a given range.

Secondly, Fig. 1-1 shows also that the variation of N with height resembles more the vertical profile of water vapor than those of temperature and pressure. In Fig. 1-4, we can see that the dependence of N on humidity is larger at warm temperatures, where more water vapor is required to saturate the air (Rogers and Yau 1989; Ahrens 2000). Such sensitivity of N has been already addressed in Fabry et al. (1997) and further observed with surface station measurements in the Montreal region during summer 1998 (Fabry and Creese 1999). Their results showed that the variations of water vapor contributed about 70% to the estimated refractivity changes.

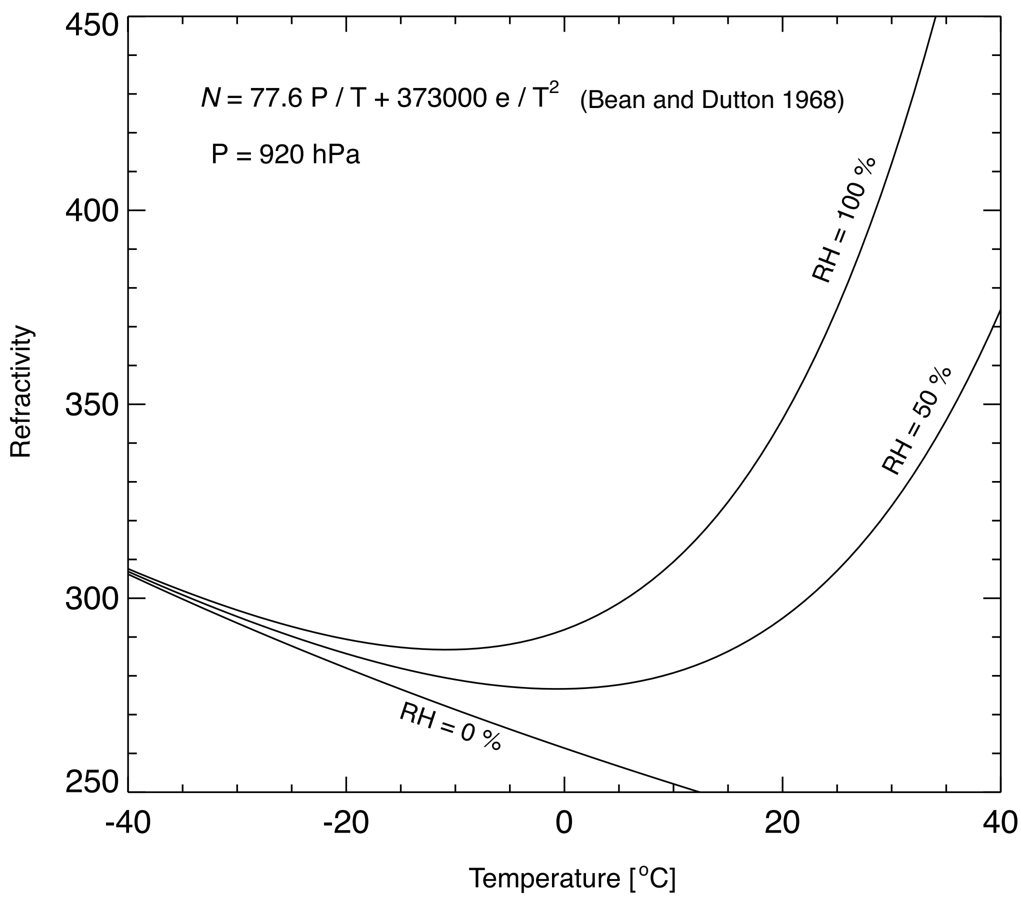

Fig. 1-4: Refractivity N as a function of temperature, relative humidity for a given pressure. The refractivity varies with temperature in the cold air. On the other hand, in warm air, the effect of humidity (in terms of relative humidity RH) on the variation on N is quite large; the more humidity (warm), the larger the N.

In addition, the algorithm developed by Fabry et al. (1997; a brief description is provided in Chapter 2) uses McGill S-band (10-cm wavelength) radar phase measurements from fixed ground targets to retrieve *N*. Hence, these *N* retrievals can be linked to the variations of moisture. Unlike the in-situ point instruments, scanning radars can provide the horizontal field of *N* every 5 to 10 minute in the bottom 250 m of the atmosphere (Weckwerth et al. 2005). Fig. 1-5 presents an example of the retrieved refractivity field around the measurement time of the sounding used in Fig. 1-1. We can see that *N* variations are monitored within a range up to 40 km around the radar and that the analysis domain slightly dried out between 10:30 UTC and 12:30 UTC.

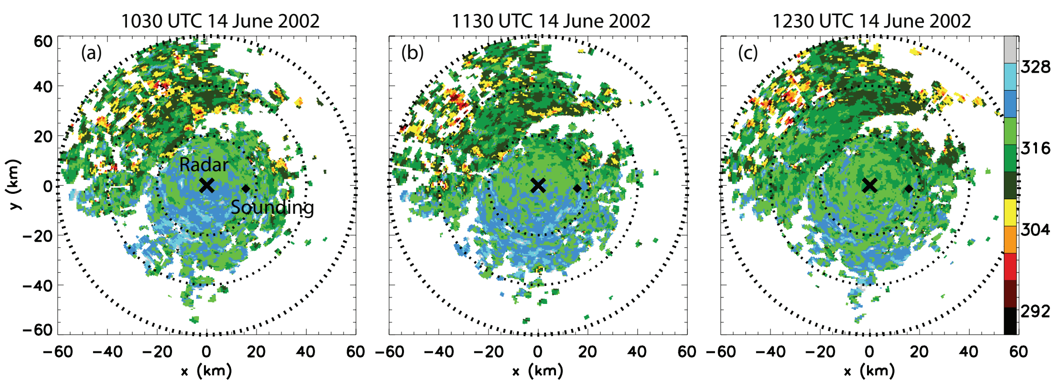

Fig. 1-5: An example of time evolution of radar retrieved refractivity fields selected on 14 June 2002 in the Southern Great Plains, Oklahoma. Higher values represent more moist area. The sounding used in Fig. 1-1 was launched at the location of a diamond symbol and near the time of (b). (a) and (c) show the refractivity field 1 hr before and after (b).

Moreover, such monitoring of refractivity fields can be useful for studying convection initiation that is sometimes associated with discontinuity of moisture (e.g., fronts, dry-lines, etc.). Figure 1.6 shows the examples of the real-time display of refractivity (lower middle) and its 5 min changes (upper middle) fields accompanying with the field of reflectivity (upper right) as well as radial velocity (lower right) observed during IHOP_2002. We can see the 30 min change in the boundaries in the refractivity fields indicated as the “Dry line” that is well collocated with some new cells developed in the reflectivity field.

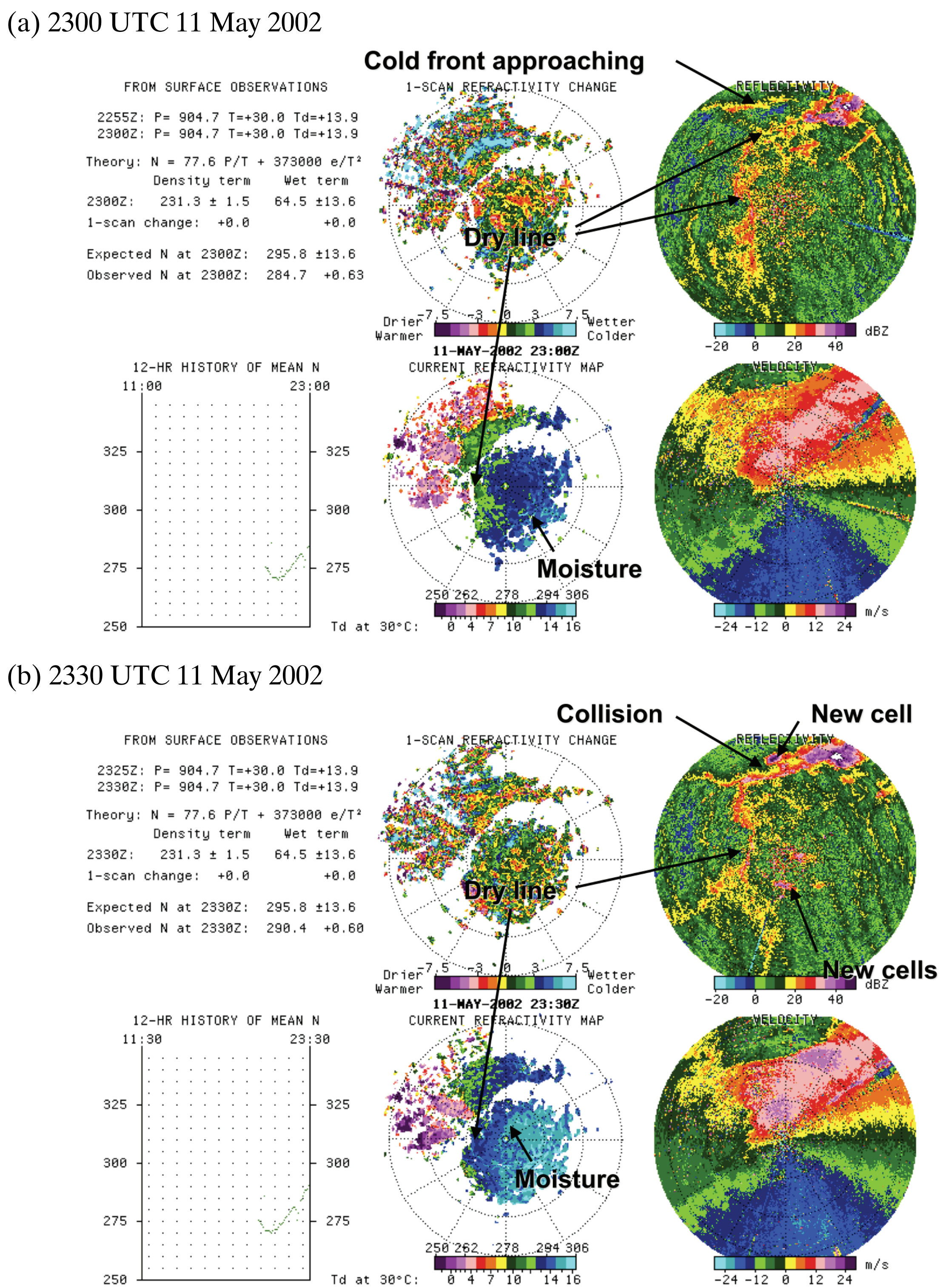

Fig. 1-6: Examples of real time display of refractivity during IHOP_2002 at (a) 2300 UTC 11 May 2002, and (b) 2330 UTC 11 May 2002: 1-scan refractivity change (upper middle), reflectivity (upper right), 12 hour mean N history (lower left), refractivity map (lower middle), and Doppler velocity (lower right). From Fabry 2010 (personal communication).

Finally, it is also worth mentioning that some long-wavelength radars (most notably, Very High Frequency -VHF-, Ultra High Frequency -UHF- and, sometimes, S-band radars) can observe scattering due to strong gradients of refractivity. These observations, typically obtained at vertical incidence, have been used in turbulence studies near the top of the boundary layer (Konrad and Robinson 1972; Gossard et al. 1998). Unfortunately, near-ground measurements of such radars cannot be used due to contamination by ground clutter.

1.2 Motivation and objectives

Doppler scanning radar observations have been widely used for understanding and forecasting summer convective storms that often cause severe weather such as flash floods, hail, or tornadoes (Burgess and Lemon 1990; Doviak and Zrnić 1993). Such surveillance radars have mainly provided reflectivity and Doppler velocity data, which allowed us to monitor the field of precipitation and the radial component of the winds at a range resolution of a few hundred meters and temporal resolution of 5 to 10 minutes. These resolutions can beneficially capture the features of summer convection (typically few kilometers in space and few hours in time; Jorgensen and Weckwerth 2003). Furthermore, these observations have been usefully assimilated into numerical prediction model for forecasting convective storms (e.g., Laroche and Zawadzki 1994; Sun and Crooke 1997; Caya et al. 2002; Chung et al. 2009).

For better understanding convective storm initiation and evolution, a number of observational and modeling studies have addressed the need for accurate measurements of boundary layer moisture (Crook 1996; Weckwerth et al. 1999) related to the parameterization of convection (e.g., Guo et al. 2000). For example, Weckwerth (2000) showed that the low resolution of stability parameters (e.g. moisture, temperature, and wind shear) measured with radiosonde soundings makes them not sufficient to examine convective initiation, so that more accurate measurements, especially of moisture and its variation in the convective boundary layer, are needed at least with a horizontal resolution of 500 meters.

Moisture is commonly measured in-situ using radiosondes (as in Fig. 1-1), but such measurements hardly allow us to resolve moisture estimates at the scale of convection due to their low resolution (e.g., one or two soundings are typically available a day and separated by a few hundred kilometers). During the last two decades, numerous studies have explored the way to estimate moisture using different remote sensors; for example, direct measurement of integrated precipitable water from ground based Global Position Systems receivers (Businger et al. 1996) or the profile of humidity from space based GPS receivers using radio occultation (Kuo et al. 2004), and refractivity profile from wind profiler together with GPS and Radio Acoustic Sounding Systems (Gossard et al. 1999) or radiometers (Bianco et al. 2005). However, all these instruments hardly provide any low-level information.

As an alternative, the radar refractivity retrieval (Fabry et al. 1997) has been recognized for its positive performance of providing moisture field information near ground during several international experiments. For example, the International H_2O project field experiment (IHOP_2002), held in the Southern Great Plains in the USA, showed that the refractivity retrievals based on single radar agreed with those from various instruments (Weckwerth et al. 2005). This result encouraged the use of radar N field in studying the initiation of convection (Fabry 2006; Weckwerth and Parsons 2006). Also, several studies have been conducted to characterize convergence zones where convection initiation often occurs by analyzing the relationship between the sharp horizontal gradients of refractivity, the so called "dry lines" and the thin reflectivity lines related with cold fronts or storm outflows (Wilson and Roberts 2006; Wakimoto and

Murphey 2009). Similar experiments have been conducted in the framework of radar networks (e.g., Roberts et al. 2008). This interest in refractivity data is also driving in parallel technical progress to measure this refractivity field with more radars using magnetron transmitter at different wavelengths (C- and X-bands; Cheong et al. 2008; Parent-du-Chatelet and Boudjabi 2008; Nicol et al. 2009).

Despite the aforementioned growing interest on the utilization of the technique, little research has been done on the assessment of the uncertainties that affect the retrievals. For example, the retrieved refractivity fields of Fig. 1-5 look unrealistically noisy, and the coverage of the retrievals changes with time. *Can we determine the origin of, characterize, and quantify the errors affecting the refractivity retrievals?*

Fabry (2004) quantified the magnitude of the expected errors in refractivity retrievals due to the different factors affecting the algorithm: the largest errors (of the order of Δn=10 ppm) are due to vegetation sway by the wind, while other factors such as the delay caused by severe rain, the drift of transmitted frequency, path changes due to anomalous propagation or differences in target height would result in errors of less than 2 ppm. These error bars were computed for a target located at 25 km from the radar under some of the hypotheses of the algorithm (more details are provided in chapter 2).

However, the results mentioned above are obtained based on a number of speculations and simplifications, and not contrasted against observations. Hence, the first objective of this dissertation is to investigate the nature of the error sources in the retrieved refractivity fields based on a discussion of the algorithm's hypotheses and the analysis of radar phase observations.

Although the retrieval algorithm mentioned above is good at monitoring the horizontal variation of the refractivity field, it does not provide any information about the vertical changes. So far, the usual way to measure them is using sounding measurements, which are often inaccurate near surface and available at a limited number of locations and times. On the other hand, as mentioned earlier, the coverage of echoes from ground targets depends on propagation conditions (i.e., on the vertical variation of N at low level). Hence, the second challenge we have faced in this dissertation is the use of ground echo coverage to characterize the vertical gradient of N; i.e., *can we estimate near-surface dN/dh from radar observations?*

More knowledge about vertical structure of N near the surface could be used in a number of applications such as (i) overcoming some of the limitations of the refractivity retrieval algorithm (see Chapter 2), (ii) providing information about beam bending to techniques for ground clutter identification (or more generally echo classification) in radar Quality Control schemes, and iii) better positioning of radar echoes instead of using the normal $dN/dh = -40$ km^{-1} (Doviak and Zrnic 1993).

1.3 Approach

The conventional use of scanning radar observations at low-elevation angles (0.0°~0.5°) has been limited for most meteorological applications due to contamination by clutter returned from ground targets such as power poles, railways, and terrain. However, the radar intensity and phase measurements returned from ground targets have shown their extended usage for revealing refractivity information under the assumption of flat terrain (e.g., Fabry and Keeler 2003; Fabry 2004).

To achieve both the gauge of errors in horizontal N field over complex terrain and the estimation of vertical gradient of N, this thesis underlines the characterization of ground targets detected by scanning radar in the context of

(i) the assessment of the error factors in the refractivity retrieval algorithm: the traveling path of the radar beam to the targets under complex terrain will be different from that under flat terrain, which can affect the phase measurements. And, the traveling path will be determined by both propagation conditions and the target heights. Hence, this study mainly simulates phase measurements with these factors by characterizing the ground targets seen by the radar based on the available measurements such as sounding measurements and digital terrain maps.

(ii) the estimation of vertical gradient of *N*: we have seen that the observation of ground echo coverage shows some clue of near-ground propagation conditions (*dN/dh*). If the ground targets are known, the coverage of ground echo returned from them can be simulated as a function of *dN/dh* and be compared with the observed one to determine the best estimate of *dN/dh.* To do this, the work in the thesis characterizes statistically the ground targets detected by the radar.

All data used in the thesis are collected from the field experiment called the International H_2O Project (IHOP_2002) that was conducted from 13 May to 25 June 2002 in the Southern Great Plains of the United States. The domain is shown in Fig. 1-6 and exhibits frequent occurrence of summer convection exposed by low-level moisture from the Gulf of Mexico transported by southerly low-level jets. A variety of instruments was deployed to understand the distribution of low-level atmospheric moisture and how it can be related to the atmospheric boundary layer processes of convection and thus to improve warm-season quantitative precipitation forecasting (Weckwerth and Parsons 2006). Among them, the NCAR's S-Pol radar made the target phase measurements used in the refractivity retrieval algorithm (Keeler et al. 2000; Fabry and Pettet 2002).

Besides, during that experiment, several instruments were deployed nearby the S-Pol radar such as the Integrated Sounding System (e.g., Parsons et al. 1994) located at Homestead site in Fig. 1-6, the tethered sonde soundings (Weckwerth et al. 2004) near Homestead site, radiosonde soundings (ARM Cental Facility), and retrieved soundings from Atmospheric Emitted Radiance Interferometer

(AERI; Feltz et al. 2003) at Homestead site. These various soundings will be useful to provide propagation conditions for the phase simulations as well as for verifying the radar estimated one based on echo coverage.

The detailed methods and results of this thesis are presented in the following chapters that have been submitted for publication:

- Park, S. and F. Fabry, 2010: Simulation and interpretation of the phase data used by radar refractivity retrieval algorithm. Published to the *Journal of Atmospheric and Oceanic Technology*, **27**, 1286- 1301. (Chapter 2).
- Park, S. and F. Fabry, 2010: Estimation of near-ground propagation conditions using radar ground echo coverage. Submitted to the *Journal of Atmospheric and Oceanic Technology*, May 2010 (Chapter 3).

Finally, the conclusions and future work are discussed in Chapter 4. The text of these manuscripts is meant to be self-contained, so some overlap between the chapters is unavoidable.

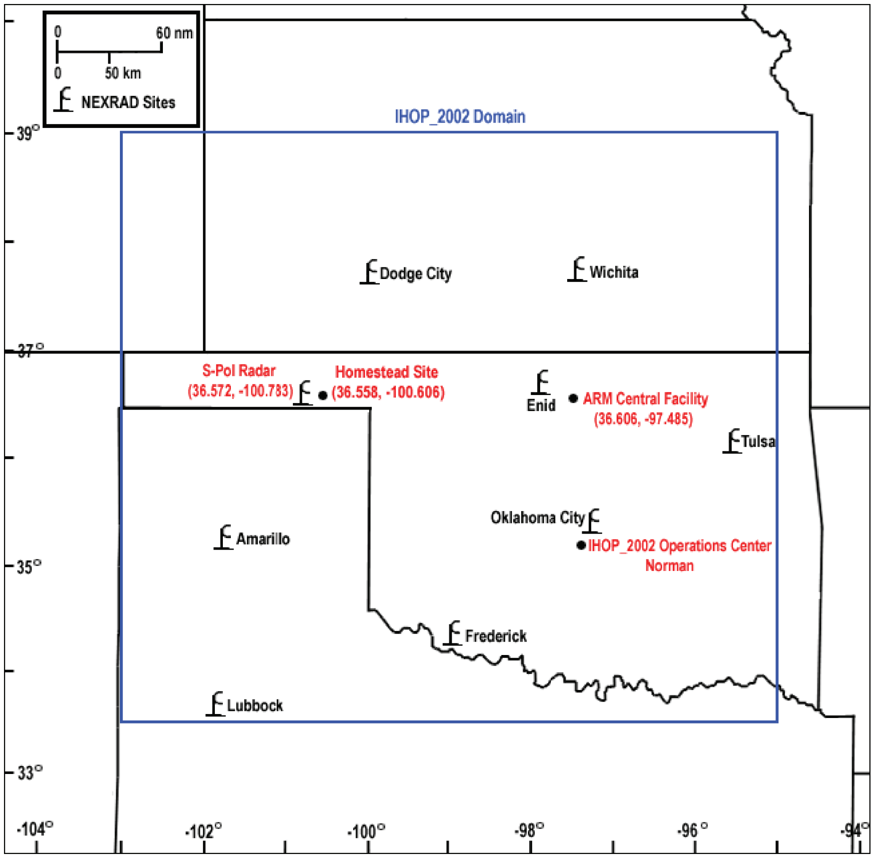

Fig. 1-7: The domain of IHOP_2002. [Available at the following website: http://www.eol.ucar.edu/dir_off/projects/2002/IHOP.html]

CHAPTER 2

Simulation and interpretation of the phase data used by radar refractivity retrieval algorithm

The phase measurements returned from ground targets are the basis of the refractivity retrieval algorithm (Fabry et al. 1997) that can provide the horizontal field of near-ground moisture. Despite its usage expected for understanding summer convections, no study has yet assessed the errors of the refractivity retrieval.

Phase data are often noisy due to the properties of the ground targets (e.g., swaying vegetation, varying terrain), propagation conditions, etc. (Fabry 2004). Although these factors should be considered for the study of refractivity retrieval errors, their practical characterization is quite challenging. Therefore, the following study focuses on the factors that can be described from available observations; that is, different target heights over complex terrain illuminated by radar beam trajectory due to different propagation conditions. If these factors are critical enough to affect the phase measurements, the simulated phase noisiness should be similar to the observed one, which led us to propose a phase simulator. Two selected cases are simulated and validated with true observations. The performance and limitation of the phase simulator is discussed.

This chapter consists of a paper published in the Journal of Atmospheric and Oceanic Technology, and the original version is available at

www.journals.ametsoc.org/pdf/10.1175/2010JTECHA1393.1

Simulation and interpretation of the phase data used by radar refractivity retrieval algorithm

Shinju Park and Frédéric Fabry

Department of Atmospheric and Oceanic Sciences, McGill University, Montreal, Quebec, Canada

Abstract

The radar refractivity retrieval algorithm applied to radar phase measurements from ground targets can provide high-resolution, near-surface moisture estimates in time and space. The reliability of the retrieval depends on the quality of returned phase measurements that is affected by factors such as i) the vertical variation of the refractive index along the ray path, and ii) the properties of illuminated ground targets (e.g., height and shape of the targets intercepted by radar rays over complex terrain). These factors introduce ambiguities in the phase measurement that have not yet been considered in the refractivity algorithm and that hamper its performance.

A phase measurement simulator was designed in order to better understand the effect of these factors. The results from the simulation were compared with observed phase measurements for selected atmospheric propagation conditions estimated from low-level radio sounding profiles. Changes in the vertical gradient of refractivity coupled with the varying heights of targets are shown to have some influence on the variability of phase fields. However, they do not fully explain the noisiness of the real phase observations because other factors that are not included in the simulation, such as moving ground targets, affect the noisiness of phase measurements.

2.1. Introduction

The radar refractivity retrieval developed by Fabry et al. (1997) is one way of estimating near surface moisture using the phase measurement of the radar signal returned from ground targets such as power lines, buildings, or mountains. Since it can provide maps of near surface moisture with high resolution in time (5 min) and space (4 km), this technique triggered high expectations in the field of quantitative forecasting of severe convective storm initiation and development (e.g., Weckwerth and Parsons 2006; Wilson and Roberts 2006).

During the last decade, the refractivity retrieval technique has been implemented on both research and operational radars and evaluated in several field experiments (Roberts et al. 2008; Cheong et al. 2008; Fritz and Chandrasekar 2009; Heinselman et al. 2009). For example, the International H_2O Project (IHOP_2002) had an S-band research radar (S-Pol) deployed in the Southern Great Plains of United States. One significant achievement of this experiment was the validation of the moisture radar retrievals compared with measurements from numerous conventional instruments [surface stations, aircraft, soundings, AERI (Atmospheric Emitted Radiance Interferometer)]. Weckwerth et al. (2005) showed that the radar moisture retrievals during IHOP_2002 were highly correlated with other moisture estimates up to 250 m above the ground. Their results suggested that radar refractivity may provide lower boundary layer moisture information for data assimilation; in this direction, Montmerle et al. (2002) assimilated moisture near the ground into the McGill short-term forecasting system. Also Wilson and Roberts (2006) suggested that moisture retrievals can possibly be useful as a precursor of convection associated with dry/convergence lines.

Despite growing interest in the use of radar refractivity, not much emphasis has been placed on the quality control of the refractivity retrieval measurements.

Fabry (2005) identified the following factors as possible sources of uncertainty of the retrieval: 1) the extreme noisiness of the measured phase field, and 2) simple assumptions used in the retrieval algorithm (section 2-2). Understanding and quantifying the noise introduced by the different sources of uncertainty affecting the refractivity retrieval will enable to develop an improved algorithm. By means of a phase simulator, we intend to assess in this study: 1) Which types of phase errors have a statistically predictable behavior? 2) How large are those errors? and 3) Do they account for the observed phase variability? To achieve these goals, we first review the current algorithm and speculate about its noise sources (section 2.2). In Section 2.3, we described how these noise sources are incorporated into the phase simulator. For selected cases, the simulated phase differences are validated with the observations in section 2.4. The conclusions are followed in section 2.5.

2.2. Phase, phase noise, and refractivity retrieval

a. Refractivity retrieval algorithm

The current radar refractivity retrieval starts with the radar phase measurement ϕ at time t, and range r. Here, transmit pulses are assumed to be preferably generated with a Klystron transmitter with a sufficiently stable frequency f, yielding

$$\phi(r,t) = 2\pi f t_{\text{travel}} = \frac{4\pi f}{c}\int_0^r n(r',t)dr' \quad (2.1)$$

The traveling time, t_{travel}, in (2.1) is the time required for a radar ray to travel twice the pathlength (or range r) to the target at the speed of propagating microwaves through the atmosphere. Here, the air reduces the speed of microwaves below the speed of light in vacuum, c. The ratio between the speed of light in vacuum and the speed in the atmosphere is referred to as the refractive index of air (n) and is integrated along the ray path in (2.1).

The refractive index of air near the surface is approximately 1.0003 for a standard atmosphere (Doviak and Zrnic 1993). In reality, it varies along the ray path. It is often expressed in terms of refractivity [$N = (n\text{-}1)\times 10^6$] According to Bean and Dutton (1968), the refractivity in the lower troposphere can be empirically approximated with atmospheric pressure (P; hPa), temperature (T; K), and water vapor pressure (e; hPa) within an accuracy of 0.1 at microwave radar frequencies as:

$$N = 77.6\frac{P}{T} + 373000\frac{e}{T^2}. \tag{2.2}$$

Additionally, in warm weather conditions, spatial and temporal changes in refractivity are known to be mostly caused by changes of near-surface moisture (Fabry and Creese 1999). Therefore, the radar-measured phase can be used to first retrieve refractivity from (2.1) and, second, the water vapor information using (2.2), if the following assumptions are satisfied (Fabry et al. 1997; Fabry 2004):

(i) Targets are rigorously stationary. Only fixed ground targets can be used in the retrieval algorithm, whereas moving targets (such as precipitation) must be avoided. This is needed in order to associate changes in traveling time (or phase) with changes in refractivity in the horizontal (what we want to retrieve). However, in reality, the phase returned from ground targets varies at different time scales (from a second to years) due to various phenomena such as vegetation sway and growth, propagation delay, turbulence, natural disasters, or land use changes. The current retrieval algorithm mitigates some of these factors by calibrating measured phase relative to a certain reference phase $\phi_{t_{ref}}(r)$ as:

$$\Delta\phi = \phi(r,t) - \phi_{t_{ref}}(r) = \frac{4\pi f}{c} r\left[\overline{n(r,t)} - \overline{n(r)}_{t_{ref}}\right], \tag{2.3}$$

where the overbar indicates path-averaged values, and the subscript t_{ref} indicates values obtained at a reference time.

(ii) The reference for the calibration is assumed to be taken when the refractivity field is as uniform as possible. This condition is best satisfied during or immediately after stratiform rain in windy and cool conditions. Alternatively, an approximation of the standard deviation of refractivity estimates from surface weather stations can also help us to select the reference time if the number of weather stations is sufficiently dense over the radar domain. For a known $n(r)_{t_{ref}}$ and the phase field at the selected reference time, the refractivity at the time of interest [$n(r,t)$] is obtained by computing the derivative of measured $\Delta\phi$ with respect to range:

$$n(r,t) = \frac{c}{4\pi f}\frac{d\Delta\phi}{dr} + n(r)_{t_{ref}} . \tag{2.4}$$

Fabry (2004) used smoothing to guarantee the robustness of the retrieved refractivity field.

(iii) *Phase data can be aliased.* When processing (2.4) from (2.3), we must be aware that small differences of refractivity fields can result in large and ambiguous differences in phase observations. Moreover, when phase exceeds $\pm 180^\circ$, it is still observed but it is wrapped within the range $\pm 180^\circ$ (phase aliasing), which may result in some uncertainty. To minimize these errors, the algorithm smoothes $\Delta\phi$ over small regions and over short paths [i.e., using (2.4) twice for neighboring targets]. A key hypothesis for this to work is that all targets are on a flat terrain and at the same height as the radar (as described in Fabry 1997, Fabry 2004).

b. Noisiness of the observed phase differences

Based on (2.4), the quality of the retrieved refractivity is determined by the quality of phase observations (affected by instrumental or measurement errors) and by the assumptions of the algorithm itself (listed above). The latter are being investigated in this paper. If these assumptions are totally fulfilled, for the case of a uniform refractivity field, observed phase differences should result in concentric rings that only depend on range, as predicted by (2.3). Figure 2-1a shows an example of the phase differences simulated with (2.3), provided that the uniform N field at the observation time is 13.9 higher than that of the reference. Note that a 1 of N difference, corresponding to the change of 1°C in temperature or 0.2 hPa in vapor pressure, can cause a phase change of 6.7°/km^{-1} for S-Pol (2.8 GHz) according to (2.3). As a result, multiple aliasing appears roughly every 4 km in range.

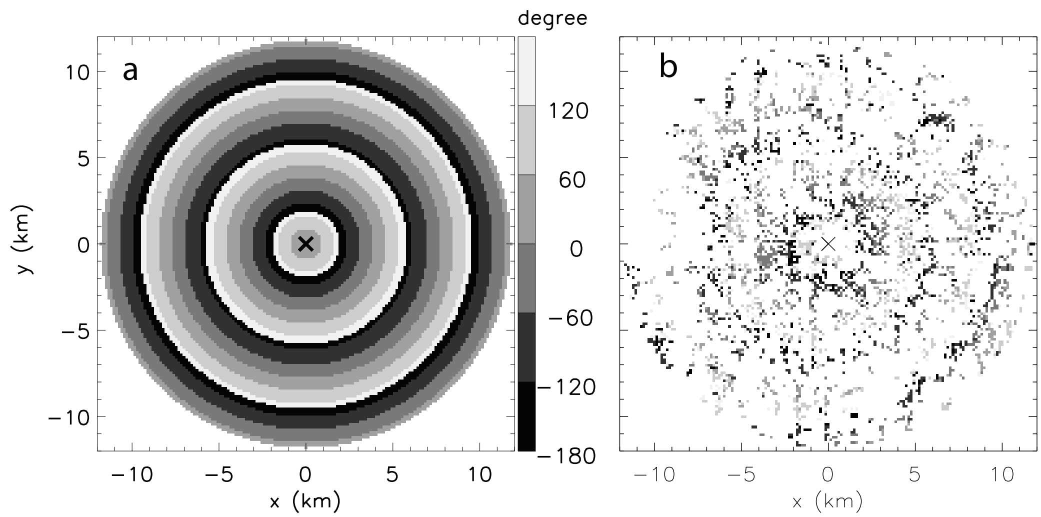

Fig. 2-1: a) Simulated phase difference field assuming that the uniform refractivity field of a current scan is 13.9 higher than that of the reference scans. b) An observed phase difference between current (2332 UTC 15 May 2002) and a reference (2027 UTC 14 May 2002) scan during IHOP_2002 in Oklahoma. The S-Pol radar is located in the middle of this plot. The spottiness in coverage is due to the limited number of fixed ground targets that can be used for refractivity measurements. To avoid some noise that may occur due to local variations within few minutes, the observed phases are averaged over four consecutive scans.

Such uniform simulated fields are not frequently observed in reality. Figure 2-1b shows a field of $\Delta\phi$ measurements at the 0° elevation angle obtained during IHOP_2002 (Weckwerth et al. 2004). Spatially averaged N differences of about

13.9 were observed between the reference and the observation times (i.e., 277.3 at the observation time and 263.4 at the reference time within the first 10 km in range). Concentric circles in the observation become less obvious with increasing range, indeed indicating the presence of horizontal refractivity gradients in this region. Moreover, the observed field is overall significantly noisier than the one simulated. This suggests that propagation delays are not only due to the horizontal variability of N (what we want to retrieve for moisture extraction) but also to other factors that are not taken into account by, in the current algorithm, namely,

(i) ground targets may not be fully stationary,

(ii) the reference N field may not be horizontally uniform at small scales, and

(iii) the heights of targets may not be at the same height of the radar due to their different heights or to complex terrain.

However, identifying and quantifying the contribution of these factors to the noisiness in phase differences is not simple. For example, 1) the information of real target properties (movement, shape, etc.) and location can hardly be resolved within a radar pixel (150 m by 1°, for instance), and 2) the small-scale variability of N at the reference time cannot be obtained unless more station measurements are available over the domain. The first two factors [(i) and (ii)] are, thus, not included in the simulation. Instead, we focused on the third factor (iii) inspired by Fabry (2004). As shown in Fig. 2-2, he observed that phase differences were sensitive to different target heights and the temporal change of propagation conditions. Hence, we have explored further how the lack of alignment between the radar and ground targets would affect the ray paths and result in phase noisiness contributing errors in N retrieval.

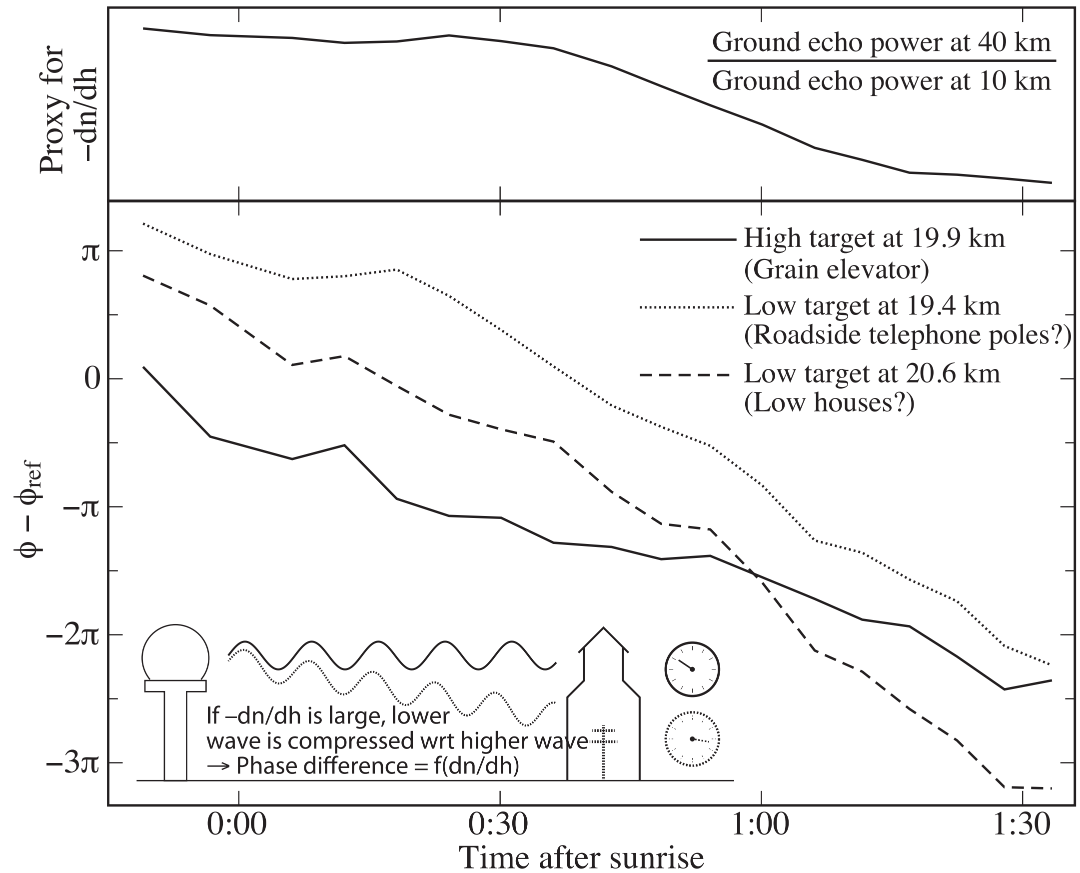

Fig. 2-2: Time evolution of the phase of three neighboring targets along the same azimuth during the disappearance of trapping conditions immediately after sunrise. The phases of the two low level targets (dotted and dashed lines) parallel each other because similar changes in path-integrated *n* occur in the two low-level paths between the radar and these targets. In between these low-level targets is a higher target whose phase (solid line) does not vary as much because the change in path-integrated *n* along the higher-level path is smaller. This occurs as a result of an adjustment in d*n*/d*h* as we move from trapping conditions (illustrated in the inset above by the stronger reflections of faraway targets) to normal propagation conditions. During trapping conditions, the higher target only 20 km away was about 180° out of phase compared to what it would have been under normal propagation conditions. This phenomenon introduces noise in the $\phi - \phi_{ref}$ field, complicating the retrieval of *n* between targets of different heights, and forms the basis for (14). From Fabry (2004).

It is well known that refractivity generally decreases with height. The gradient of the refractive index in the vertical (*dn/dh*; approximately spherically-stratified in the lower atmosphere; Doviak and Zrnic, 1993) determines the propagation conditions of microwaves. When the vertical profile of refractivity is constant (*dn/dh* = 0 ppm km^{-1}), the ray will travel in a straight line. Otherwise, the ray will bend upward (downward) for propagation conditions of *dn/dh* greater (or less) than 0 ppm km^{-1} (Bean and Dutton 1968; Sauvageot 1992; Steiner and Smith 2002). Consequently, the amount of bending determines the areas of ground (or targets above the ground) detectable at a certain distance. Similarly, for given propagation conditions, the topography within the radar domain and the distribution and height of targets may also result in areas with more or less ground target measurements. Hence, as shown in Fig. 2-3, to determine the sensitivity of the propagation conditions (*dn/dh*) to the phase return, let us consider a given ground target with a certain height H_{target}. First, we express the location of the ray path as the incremental variables of range r along the Earth's surface d (Fig. 2-3a). The range and the distance of the target from the radar are expressed as the fixed variables of range R and D, respectively. Because we assume that D and H_{target} are known, R can be computed as a function of *dn/dh*:

$$R = \left(\frac{dn}{dh}\right)^{-1} \cos^{-1}\left[1 - \frac{C\left(\frac{dn}{dh}\right)^{2}}{2}\right], \tag{2.5}$$

where $C = \left(E_r + H_{radar}\right)^2 + \left(E_r + H_{target}\right)^2 - 2\left(E_r + H_{radar}\right)\left(E_r + H_{target}\right)\cos\left(\frac{D}{E_r}\right)$ by applying the law of cosines, and E_r is the Earth's radius. If the radius of a ray curvature is the same as E_r (which can be approximated with *dn/dh*=−157 ppm km^{-1}), R is the distance following a line of constant height and is the same as D. For a target at D=30 km, this can be shown in Fig. 2-3b by plotting ΔR with respect to D as a function of *dn/dh*. It is seen that the range is slightly longer i) for larger negative *dn/dh* (yielding more bending), and ii) for higher target height. Although this change in range due to *dn/dh* or target height is relatively small, from mm to cm, it can trigger large changes in phase differences ($\Delta\phi$) between reference and observation times, and it becomes more complex if we consider its aliasing behavior. If $dn/dh = -39$ ppm km^{-1} at the reference time and N=300 for both the reference and observation times, the phase changes due to ΔR can be shown in Fig. 2-3c as a function of dn/dh. No phase difference is observed at $dn/dh = -39$ ppm km^{-1} and the aliasing occurs in superrefraction conditions, that is, for large negative dn/dh. Here, no height dependence on $\Delta\phi$ is shown because the phase changes are plotted relative to the reference propagation conditions at each fixed target height. Hence, the resulting change in pathlength in time under a constant dn/dh conditions should not contribute to the noisiness in the phase but simply to a bias in N. Note that we still consider a constant dn/dh over the radar domain since the spatial variation of dn/dh from available measurements (e.g., soundings) cannot be resolved in the radar pixel resolution.

In fact, to examine the dependence of target heights on $\Delta\phi$ associated with changes of a dn/dh, we should consider the height change of the ray trajectory intercepting a given target. Hence, similarly assuming the trajectory is parabola, we can now compute the height of the ray along range $h(r)$:

$$h(r) = \frac{1 + \left(E_r + H_{radar}\right)\dfrac{dn}{dh}}{2\left(E_r + H_{radar}\right)}\left(r^2 - rR\right) + \left(H_{target} - H_{radar}\right)\frac{r}{R} + H_{radar} \qquad (2.6)$$

This formula is based on Fabry (2004) [eq. (9)] and is practically equivalent to the one in Doviak and Zrnic (1993). It has the advantage of explicitly showing the effect of propagation conditions on the path of a ray intercepting a given target. Let us first compute the ray height with $dn/dh = -39$ ppm km^{-1} for a given target height H_{target} and the terrain (Fig. 2-4a). Typically, ground targets intercept the lower part of the main lobe and, at times, the side lobes (especially at close ranges). Radar rays heading toward the surface are plotted as a gray shaded area in Fig. 2-4a. Note that we consider beam blockage to be caused only by the terrain, and not by any structured target. In other words, we assume that the signal may be reflected by any possible structured target as well as pass around it. More importantly, the height of the lowest nonblocked ray above the terrain at a given range and azimuth can be interpreted as the minimum detectable height (MDH) for ground targets. Therefore, in clear air conditions, strong echoes at a

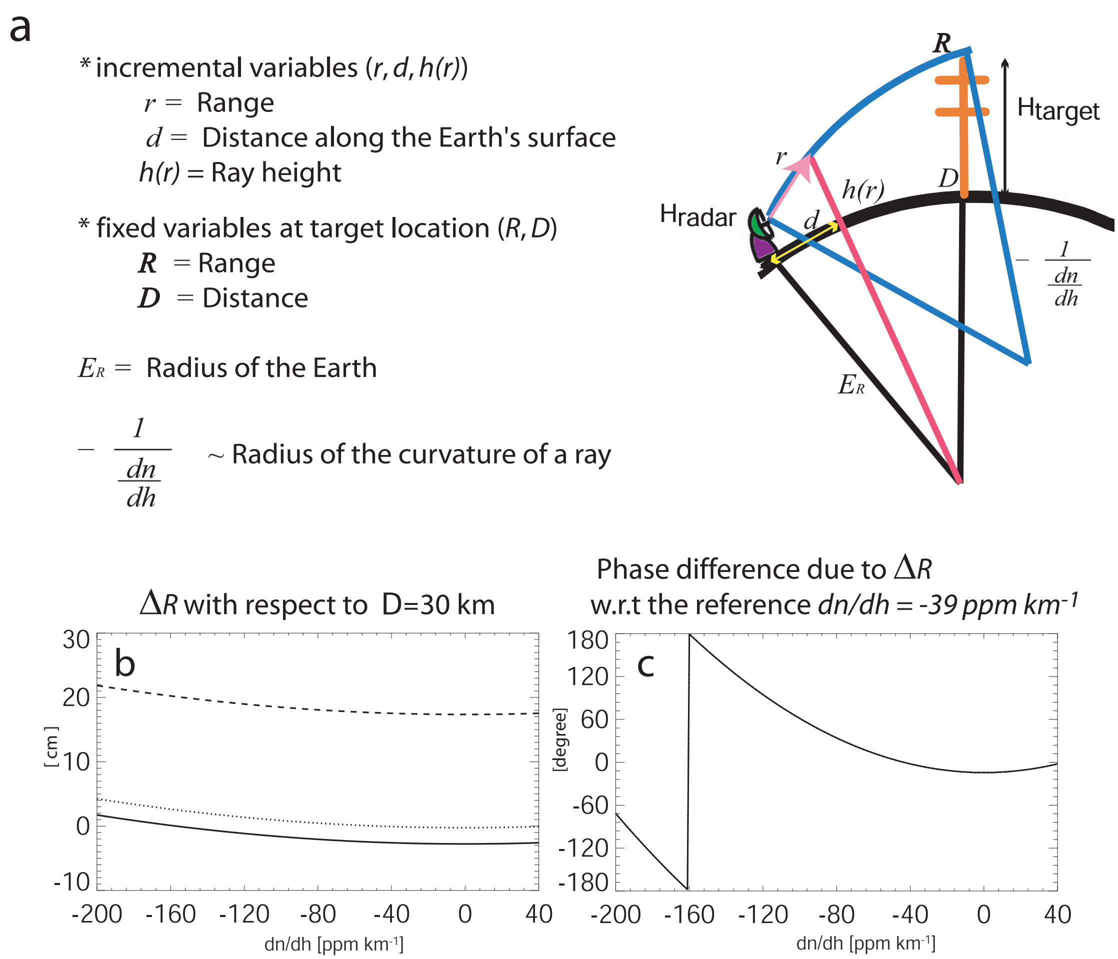

Fig. 2-3: Dependence of the pathlength on target height and propagation conditions. (a) Illustration of the geometry of the problem. (b) Examples of the ΔR variation due to the propagation conditions and target heights relative to the radar height. The solid line indicates that the target height is the same as the radar height. The dotted and dashed lines indicate, respectively, that the heights of the target are at 10 m above and 60 m above the radar. (c) The changes of phase differences with respect to the reference ($dn/dh = -39$ ppm km^{-1}) due to the ray length changes at D=30 km.

given location identify the presence of at least one target higher than the minimum detectable height.

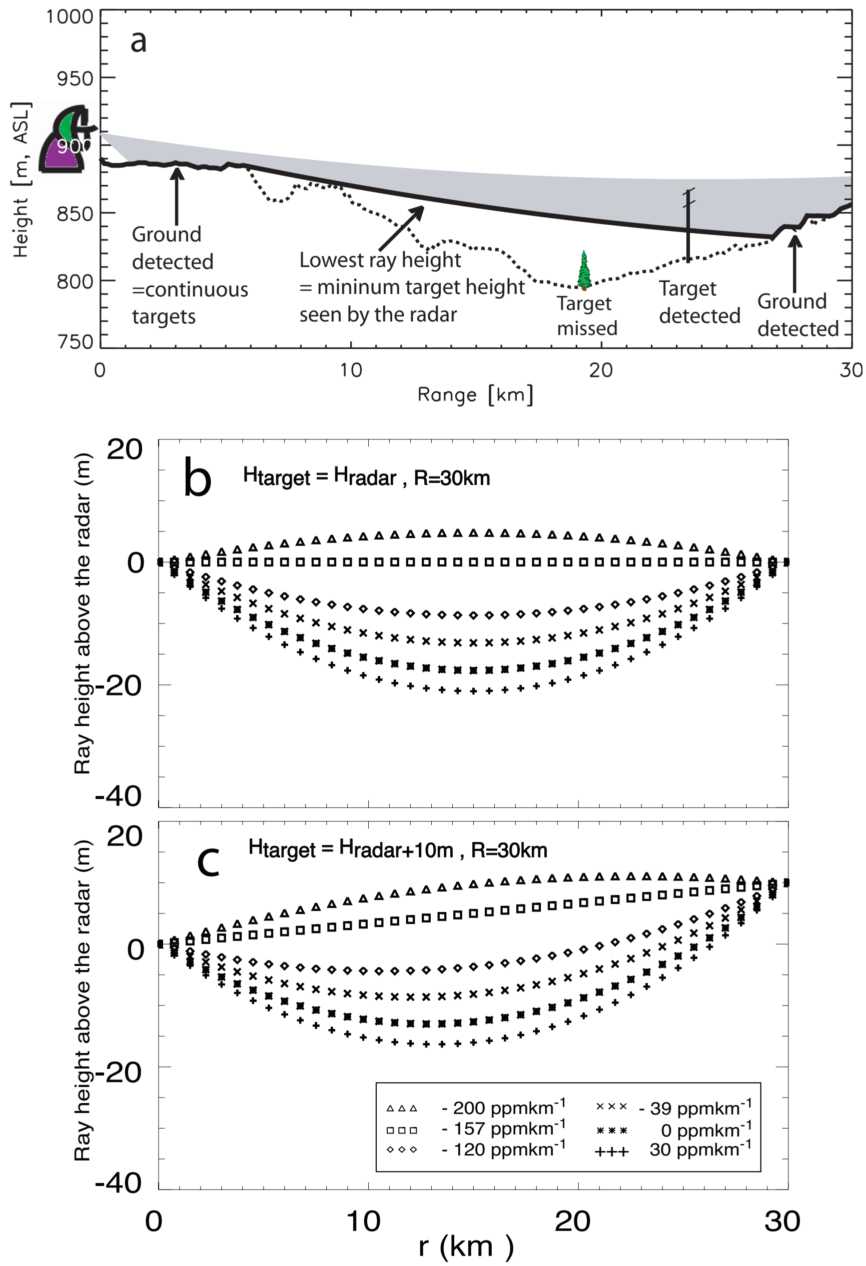

Fig. 2-4: Ray heights affected by propagation conditions. (a) Illustration of ray trajectory. The dotted line indicates terrain height above MSL. The grey shaded area represents the rays going toward the ground as determined by the grazing angle between the radar and ground heights at each range pixel. (b) Ray heights toward a given target as a function of distance along the surface and propagation conditions. Here, the target height is leveled with the radar height. (c) As in (b) but for a target 10 m above the radar.

Now, let us analyze the impact of propagation conditions in (2.6). Fig. 2-4b shows the path of the ray intercepting a target aligned with the radar ($H_{radar}=H_{target}$). For ducting conditions ($dn/dh \leq -157$ ppm km^{-1}), rays follow a convex path to reach the targets. This implies that rays are less blocked by terrain and thus better able to detect the ground at further ranges. On the other hand, in subrefractive conditions ($dn/dh>0$ ppm km^{-1}), rays bend upward (concavely) and are thus likely miss ground targets. Note in Fig. 2-4b that the ray trajectory is as much as 20 m below the radar height for $dn/dh=30$ ppm km^{-1} and would be blocked at near range before reaching the target. Consequently, targets at far range can be detected only in ducting conditions unless the ground target is taller than the minimum detectable ray height. Of course, if we consider target heights being different from the radar height, the interpretation of the phase measurement can be more complicated because the ray may hit or miss the ground targets. To include such complication introduced by changes of propagation conditions as well as target heights on phase, we can rewrite (2.1) for a radar scan observed at time t by substituting $h(r)$ from (2.6):

$$
\begin{aligned}
\phi(R,t) &= \frac{4\pi f}{c}\left[\int_0^R n(r,t)_{H_{radar}}\,dr + \int_0^R \int_{H_{radar}}^{h(r)} \frac{\partial \mathrm{n}(\mathrm{r},\mathrm{t})_{h'}}{\partial h'}dh'dr\right] \\
&= \frac{4\pi f}{c}\left\{\int_0^R n(r,t)_{H_{radar}}\,dr + \frac{dn}{dh}\int_0^R \left[h(r) - H_{radar}\right]dr\right\} \\
&= \frac{4\pi f}{c}\left\{\overline{n(t)}R + \frac{dn}{dh}\left[\frac{\left(H_{target}-H_{radar}\right)R}{2}\right] - \frac{dn}{dh}\left[\frac{1+\left(E_r+H_{radar}\right)\frac{dn}{dh}}{12\left(E_r+H_{radar}\right)}R^3\right]\right\},
\end{aligned}
\tag{2.7}
$$

where $n(r,\ t)_h$ is the refractivity at a given $(r,\ t)$ and height h [if not explicitly mentioned, $n(r,\ t)$ is at the radar height]. Here, the vertical gradient of refractivity dn/dh is assumed to be a constant. As we can see, three terms on the right of (2.7) are affected by dn/dh and the height of the target. We have also substituted R with (2.5) even though it is small. It was added for completeness sake. To quantify their impact on phase differences from (2.3), we compute the propagation error of phase difference measurements ($\sigma_{\Delta\phi}$) according to Bevington (1969):

$$\sigma_{\Delta\phi} = \sigma_{H_{\text{target}}} \left| \frac{d\Delta\phi}{dH_{\text{target}}} \right| = \sigma_{H_{\text{target}}} \left| \frac{d\phi(R,t)}{dH_{\text{target}}} - \frac{d\phi_{t_{ref}}(R)}{dH_{\text{target}}} \right|. \tag{2.8}$$

Here, the variability of target heights can be quantified as the spread of the distribution of target heights ($\sigma_{H_{\text{target}}}$). Figure 2-5 shows $\sigma_{\Delta\phi}$ computed from (2.8) using simply a spread of target heights of $\sigma_{H_{\text{target}}} = 10$ m. Because from (2.8) the uncertainty grows linearly with $\sigma_{H_{\text{target}}}$, the variability of phase differences here is only a result of the changes in *dn/dh* between the observed and the reference time. The phase variability increases as 1) *dn/dh* departs from that of the reference time and 2) targets are located at farther ranges.

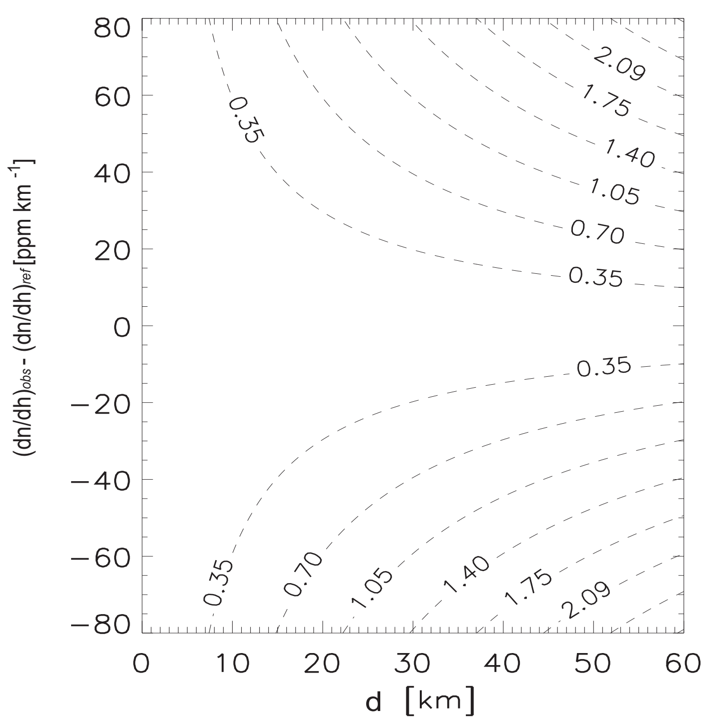

Fig. 2-5: Contour plot of the variance of phase measurements in radians as a function of $(dn/dh)_{obs} - (dn/dh)_{ref}$ and the distance along the arc surface for a target height variability of 10 m. Note how even a very modest $\sigma_{H_{\text{target}}}$ of 10 m results in considerable phase variance.

This sensitivity of the phase data to propagation conditions encouraged us to predict expected phase noise by carrying a more rigorous analysis. If all of the noise is predictable by these factors, then we can correct it to improve refractivity retrieval. Hence, we designed a phase simulator based on the equations derived above coupled with the determination of a target height distribution and the estimation of different *dn/dh* values. Predictions of phase noise made by the simulator will be compared with the observed phase noise, allowing us to evaluate its skill.

2.3. Phase simulator

The refractivity retrieval uses relative differences between the observed phase differences with respect to those made at a reference time. Hence, a phase simulator has been developed to compute phase differences $\Delta\phi$ with respect to the reference phase and to test the effect of propagation conditions (characterized by *dn/dh*) on the noisiness of $\Delta\phi$. Based on (2.7), for a given target location in terms of radar range R, the phase differences can be determined as

$$
\begin{aligned}
\Delta\phi = \phi(R,t) - \phi_{t_{ref}}(R) = \frac{4\pi f}{c}\left[\overline{n(t)}R - \overline{n\left(t_{ref}\right)}R_{t_{ref}}\right] \\
+\frac{4\pi f}{c}\left(H_{target} - H_{radar}\right)\left[\left(\frac{dn}{dh}\right)\frac{R}{2} - \left(\frac{dn}{dh}\right)_{t_{ref}}\frac{R_{t_{ref}}}{2}\right] \\
-\frac{4\pi f}{c}\left\{\left(\frac{dn}{dh}\right)\left[\frac{1+(E_r+H_{radar})\left(\frac{dn}{dh}\right)}{12(E_r+H_{radar})}R^3\right]\right. \\
\left.-\left(\frac{dn}{dh}\right)_{t_{ref}}\left[\frac{1+(E_r+H_{radar})\left(\frac{dn}{dh}\right)_{t_{ref}}}{12(E_r+H_{radar})}R_{t_{ref}}{}^3\right]\right\}
\end{aligned}
\qquad (2.9)
$$

As we see on the right-hand-side (rhs) terms of (2.9), phase differences depend on three factors: i) the radial (horizontal) change of refractivity (the first term), ii) the target alignment with respect to the radar associated with a constant *dn/dh* (the second term), and iii) the ray curvature relative to the curvature of the Earth (the last term). The three terms depend on $(dn/dh)_{t_{ref}}$ at the reference time and (dn/dh) at the time of interest. In practice, to compute each term, we require the following information:

- the path averaged refractivity $\overline{n(t)R}$ for observation and $\overline{n(t_{ref})R_{t_{ref}}}$ for reference times between the radar and given targets;
- the vertical gradient of refractivity (dn/dh) for both observation and reference times; and
- the location and height of targets (H_{target}) within the radar domain.

Because it is not straightforward to measure these directly, let us describe the following approach to obtain each element based on the observations available during IHOP_2002.

a. Path-averaged refractivity

One should remember that the path-averaged refractivity at an observed time $\overline{n(t)R}$ of the first term on the rhs of (2.9) is the variable to be retrieved with the refractivity retrieval algorithm. Thus, the true value of $\overline{n(t)R}$ is not known in advance. Instead, what we know is the average aliasing rate of measured phase differences due to the spatial average of the refractivity difference over the radar domain. This means that the spatially averaged refractivity difference will be a good estimate of the path-averaged refractivity as long as the refractivity fields are uniform at both reference and observation times (as in the example of Fig. 2-1). Otherwise, we should include the spatial variability of differences in *N*. Fig. 2-6 shows an example of the observed aliasing pattern of azimuthally averaged phase differences within a 40-km range (dotted line) for the same time as Fig. 2-1. The fit aliasing rate (solid line) results in a difference of about 14 between the observation and the reference times. However, although some ranges seem to have aliasing rates similar to the fit, others are totally mismatched. Because our goal is to simulate the phase field as close as possible to reality, the variability of the refractivity field should also be considered in the simulation. Hence, we used the retrieved refractivity fields to characterize the local departures from the spatial mean. It is not a desired approach to reuse the retrieved fields, but this is a realistic way to consider the spatial variability of differences in *N*.

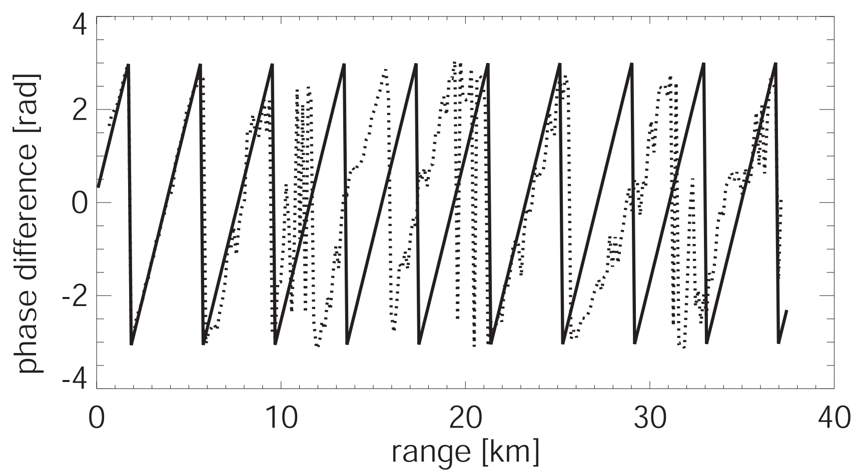

Fig. 2-6: The azimuthally averaged phase difference (dotted line) between time of interest (2332 UTC 15 May 2002) and the reference (2027 UTC 14 May 2002) as a function of range. The solid line is the best fit to this observed phase difference over 40 km in range, resulting in a mean refractivity difference of about 13.7 within the 40-km domain.

b. Sources of the vertical gradient of refractivity (*dn/dh*)

Sounding measurements are used to characterize propagation conditions by estimating *dn/dh* from pressure, temperature and humidity. During IHOP_2002, several radio soundings were available from different instruments. The Homestead site, located 16 km away from the S-Pol radar, had an Integrated Sounding Systems (ISS) and a mobile research vehicle AERIBAGO equipped with an AERI (Atmospheric Emitted Radiance Interferometer) instrument; ceilometer; surface stations; radiosonde; and GPS antenna measuring total precipitable water. Mobile facilities and aircraft launched soundings were also available within the radar domain (Weckwerth et al. 2004).

For the simulator, the values of *dn/dh* were assumed to be constant for both the reference time and the time of interest. The reference times during IHOP_2002 are those used for calibration in the refractivity retrieval algorithm: between 2010 and 2040 UTC 14 May 2002 for dry conditions, and between 0830 and 0900 UTC 21 May 2002 for wet conditions. Since no radiosonde sounding is available at these times, we have used the retrieved soundings from AERI observations. The AERI retrieval has been obtained through inversion of the infrared transfer equation (Feltz et al. 2003) and derived with a high temporal resolution (less than 10 min) at discrete heights (e.g., around 44, 87, 130 m, etc.) Because we are interested on propagation conditions near the ground, a representative value of *dn/dh* at 65 m has been computed with N at the level between 44 and 87 m. Then, we have extrapolated this estimated *dn/dh* to a value at the level of 33 m AGL. We have used such low-level estimates because conditions near the surface have the most effect on phase measurements from ground targets.

c. Target height simulation

The simulation of phase differences requires the location, heights, and number of ground targets that are neither moving nor changing their apparent shape. Note that the target height (H_{target}) in (2.9) includes the terrain height above MSL and the target height above the ground. Terrain height can be easily obtained from a digital elevation model (Fig. 2-7a around the S-Pol radar during IHOP_2002). Although it is difficult to know the exact location and height of targets within the radar domain, it is known that the area of the Great Plains has targets such as farm barns, water towers, and power poles that are generally lower than 30 m tall. We hence need to determine the height distribution of targets within a typical radar pixel that only contain fixed ground targets.

We have chosen these pixels based on a quality index (QI). The QI is composed of (i) the echo strength estimated at the 0° elevation angle during the dry calibration time (from 2010 to 2040 UTC 14 May) and ii) the reliability index (RI) used to characterize the stationarity of the target (Fabry 2004). The echo strength is determined by analyzing radar-backscattered power in terms of the norm of I and Q (NIQ) in decibels computed as

$$NIQ = 10\log\left(\left|\mathbf{X}_i\right|\right), \tag{2.10}$$

where $\mathbf{X}_i = \sum_{k=1}^{M} \mathbf{x}_{i,k}$ for M samples of the complex $\mathbf{x}_{i,k}$ (I, Q) signal over the pulse width (~1 μs) at the ith range gate. Higher values indicate strong echoes likely from ground targets. Hence, we have first established that values of NIQ exceeding -20 dB are returned from fixed ground targets. Note that NIQ is only the instantaneous signal strength, and so does not provide target reliability.

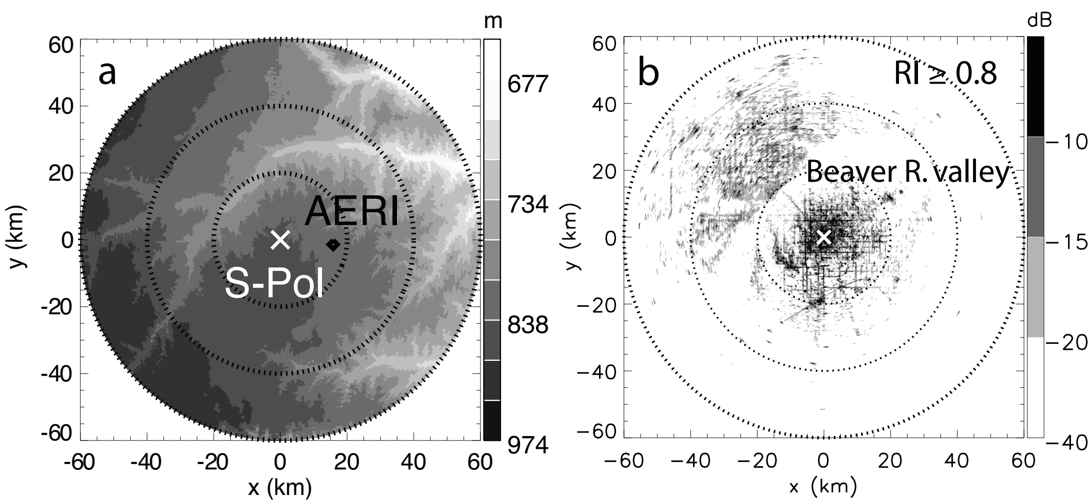

Fig. 2-7: (a) Topography map generated with the National Elevation Dataset of the USGS (with a resolution of 1 arcsec, approximately 30 m in space) within 60 km of the S-Pol radar. (b) The map of the NIQ (larger than -20 dB) combined with RI (larger than 0.8) observed at 2027 UTC 14 May 2002, when the reference has been prepared for the refractivity retrieval. The radar detects well many targets near range (~10 km) and on higher terrain (e.g., the northern western area). The Beaver River valley in northern east area is not seen by the radar because of its lower elevation.

Therefore, the reliability index (RI) between 0 (bad) and 1 (good) has been also obtained as a measure of the coherence of *NIQ* as

$$RI = \frac{\left|\sum_{i=1}^{s} \mathrm{X}_i\right|}{\sum_{i=1}^{s} \left|\mathrm{X}_i\right|} \tag{2.11}$$

from *S* scans at the 0° elevation during a period of frequent scan every 1 min instead of the usual complete volume scan every 5 min (e.g., from 1849 to 2027 UTC May 16 during IHOP_2002). Then, the QI is assigned at each radar pixel as "1" for "good" targets and "0" for the rest using a high threshold of RI (larger than 0.8) at the reference time defined above and the *NIQ* larger than -20 dB. For example, Fig. 2-7b shows the *NIQ* field filtered with the field of QI. The selected area of *NIQ* corresponds well to the area of higher terrain around the radar (Fig. 2-7a).

From this information, we have inferred the distribution of the heights of solid ground targets within the radar domain as follows. First, solid targets are identified based on QI. In parallel, we have simulated the minimum detectable height (see section 2-2b and Fig. 2-4a) over the radar domain; if a target is observed at a radar pixel (150 m in range by 1° in azimuth) with a given *MDH*, that pixel must contain a target higher than the MDH.

For consistency, the simulation has been performed using the propagation conditions estimated for the fast scanning period (during which RI was obtained). Hence, we have used a value of *dn/dh*=20 ppm km^{-1}, which is obtained from AERI measurements on from 1948 to 1957 UTC 16 May 2002. In the simulation, the height of the radar and the propagation conditions plays an important role. Considering the size of the antenna dish of S-Pol (~10 m) and of its supporting structure, the radar height is estimated to be 15 m above the ground (893 m MSL at the S-Pol site). Figure 2-8a shows the result of the simulated MDH map. Areas in black (0 m) indicate where the lowest ray hits the ground, which correspond well to areas with high ground echo intensity of Fig. 2-7b.

By combining identified targets with MDH values, we have estimated the probability of having a target higher than H_{target} within a pixel as shown in Fig. 2-8b:

$$P(H_{target} \geq MDH_i) = P(NIQ \geq NIQ_{min} \mid MDH_i \leq MDH < MDH_i + \Delta) \tag{2.12}$$

where i indicates the split of a target with the height interval of Δ=1 m from 0 m to the maximum value of MDH above the ground, and NIQ_{min} is the threshold on NIQ used to identify solid targets. We estimated the probability of having a target of a certain height in a pixel of the domain by differentiating (2.12) with respect to the height interval as:

$$\begin{aligned} &P\left(MDH_i \leq H_{target} < MDH_i + \Delta\right) \\ &\qquad = \frac{P(H_{target} \geq MDH_i) - P(H_{target} \geq MDH_i + \Delta)}{\Delta} W_m, \\ &\text{where} \quad W_m = \left[\frac{1}{1 - P(H_{\mathrm{target}} \geq \mathrm{MDH}_i + \Delta)}\right]. \end{aligned} \tag{2.13}$$

Here, W_m is a correction term that considers the possibility of having multiple targets within a single radar pixel. Figure 2-8c shows the histogram of target heights obtained over the S-Pol domain (up to 60 km in range) as a function of target height. As expected in the Great Central Plains (and mostly everywhere else), low targets are much more frequent within the radar domain.

Note that the distribution of Fig. 2-8c is used to simulate the location and height of targets within the radar domain under the assumption that targets are uniformly distributed in space. However, in reality they are quite randomly distributed. To compensate for this, we consider a possibility of having more than one target per pixel. So, the number of targets of a certain height in each pixel is randomly generated based on a Poisson distribution (Kalbfleisch 1985). The expected value of the distribution for each height is set according to the frequency obtained in Fig. 2-8c. In our case, the simulated number of targets resulted in mostly one and rarely two per pixel from continuous (in space) targets detected near the radar seen in Fig. 2-4a.

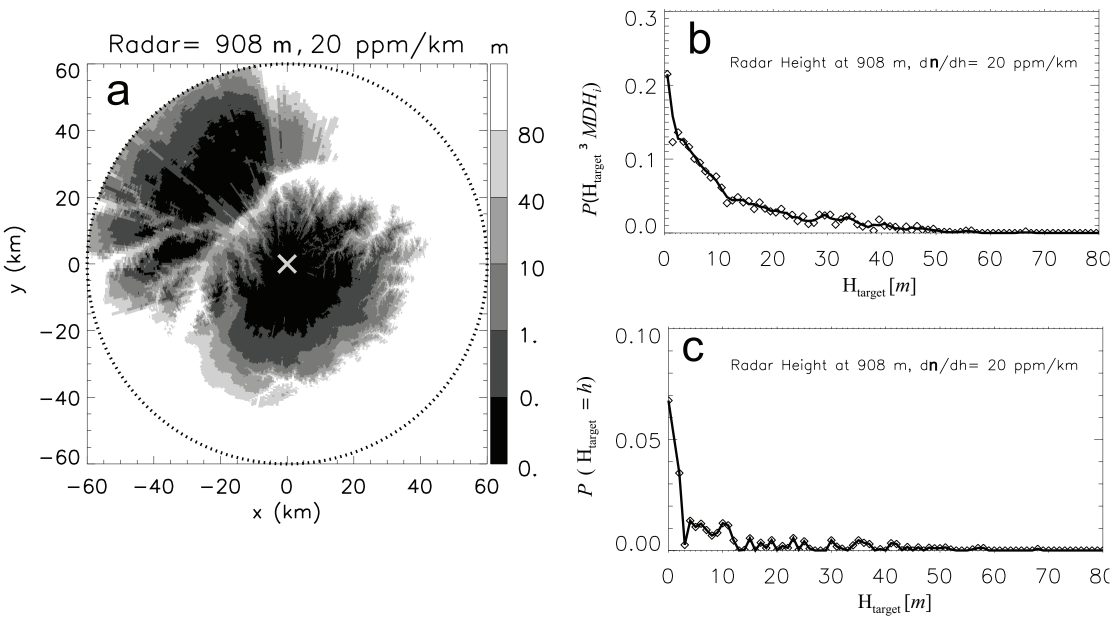

Fig. 2-8: (a) MDH map; the terrain height is subtracted from the lowest ray height assuming that *dn/dh* is 20 ppm km^{-1} as obtained from AERI soundings (located near 'AERI' in Fig 2-7a) at 19:48~20:20 UTC 16 May 2002. (b) Probability of having radar pixels at larger than a certain height over the pixels of good targets (as determined by the *NIQ* and RI thresholds over the radar domain: −20 dB and 0.8, respectively): $P(\mathrm{H}_{target} \geq \mathrm{MDH}_i)$ as a function of target height (in square). This probability is smoothed (solid line) to avoid any negative probability. (c) Probability of having a target at a specific height, $P(\mathrm{H}_{target} = h)$, using the smoothed result from (b). This probability is applied to the radar pixel given as 150 m in range and 1 ° in azimuth to assign target numbers and heights in the pixel.

Phase returns from simulated targets are computed by averaging (2.9) for all the heights where the target is visible (with the height resolution of 1 m) according to

$$\overline{\phi(R,t)} = \tan^{-1}\left[\frac{\sum_{i=MDH_i}^{H_{target}} \sin(\phi_i)}{\sum_{i=MDH_i}^{H_{target}} \cos(\phi_i)}\right]. \tag{2.14}$$

If the simulated ray intercepts multiple targets within a radar pixel, the phase returns from that pixel are averaged in a similar manner.

2.4. Validation of the phase simulator

The validation of phase differences simulated with (2.9) can be done by comparison with phase differences from real observations. This section presents two cases chosen because of the availability of 1) the values of mean refractivity difference and 2) *dn/dh* soundings. All radar measurements (i.e., phase, and retrieved refractivity) are obtained at 0° elevation angle and averaged over 15 min. This can help mitigate measurement noise that may introduce additional complexity in the comparison. Also, only radar pixels with high QI are considered (as described in section 2-3c), which guarantees that only solid targets have been used. Since ground targets are expected to be better observed at near range than far range, we present results up to 10 km in range based on the density of high *NIQ* seen in Fig. 2-7b; we also found that results obtained beyond 10 km range did not add any insight to the analysis to follow.

The comparisons are performed in terms of phase differences between reference time and time of interest. Since these fields are noisy, in order to see better their patterns, we compute the local average of phase differences ($\overline{\Delta\phi}$) over areas of 2.4 km in range by 10° in azimuth around each pixel:

$$\overline{\Delta\phi} = \tan^{-1}\left(\frac{\overline{\sin\Delta\phi}}{\overline{\cos\Delta\phi}}\right) \tag{2.15}$$

Also, we compute the variability expressed as the local standard deviation $\sigma_{\Delta\phi}$ for directional data followed by Weber (1997):

$$\sigma_{\Delta\phi} = \sqrt{-\ln[\overline{\sin(\Delta\phi)}^2 + \overline{\cos(\Delta\phi)}^2]}. \tag{2.16}$$

This formula is similarly used to estimate Doppler spectrum width (Lhermitte 2002). The size of the area considered (2.4 km by 10°) was chosen to be large enough to obtain proper statistics in (2.16) while remaining small enough not to be influenced unduly by changes of *N* in space.

a. Case1: 2332 UTC 15 May 2002

This is the case already analyzed throughout the paper (see section 2-2). The reference refractivity field is the one used for dry conditions at 2027 UTC 14 May 2002. In Fig. 2-1, we could identify ring like patterns in the phase difference data. This pattern corresponds to a spatial mean difference of refractivity of about 13.9, as shown in the fitting exercise of Fig. 2-9a. The fit matches well with the observation up to 6 km but varies beyond that range. This inhomogeneity is partly reflected on the retrieved *N* difference field showing a west-east gradient and some small-scale variability at ranges beyond 6 km (Fig. 2-9b). For the propagation conditions, we have used the values of near surface *dn/dh* estimated from AERI soundings (see its location in Fig. 2-7a): 62 ppm km^{-1} for the reference time and 25 ppm km^{-1} for the time of interest (Figs. 2-8c and 2-8d, respectively). Both periods had subrefractive conditions and show some variability of *dn/dh* in the vertical.

With the estimated propagation conditions at the reference and observation times, the simulations of phase differences are presented considering the three terms of (2.9) additively. In other words, simulation 1 includes only the radial change of refractivity, simulation 2 adds the influence of target heights associated with a given *dn/dh* at observation time. Finally, simulation 3 gathers simulation 1 and 2 as well as the effect of ray curvature depending on *dn/dh*. Figure 2-10 shows the comparisons between the three simulations and observations in terms of phase difference (Fig. 2-10a), spatially averaged phase differences (Fig. 2-10b), and local phase variability (Fig. 2-10c). First of all, the coverage of targets visible in the simulated fields of phase differences is in reasonable agreement with the coverage of targets in the observations. Although the patterns in the observations are patchier than in the simulations, their aliasing patterns resemble each other. For example, the ring patterns are skewed toward the West due to the presence of the east-west gradient of refractivity mentioned earlier. Hence, the simulator has produced more realistic results than those presented in Fig. 2-1a, where rings are purely concentric because the N difference field is considered uniform. In terms of the noisiness of the phase difference fields, the smooth simulated fields show some small-scale wavy patterns and similar values of standard deviation as the observations (Fig. 2-10b and Fig. 2-10c, respectively). If we focus on the simulations in Fig. 2-10c, the variability becomes slightly larger in simulation 2 which includes target information, than in simulation 1 where only the effect of the horizontal refractivity field is considered. Finally, simulation 3 is almost identical to that in simulation 2. This is not surprising at this near range because the third term of (2.9) is only significant at far ranges. From this case, the simulation seems to show some skill in reproducing noisiness. However, note that this case showed relatively large mean refractivity differences (of around 13.9) between the reference and the observation times. This might be responsible for a significant part of the variability of the phase difference fields. Hence, we have chosen another case with an observed mean refractivity similar to that at the reference time to better illustrate the impact of the propagation factors on the simulated phase differences.

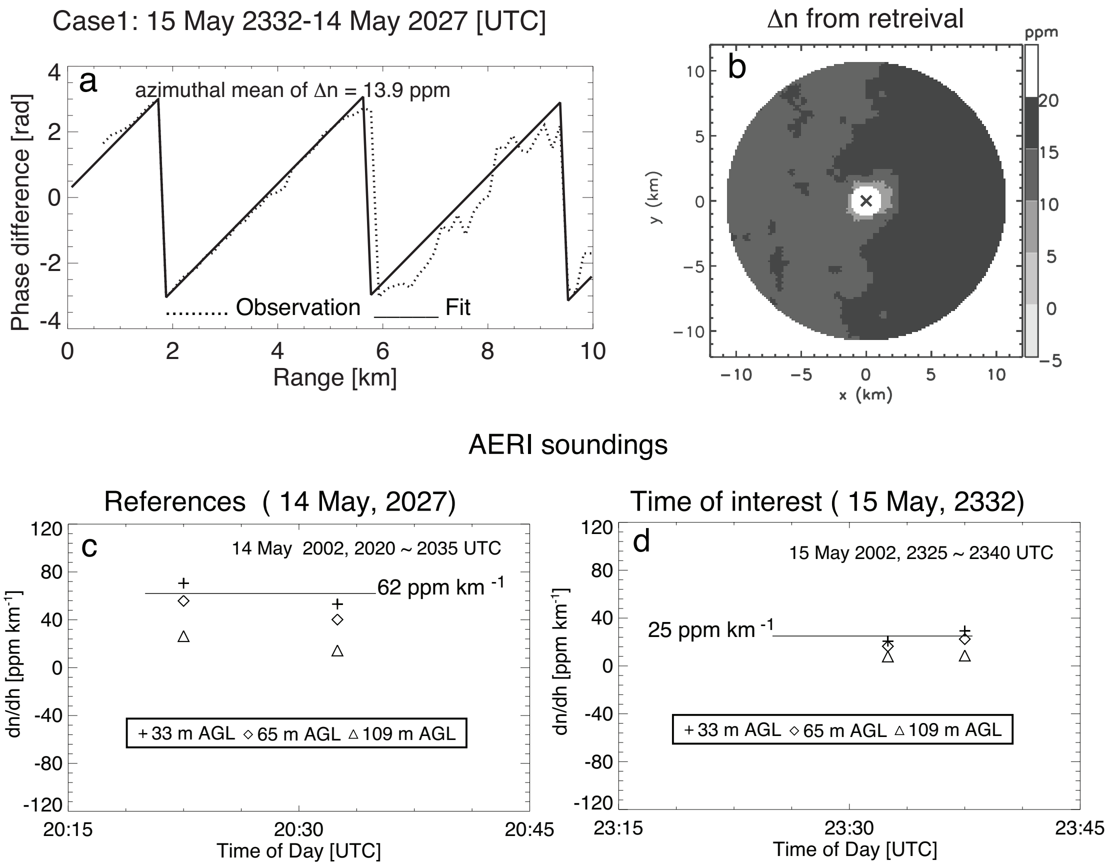

Fig. 2-9: Results for case1. a) Phase differences between 2332 UTC 15 May and 2027 UTC 14 May (reference time). Data are azimuthally averaged up to 10 km (dotted line). The solid line is the fit to the observations; aliasing every 3∼4 km indicates a uniform change of 12∼14 of the mean refractivity over the domain. (b) Retrieval field of refractivity differences between the time of interest and the reference. We only plot the area beyond 1.2 km due to the low quality of the near –range data. (c) Here, *dn/dh* estimated from the AERI soundings at the reference time (averaged over 15-min period scans; from 2020 to 2035 UTC) and at low levels (e.g., 65, 109 m AGL). A representative value (62 ppm km^{-1}) is obtained by extrapolating *dn/dh* at 65 m to the lowest level of 33 m and averaged in time. (d) As in (c) but for the time of interest.

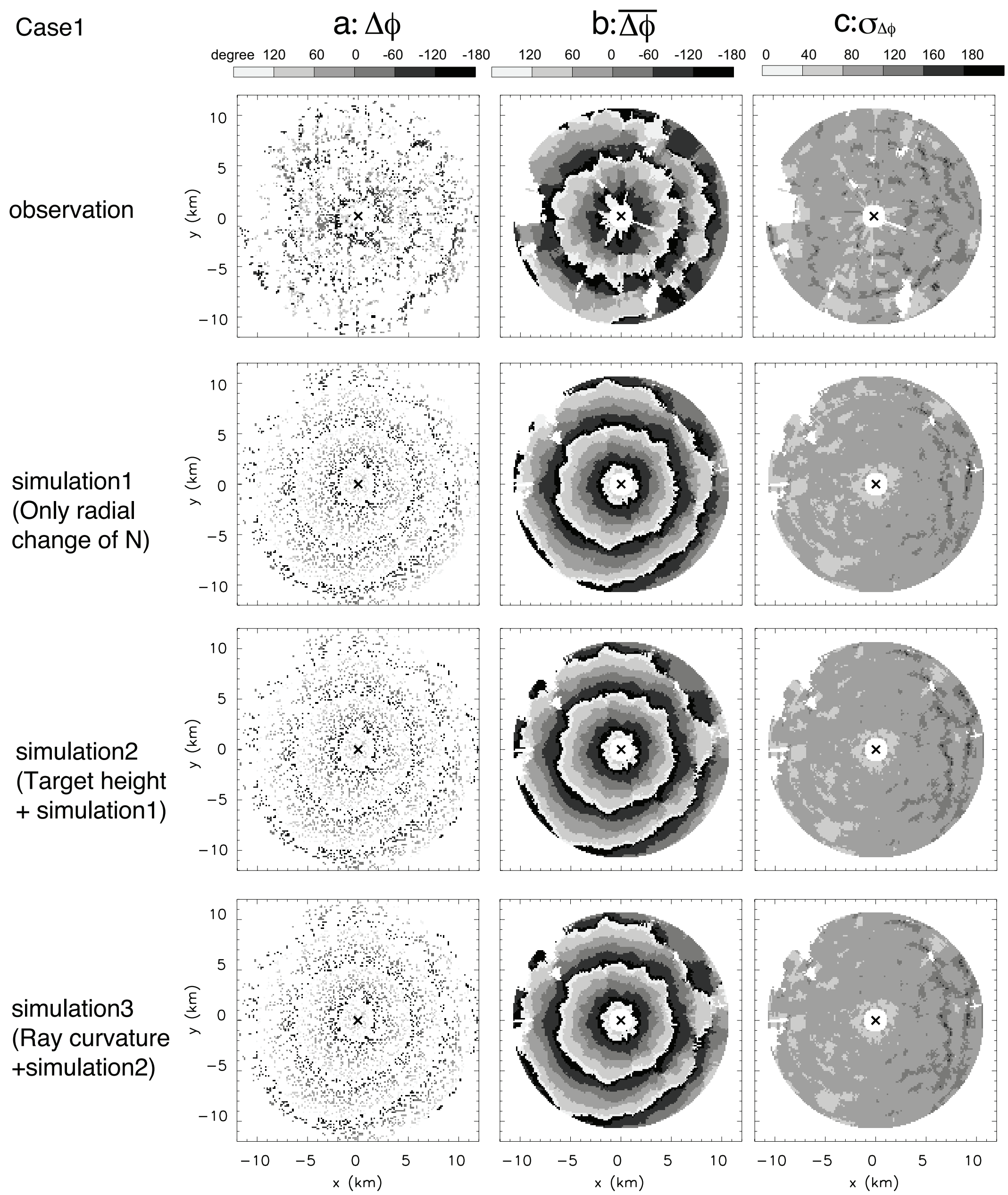

Fig. 2-10: Comparison between the observation and the simulation for case 1. (a) phase difference, (b) its local average, and (c) the variability over an area of 2.4 km in range by 10° in azimuth are shown (top to bottom). Each row shows the results from the observations, simulation 1, simulation 2, and simulation 3.

b. Case2: 1850 UTC 16 June 2002

The time of interest (1850 UTC 16 June) is selected because the phase aliasing rate (or the mean of ΔN) is very low, that is, the average refractivity is very similar to that of the reference time for wet conditions (0843 UTC 21 May). Figure 2-11a shows that the mean $d(\Delta\phi)/dr$ is much smaller than in the previous example (Fig. 2-9a), and its best fit yields a mean refractivity difference of about 0.56 up to 10 km in range. This small value is in good agreement with the overall refractivity differences of the retrieved fields (as seen in Fig. 2-11b). Unlike the dry reference time used in case 1, propagation conditions for this wet case are characterized by an almost constant vertical profile of *dn/dh* near the ground. The estimates of *dn/dh* are similar at each level of 33, 65 and 109 m, but slightly different between the reference and observation times (–37 ppm km^{-1} versus –52 ppm km^{-1} shown as Figs. 2-11c and 2-11d, respectively).

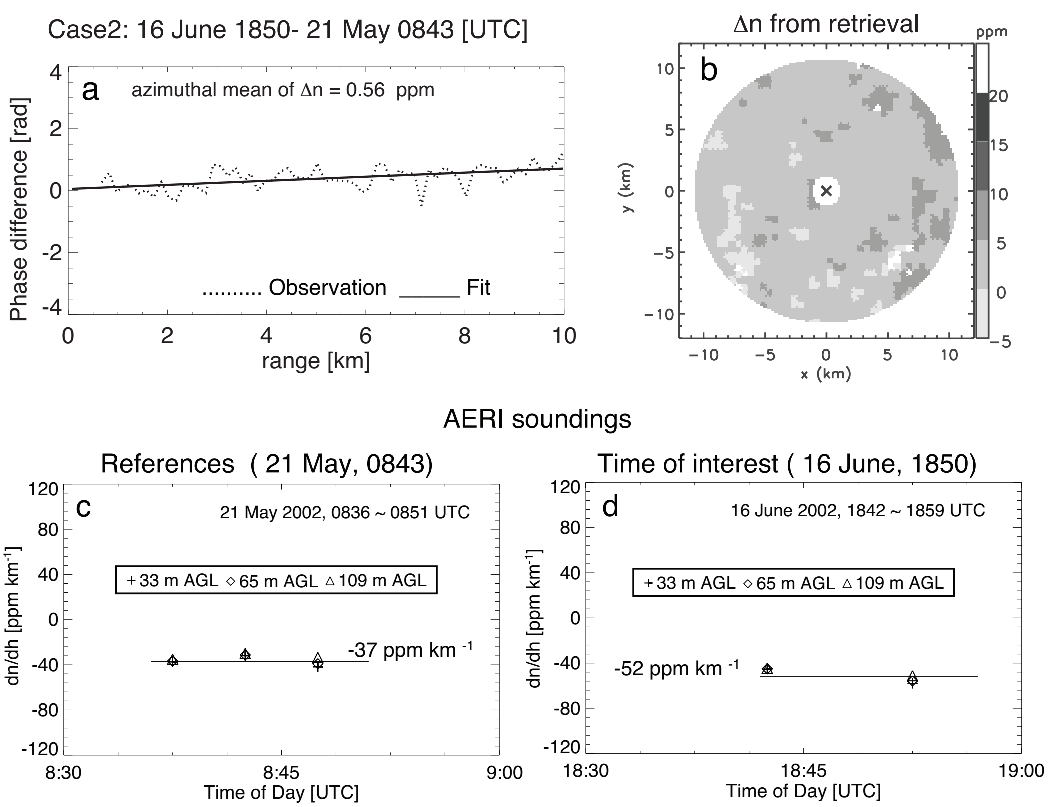

Fig. 2-11: As in Fig. 2-9, but for case 2 between 1850 UTC 16 June and 0843 UTC 21 May (reference time).

Observations and simulations for this case are presented in Fig. 2-12. The observed phase difference field (Fig. 2-12a) shows almost no aliasing pattern within 10 km in range. This is well reproduced in the three stages of simulation. The smoothed fields of Fig. 2-12b show that the simulated phase differences resemble the observations in general. The effect of target height and propagation conditions is also shown in Fig. 2-12c; simulations 2 and 3 are slightly noisier than simulation 1 and seem to have more impact at farther ranges (see around 10 km in range in the northeast area) than simulation 1. If the observation time had been more superrefractive, the simulated results would have been better obtained because the difference in *dn/dh* between the reference and observation times may play more in phase simulator. However, as seen in Fig. 2-12c, the variances of the simulated fields remain much smaller than those of the observations. For example, in terms of the root-mean-square error of $\sigma_{\Delta\phi}$ over the domain of 10-km range, we have obtained about 10° (70°) from the simulated (observed) fields.

From the simulation, therefore, we have learned that higher variability appears 1) with larger differences in the propagation conditions between the reference time and the time of interest and 2) at farther range. Nevertheless, we have not been able to approach the variability of observed fields that can be 7 times larger than those of simulated fields, especially for case 2. These large differences are observed at near range, where none of the terms of (2.9) are significant. Hence, the explanation for the noisiness in the phase data must lie elsewhere.

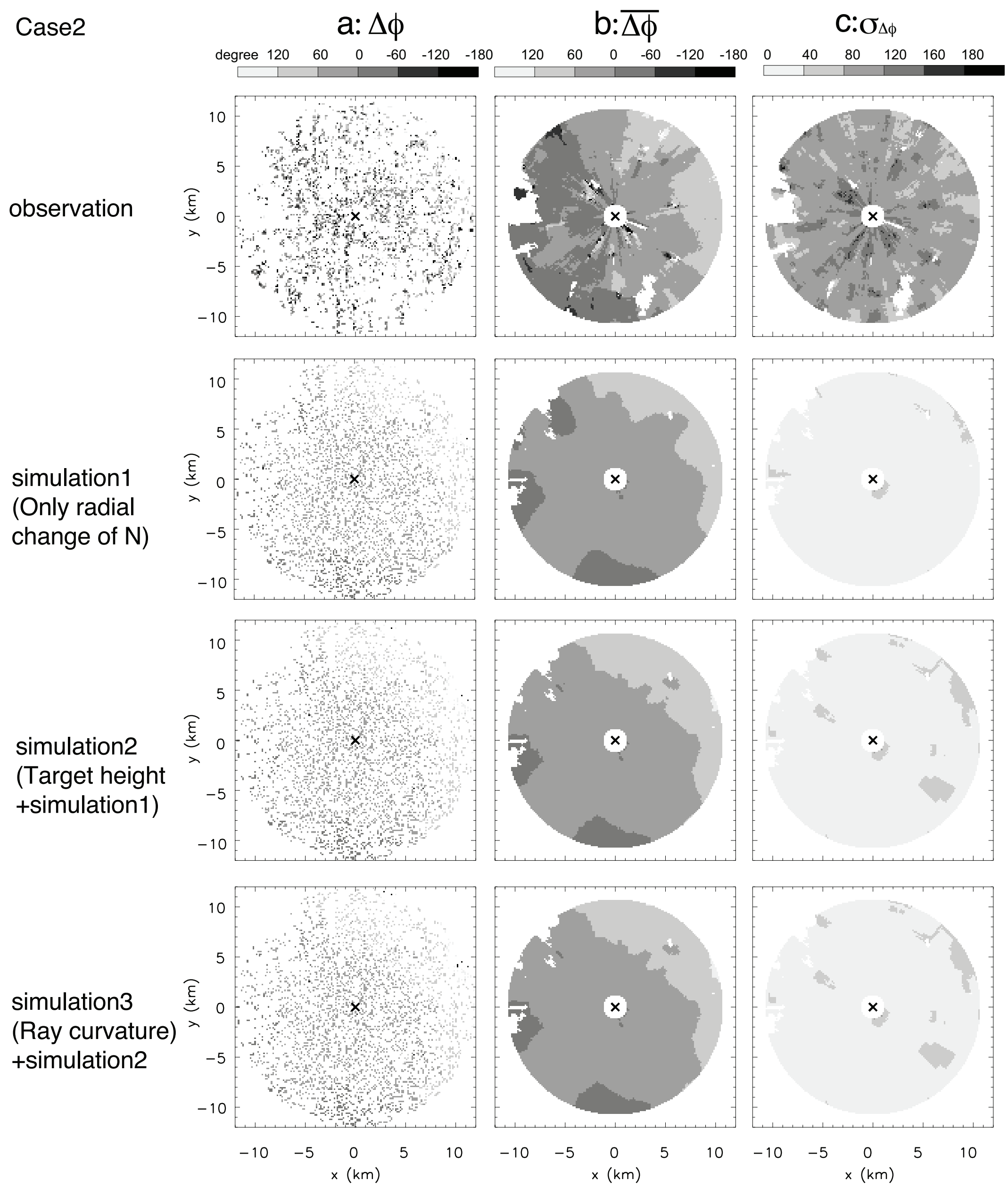

Fig. 2-12: As inFig. 2-10, but for case 2.

2.5. Conclusions

The phase measurements of ground targets used in the radar refractivity retrieval algorithm are often noisy, yielding ambiguous retrieval results. This paper has attempted to reproduce the noisiness of the phase measurements by rewriting the equations of the algorithm to include the change of ray trajectories to ground targets over complex terrain as a function of the propagation conditions. Observed phase differences were used to validate our simulations. From the analysis of two selected cases during IHOP_2002, we have seen that phase difference simulations are sensitive to propagation conditions. This effect would also be more significant at far range. However, the simulated results at near range where ground targets are denser and of "better quality" than those at far range suggest that the factor of dn/dh and the target height variability cannot fully explain the noisiness of observed phase differences. The reasons for the discrepancy could be due to factors not accounted in the simulation such as the following:

(i) Here, dn/dh obtained at a single location is used for the entire radar domain

(ii) The small-scale horizontal variability of refractivity at the reference time (supposed to be uniform in the simulator) remains still unresolved. Moreover, calibration times should be carefully selected on the basis of not only a horizontally uniform N but also on a uniform dn/dh near the ground.

Yet, these factors would not be sufficient to explain the noise in observed phase differences. Hence, other factors must also play a significant role. Our simulation lacked a full characterization of the complexity of ground targets, that is, the geometry and surface roughness of targets or the fact that they can move (for instance, overhead irrigators deployed in the farm fields or vegetation growth). Long-term ground observation of phase as well as echo intensity over the area of interest may help to ensure fixed ground targets and avoid moving targets. Furthermore, our simulator only includes single-ray backscattering and does not consider a full description of wave propagation. Multiple reflections of rays, diffraction behind the shadow regions have thus been ignored. All these can be factors introducing noise in phase difference observations. Their complexity makes their inclusion in the refractivity retrieval algorithm a challenge.

Acknowledgements

We would like to thank Prof. Isztar Zawadzki for many valuable comments. The authors are grateful to Dr. Marc Berenguer for his early review of the manuscript and numerous advices. We also thank Dr. Aldo Bellon for his insightful review. This work was possibly completed thanks to the Canadian Foundation for Climate and Atmospheric Sciences.

CHAPTER 3

Estimation of near-ground propagation conditions using radar ground echo coverage

We have seen on the phase simulator introduced in the previous chapter that the propagation conditions characterized by the vertical gradient of refractivity (*dN/dh*) were given by sounding instruments (e.g., radiosonde). Although the availability of the sounding at low-levels is often limited by its coarse temporal and spatial resolution or some erroneous measurement errors, such conventional soundings have been so far the most available source providing propagation conditions. Particularly, anomalous propagation conditions (e.g., large negative values of *dN/dh*) given by soundings have been often used to distinguish ground echoes from weather echoes for quantitative precipitation estimation (e.g., Steiner and Smith 2002).

In fact, the following work takes advantage of the relation between ground echo coverage observed by scanning radar (at low elevation angles) and near-ground *dN/dh*. Because little investigation of retrieving *dN/dh* from this ground echo coverage observations, we cannot stress too much about the worthwhile effort to improve such deficit of data availability based on existing radar measurements. Hence, a new method of estimating propagation conditions is presented and validated in this chapter consisting of a manuscript submitted to the Journal of Atmospheric and Oceanic Technology: Shinju Park and Frédéric Fabry (2010).

Estimation of near-ground propagation conditions using radar ground echo coverage

Shinju Park and Frédéric Fabry

Department of Atmospheric and Oceanic Sciences, McGill University, Montreal, Quebec, Canada

Abstract

The vertical gradient of refractivity (*dN/dh*) determines the path of the radar beam; namely, the larger the negative values of the refractivity gradient is, the more the beam bends toward the ground. The variability of propagation conditions significantly affects the coverage of ground echoes and, thus, the quality of scanning radar measurements. The information about the vertical gradient of refractivity is usually obtained from radiosonde soundings whose use, however, is limited by their coarse temporal and spatial resolution. Because radar ground echo coverage provides clues about how severe the beam bending can be, we have investigated a method that uses radar observations to infer propagation conditions with better temporal resolution than usual soundings.

Using the data collected during the International H_2O Project (IHOP_2002), this simple method has shown some skill in capturing the propagation conditions similar to these estimated from soundings. However, the evaluation of the method has been challenging because of 1) the limited resolution of conventional soundings in time and space, 2) the lack of other sources of data with which to compare our results, and 3) the ambiguity in the separation of ground from weather echoes.

3.1. Introduction

Propagation conditions of radar waves depend on the vertical gradient of refractivity (dN/dh, where $N = (n - 1) \times 10^6$, and n is refractive index of air) that varies with atmospheric pressure, temperature and humidity (Bean and Dutton 1968). For example, when N decreases with height (h) for a spherically stratified atmosphere, the radar rays passing through different layers of N bend according to Snell's law. The curvature of the bent rays can be approximated with the vertical gradient of refractivity (e.g., Doviak and Zrnić 1993). Hence, it is dN/dh that controls the trajectory of the radar beam. Considering the curvature of the Earth ($-dn/dh \sim 157$ ppm km^{-1}), propagation conditions are often classified in the following four categories; ducting ($dN/dh < -157$ km^{-1}; the beam gets "trapped" and bends toward the ground), super-refraction (-157 km^{-1} $< dN/dh < -79$ km^{-1}), normal refraction (-79 km^{-1} $< dN/dh < 0$ km^{-1}), and sub-refraction ($dN/dh > 0$ km^{-1}) (e.g., Barclay 2003). The occurrence of superrefractive conditions is usually associated with the following situations: (i) nocturnal radiation (triggering cool and moist air at the ground level), (ii) a gust front at the leading edge of a thunderstorm, and (iii) evaporation over the sea (Battan 1973; Atkinson and Zhu 2005). On the other end, sub-refraction occurs when the air density contrast is weak; e.g., cold air passing over warm sea near the Arctic or warm and moist air over cold and dry land surface (Battan 1973; Babin 1995).

Such propagation conditions affect scanning radar observations, particularly at low elevations:

(i) *The determination of the beam height at which weather/ground echoes are located*: The use of volumetric radar observations for QPE (Quantitative Precipitation Estimation) or assimilation into Numerical Weather Prediction (NWP) models (e.g., Pellarin et al. 2002; Bellon et al. 2007; Berenguer and Zawadzki 2008) or beam blockage mitigation/simulation methods for data quality control (Bech et al. 2003;

Kucera et al. 2004) require an estimation of the radar beam height, especially in mountainous areas (Germann et al. 2006). According to Doviak and Zrnić (1993), the beam height can be computed with a given *dN/dh*. However, due to the lack of measurements of *dN/dh*, normal propagation conditions (dN/dh = − 40 km^{-1} under the standard atmosphere) have been mostly used in those applications above.

(ii) Contamination by ground echoes: The more negative *dN/dh* becomes, the more the beam bends towards the surface and the more ground targets are reflected in radar measurements. As a result, the observed radar echo coverage at low elevation angle tends to increase. This can interfere with weather echoes near the ground that are often used for precipitation estimation. In this sense, the detection of ground clutter is a fundamental step in the chain of quality control algorithms applied to radar measurements to guarantee their meteorological relevance. However, the detection of ground clutter is a well-known challenge in the radar community and has been an active research area: ground detection and removal can be based on signal processing of raw data (e.g., Moisseev and Chandrasekar 2009) or on data processing of reflectivity data (e.g., Moszkowicz et al. 1994; Steiner and Smith 2002) and/or together with measurements of Doppler velocity (e.g., Berenguer et al. 2006; Cho et al. 2006; Hubbert et al. 2009). However, none of the works cited above included information about the propagation conditions in their methods for ground echo elimination.

(iii) *The quality of radar refractivity retrievals*: The radar refractivity retrieval algorithm is used to estimate moisture fields with high resolution in time and space (Fabry et al. 1997; Weckwerth et al. 2005). This technique has been utilized to understand thunderstorm initiation (Fabry 2006; Wilson and Roberts 2006; Roberts et al. 2008; Wakimoto and Murphey 2009).

However, the quality of its performance could be somewhat affected by propagation conditions that determine ray trajectories to ground targets over complex terrain (Park and Fabry 2010).

Hence, there is a certain need for better knowledge of propagation conditions as far as radar data quality is concerned. As mentioned above, however, very few instruments measure/estimate the vertical gradient of refractivity. Radiosonde soundings can provide useful estimates of propagation conditions, but their availability is limited in terms of temporal and spatial distribution (generally two a day at point sites separated by hundreds of kilometers). Besides, their estimates in the first few meters above the ground are often missing or unreliable because of instrumental, operator, or representativeness errors. And, as we will show in this work, propagation conditions very close to the surface are critical in determining the trajectory of radar beams.

To compensate for the lack of availability of conventional soundings, several studies have explored the use of different sources of information to estimate/provide the propagation conditions such as i) NWP model outputs to modify the refractivity profile observed at a given point (Bech et al. 2007), and ii) radar reflectivity patterns of free-precipitation observed under anomalous propagation (AP) in order to isolate the AP in the radar precipitation estimation (Moszkowicz et al. 1994). Also, different methods have been suggested to obtain propagation conditions for a given sounding in terms of i) a multi-layer ray tracing algorithm in the simulation of beam trajectory that affects radar volume and power distribution (Fornasiero et al. 2006), ii) the parabolic equations in some sea-clutter studies (Babin and Dockery 2002), and iii) the objective function composed of reflectivity at multiple elevation angles combined with Monin-Obukhov similarity theory (Gerstoft et al. 2003). These studies were, nevertheless, limited to marine atmosphere, involved expensive computations in the simulation of radar echo intensity, and required an initial sounding whose *N* would be modified.

The purpose of this paper is, therefore, to investigate an alternative method to characterize propagation conditions. During the field experiment of International H_2O Project (IHOP_2002) held in Oklahoma, the S-Pol radar collected ground echo intensity maps at the 0.0° elevation angle (see section 3.2). For given propagation conditions, section 3.2 also describes how we can simulate the height of detectable ground targets and ground echo coverage. The comparison of measured and simulated ground coverage forms the basis of the proposed method to extract near-ground propagation conditions (section 3.3). Section 3.4 discusses the verification challenges by analyzing ground echo coverage together with soundings available during the entire experiment. Selected results and analysis of their impact on beam height error are presented in section 3.5.

3.2 Measured and simulated ground echo coverage

a. Observation of ground echoes and propagation conditions

Radar ground echo intensity maps and soundings were collected over the domain of the S-Pol radar (up to a maximum range of 60 km) during early summer 2002 (Weckwerth et al. 2004). Fig. 3-1a shows the orography map around the radar generated from the National Elevation Dataset of U.S Geological Survey (with a resolution of 1 arc-second). To enhance the contribution of ground echoes, we have used the Norm of the Inphase and Quadrature vector, *NIQ*, a measure of echo strength defined as

$$NIQ_i = 10\log\left(\left|\mathbf{X}_i\right|\right), \text{ in dB,} \tag{3.1}$$

where $\mathbf{X}_i = \sum_{k=1}^{M} \mathbf{x}_{i,k}$, the sum of the M samples of the complex signal $\mathbf{x}_{i,k}$ (I, Q) received by the radar at the *i*-th range gate. This parameter is referred more rigorously in the literature with different names later such as Phase Quality

Indicator (PQI; Nicol el al. 2009) or the nominator of the Clutter Phase Alignment (CPA; Hubbert et al. 2009). Fig. 3-1b and 3-1c show the *NIQ* fields observed at different times on 14 June 2002. Both events had no precipitation within the radar domain, yet the coverage of *NIQ* shows distinct differences. The large echo coverage in Fig. 3-1b is possibly due to nocturnal radiative cooling (moist and cold air near ground) before sunrise, providing favorable conditions for super-refraction (or ducting). Less coverage is present in the *NIQ* field of Fig. 3-1c. This may be the result of subrefractive conditions caused by surface heating.

Meanwhile, propagation conditions can be estimated from sounding measurements. According to Bean and Dutton (1968), N is a function of pressure [P in hPa], temperature [T in Kelvin] and water vapor pressure [e in hPa] such as

$$N = 77.6\frac{P}{T} + 373000\frac{e}{T^2}. \tag{3.2}$$

Then, the vertical gradient of N dictates the propagation conditions. During IHOP_2002, soundings over the radar domain were obtained with the following instruments (Weckwerth et al. 2004): the Integrated Sounding System (ISS), the Atmospheric Emitted Radiance Interferometer (AERI), mobile sounding stations and aircraft. Unlike mobile and aircraft soundings, radiosonde soundings from the ISS and retrievals with the AERI were from a fixed site (Fig. 3-1a). Figure 3-1d presents the ISS soundings of dN/dh at the times corresponding to the radar scans of Figs. 3-1b and 3-1c. To remove small-scale fluctuations in the vertical, we have smoothed N estimates over 80 m in height (corresponding to 10 ~ 20 seconds in time for the radiosonde) and plotted data every 40 m up to 200 m above the ground. Here, dN/dh at very low levels (less than 80 m) is not plotted because near-ground sounding measurements are often missing or inaccurate. Then, it would be the nearest-ground propagation condition that mostly affects the radar returns from ground targets. Therefore, we focus on the first value of the soundings. For example, ~ –82 km^{-1} from the thick line in Fig.

1d indicates superrefractive conditions, which coincides with larger coverage of ground echoes in radar scans.

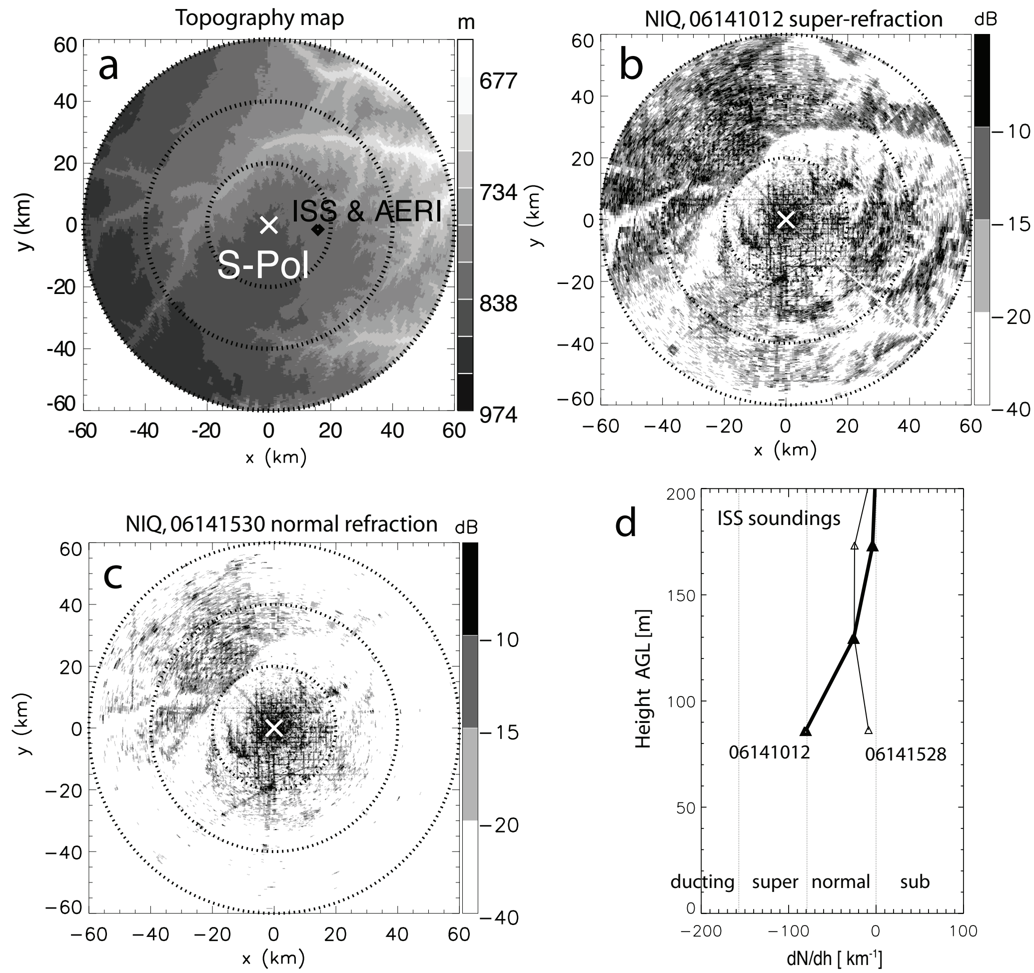

Fig. 3-1: (a) Orography map within a range of 60 km. Areas are overall flat, yet the Northwest area is higher than the East area. Next are shown the *NIQ* fields at the 0.0° elevation measured in (b) superrefractive (10:12 UTC or 04:12 local standard time) and (c) subrefractive (15:28 UTC) conditions on 14 June 2002. d) Vertical profile of *dN/dh* obtained from the Integrated Sounding System corresponding to the cases of (b) and (c).

b. Simulation of ground targets seen by the radar

Meanwhile, we can simulate the expected ground echo coverage by determining the areas where the radar beam intercepts ground targets for given propagation conditions. This requires determining radar horizon for given terrain heights. According to Doviak and Zrnić (1993), ray height can be computed as a function of *dN/dh*:

$$h(r) = \sqrt{r^2 + (R_e)^2 + 2rR_e \sin\theta} - R_e + H_r,$$
$$R_e = \frac{(R + H_r)}{1 + (R + H_r)\left(10^{-6}\frac{dN}{dh}\right)}, \tag{3.3}$$

where r is the radar measurable range, θ is the elevation angle of the ray considered, and H_r is the radar height. R_e is the equivalent Earth radius and is obtained from both the Earth radius (R) and the vertical gradient of refractive index. Note that (3) can and will be used not only for the center of the beam, but also for all the rays in the main lobes as well as the sidelobes. Then, using (3.3), the radar horizon is obtained by computing the lowest unblocked ray height as a function of *dN/dh*. Fig. 3-2a shows two examples of the lowest ray heights along the range over the terrain at the azimuth of the ISS soundings seen in Fig. 3-1a. In superrefractive conditions (e.g., dN/dh = –120 km^{-1}), the lowest rays bend more toward the ground and thus intercept the ground over a wider area than in subrefractive conditions (e.g., dN/dh = 20 km^{-1}). The minimum height of ground targets, H_t, that can be detected by the radar for a given *dN/dh* will be the height between the terrain and the lowest rays reaching the target's location. The black areas shown in Figs. 3-2b and 3-2c correspond to the areas where radar beams hit the surface. Otherwise, for a target to be observed by the radar in the area of grey or white, its height should be higher than the indicated values. Because the study area is relatively flat and agricultural, ground targets are virtually lower than 100 m above the ground (as discussed in Park and Fabry 2010).

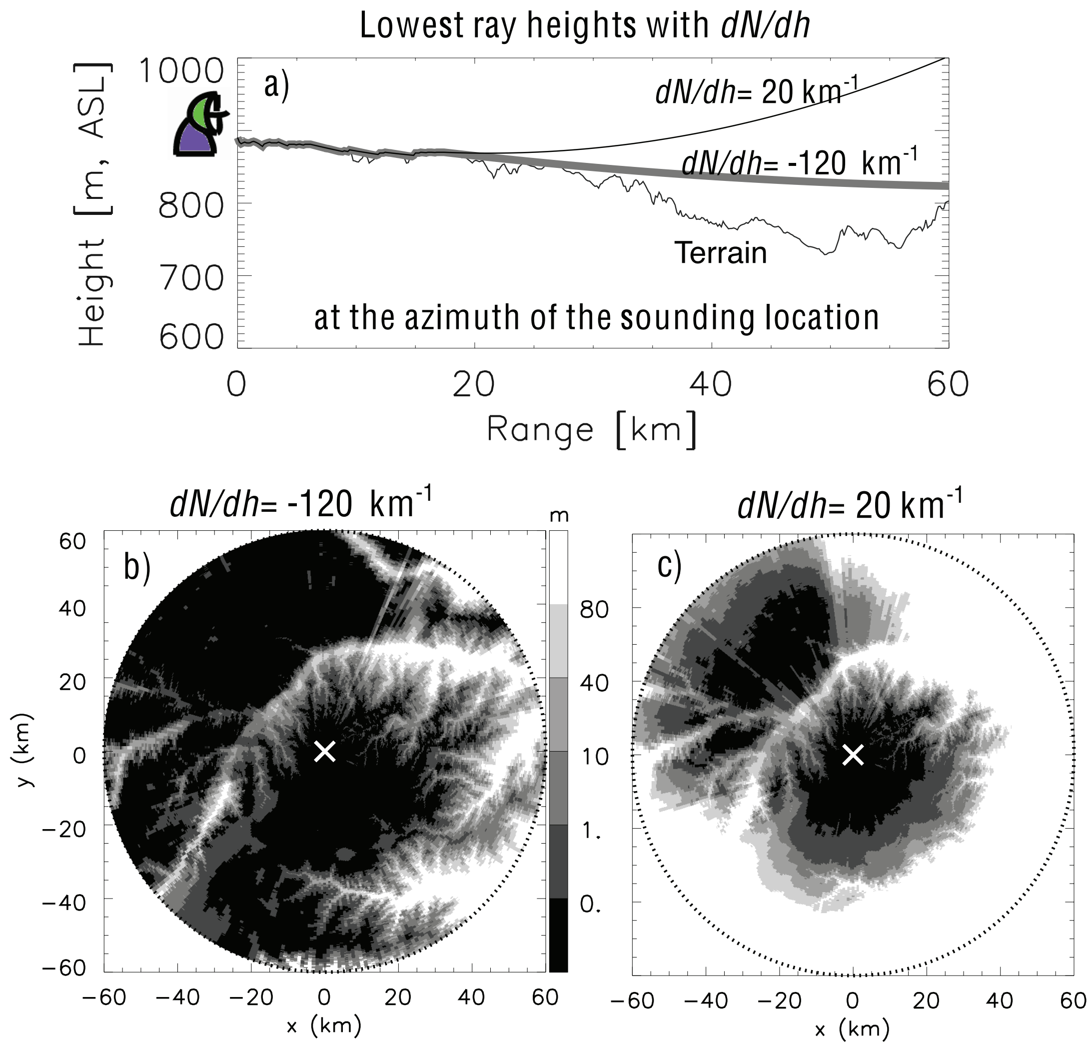

Fig. 3.2: (a) Illustration of the lowest ray height with range for two different *dN/dh*. Below are the associated maps of detectable ground target heights (H_t) for (b) super-refraction and (c) sub-refraction conditions.

3.3. Estimating *dN/dh* using radar ground echo observation

We have seen that the *NIQ* fields reflect the location of ground targets and show a clear dependence on propagation conditions. On the other hand, we have demonstrated how the height of visible ground targets can be simulated as a function of *dN/dh*. In Figs. 3-1 and 3-2, we can see certain correspondence between the coverage of high values of *NIQ* and the areas in which short targets are visible for different propagation conditions. Hence, the method proposed will retrieve the average *dN/dh* that results in the best match between the observed *NIQ* maps and the simulations of height of ground targets detectable by the radar.

a. Parameterization

For the comparison, we must realize that the variables observed and simulated are of significantly different nature (i.e., echo intensity and height above the ground, respectively), not to mention the lack of knowledge on the real distribution of ground targets within the radar domain (as discussed in Park and Fabry 2010). The *NIQ* observations are the primary source to determine where ground targets are. And the ground targets are supposed to be solid (e.g., railways, power poles, and the terrain…). However, in reality, the *NIQ* observations also include echoes from moving targets such as precipitation, vegetation swaying by winds and/or irrigators rotating whenever the farmers need. So, we have characterized the solid targets as those with *NIQ* values over a threshold of -20 dB. This value is somewhat arbitrary but good enough to discriminate fixed targets from moving targets and precipitation echoes without any additional constraint such as "zero" radial velocity. Now, one may assign 1 (ground targets detected) to the echoes with *NIQ* exceeding the threshold, and 0 (no ground targets detected) for *NIQ* values below the threshold. Instead, we have opted for a fuzzier target likelihood index defined as:

$$f_{obs}(NIQ) = \frac{10^{\frac{NIQ}{m}}}{10^{\frac{NIQ}{m}} + k \cdot \left(10^{\frac{NIQ\_thresh}{m}}\right)}, \tag{3.4}$$

where *NIQ_thresh* is set to -20 dB. Here, *m* and *k* are the weighting factors that determine the smoothness in the transition from "no ground target detected" to "ground target detected". For example shown in Fig. 3a, in this study, we chose the values of k=8 and m=6 to fuzzy the transition between "definitely a ground target" and "definitely not a ground target" given partial overlap *NIQ* values in precipitation and in ground targets. Then, from a real-time radar scan, we have used (3.4) to convert the observed *NIQ* field into the field of ground target detection index.

Now, when it comes to parameterize the possibility of detecting ground targets from the simulation, the challenge lies in how to define a target likelihood index f_{sim} to be comparable to and compatible with f_{obs}. We know that the observed coverage of ground targets would be influenced by the distribution of target heights. However, because such distribution is unknown, it is difficult to input proper target heights into the simulation of ground target coverage. One must remember that the simulation computes only the height of the lowest detectable target (H_t) as a function of *dN/dh* for a given terrain map. Therefore, we need to use, and hence determine, a function to map H_t into the field of target likelihood index for observing a target.

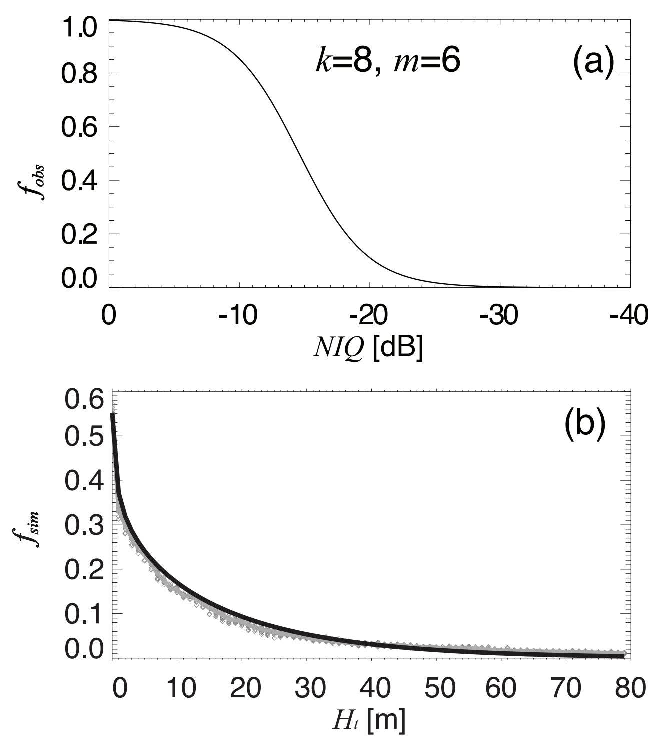

Fig. 3-3: Target likelihood indices: a) f_{obs} derived from observations as a function of *NIQ*; b) f_{sim} used in the simulation as a function of H_t. For 17 low-level scans from 1330 UTC to 1500 UTC on 14 June 2002, all the results of f_{sim} are in grey diamonds and their average is in grey thick line. Black line is the fit of this

average, which constitutes our parameterization of f_{sim} as a function of H_t.

To do this, we chose a period when dN/dh was known and constant. This allowed us to compute H_t for every radar bin (i.e., the size of 150 m in range and 1° in azimuth over 60 km in range) and compare it with f_{obs} measured. From the two maps of H_t and f_{obs}, we formulated f_{sim} as a function of H_t:

$$f_{sim}[H] = \left\langle f^*_{obs} \right\rangle_H , \tag{3.5}$$

where H is the increment of H_t being $H_i<(H=H_t)<H_i+\Delta H_t$ with the interval size $\Delta H_t=1$ m, f^*_{obs} is defined as a set of f_{obs} during a period of known propagation conditions, and $<>_H$ is the average of f^*_{obs} over radar bins satisfying H. Once this target likelihood index is determined, f_{sim} will be used as a "reference" to compute maps of expected target coverage from the simulated maps of H_t for all propagation conditions. For example, grey diamonds in Fig. 3-3b shows f_{sim} as a function of the minimum target heights (H_t) computed with cases chosen from the tethered atmospheric observation during IHOP_2002 when the values of dN/dh are between -50 km^{-1} and -60 km^{-1} from 1330 UTC to 1500 UTC on 14 June 2002 (see section 3.4b). Statistics of echo occurrence were computed for H_t up to 80 m above the ground. In Fig. 3-3b, the grey line is the average for all cases and the black line is the fit of this average that can be used as the reference target height statistic. We also assumed these height statistics within the radar domain remained constant during the entire period of IHOP_2002. Therefore, f_{sim} is in fact independent of dN/dh for each radar bin and a function of only H_t. However, because H_t changes for any dN/dh, a target likelihood index can be finally assigned to a radar bin corresponding to H_t

b. Optimization

We have parameterized the detectable ground targets in terms of indices introduced as (3.4) and (3.5) for both observation and simulation maps. To find the best match between two fields, we first tried to simply minimize the differences in terms of the least squares on a pixel-by-pixel basis. However, this approach did not show clear minima in the least square estimates because we know only the likelihood of observing a target, not their actual locations. Hence, we chose to minimize differences in the fields of target likelihood indices in terms of H_t and formulated a cost-function as:

$$J\left[\left(\frac{dN}{dh}\right)\right] = \sum_{i=0}^{79} \left\{ \left\langle f_{obs}(NIQ) \right\rangle_{H_i} - f_{sim}(H_i) \right\}^2 \cdot A(H_i) \quad , \tag{3.6}$$

where $A(H_i)$ indicates the number of radar bins satisfying the increment of H_t being $H_i < H_t < H_i + \Delta H_t$ with the interval size $\Delta H_t = 1$ m. Then, the optimization of (3.6) has been performed numerically with a quick downhill simplex method (Press et al. 1999).

3.4. Validation challenges

Before we look at the results obtained with the method presented above, the following should be addressed regarding the validation of *dN/dh* estimates:

(i) We have seen in section 3.2 that the proposed method was inspired by a few good agreements between observed coverage of ground echoes (targets) and simulated target heights given propagation conditions. How often do we actually observe such good agreement?

(ii) Soundings often provide the estimation of *dN/dh* at a point location, whereas radar estimates are obtained over the ground echo domain. How trustworthy are point measurements to verify radar estimates?

To answer these questions, we analyzed available data for the entire period of the IHOP_2002 experiments (for 45 days from 11 May to 26 June 2002).

a. Observations of ground echo coverage vs. sounding estimations of *dN/dh*

First, we plotted radar ground echo coverage (Fig. 3-4a) observed with a time resolution of about 5 minutes. The ordinate of this plot is percentage of area (within 60 km in range) with *NIQ* values exceeding -20 dB. As discussed previously, this threshold does not fully guarantee the complete removal of weather echoes, especially in those areas where clutter is embedded within precipitation and/or affected by heavy rainfalls. The domain size of 60 km in range is relatively small compared to the usual operational radar domain (120 km or 240 km in range). However, it shows better sensitivity to propagation conditions and, thus, results in a wide range of clutter coverage (the larger the size of the domain, the smaller the ground echo coverage). Note that the evolution of ground echo coverage in Fig. 3-4a presents a strong diurnal cycle independent on how low or high the percentage of coverage is. Yet, this does not mean that large coverage always occurs at night or early morning (i.e. when ducting conditions are favorable). In fact, only about 10 % of the radar scans during the entire period of the experiment show large echo coverage (see Fig. 3-4b). Because of this reduced number of samples, it is quite challenging to investigate how the evolution of the ground echo coverage matches the observed propagation conditions (*dN/dh*) in the context of the proposed method.

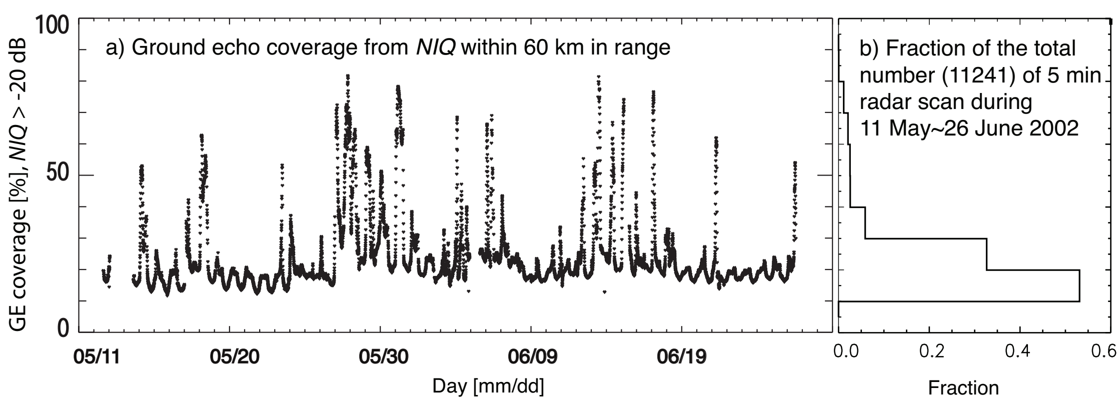

Fig. 3-4: (a) Time series of ground echo (GE) coverage with *NIQ* larger than -20 dB within 60 km range in %. b) Histogram of the ground echo coverage shown in a) during IHOP_2002.

Second, the estimates of *dN/dh* obtained from ISS observations during IHOP_2002 were usually limited in time and space and often uncertain near the surface (i.e., at levels below 100 m). To overcome the difficulties due to the low temporal resolution of radio soundings, we have used the AERI (Atmospheric Emitted Radiance Interferometer) retrievals of pressure, temperature and water vapor pressure sampled at a time resolution of 10 min or better (Feltz et al. 2003). Conveniently, the AERI was located at the same site as the ISS (Fig. 3-1a) and the retrievals were obtained whenever there was no rain. These soundings are retrieved through the radiative transfer equation provided with an initial guess based on available measurements of the AERI, surface stations, RUC (Rapid Update Cycle) model, and ceilometers. We have interpolated the low-level profiles of atmospheric variables from the AERI at 80 m and smoothed them over 30 minutes. Fig. 3-5 shows the comparison between AERI and ISS soundings (at around 80 m AGL) matched within a 5-minute time window. As we can see from the scatter plots, all variables agree fairly well. That being said, if we try to retrieve the height derivative of *N* from these measurements, small height dependent biases can strongly affect the outcome. Most of the scatter in *N* comparisons can be due to the differences in the humidity measurements (Fig. 3-5d). However, we are not fully certain about which instrument is better at measuring humidity and, thus, we have used AERI humidity measurements as retrieved.

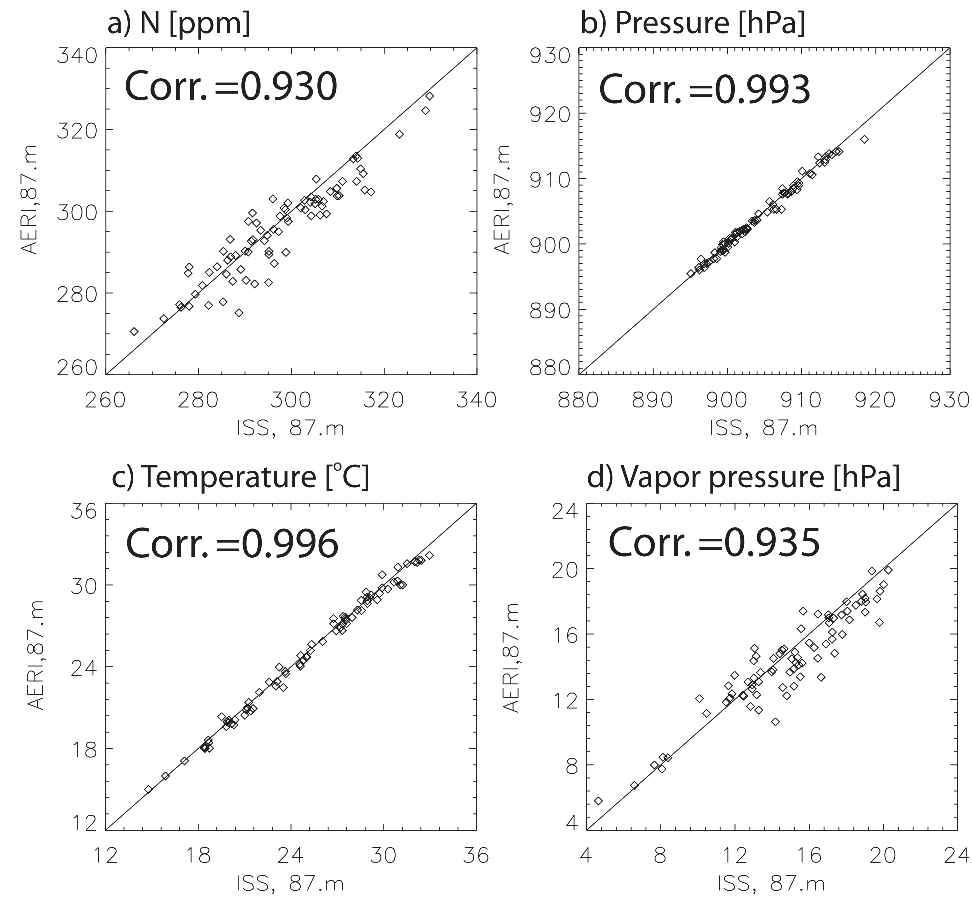

Fig. 3-5: Comparison of (a) estimated *N*, (b) pressure, (c) temperature, and (d) water vapor pressure between the AERI and ISS variables at 87 m AGL. High correlation coefficients (Corr.) suggest that AERI and ISS at this level agree well with each other.

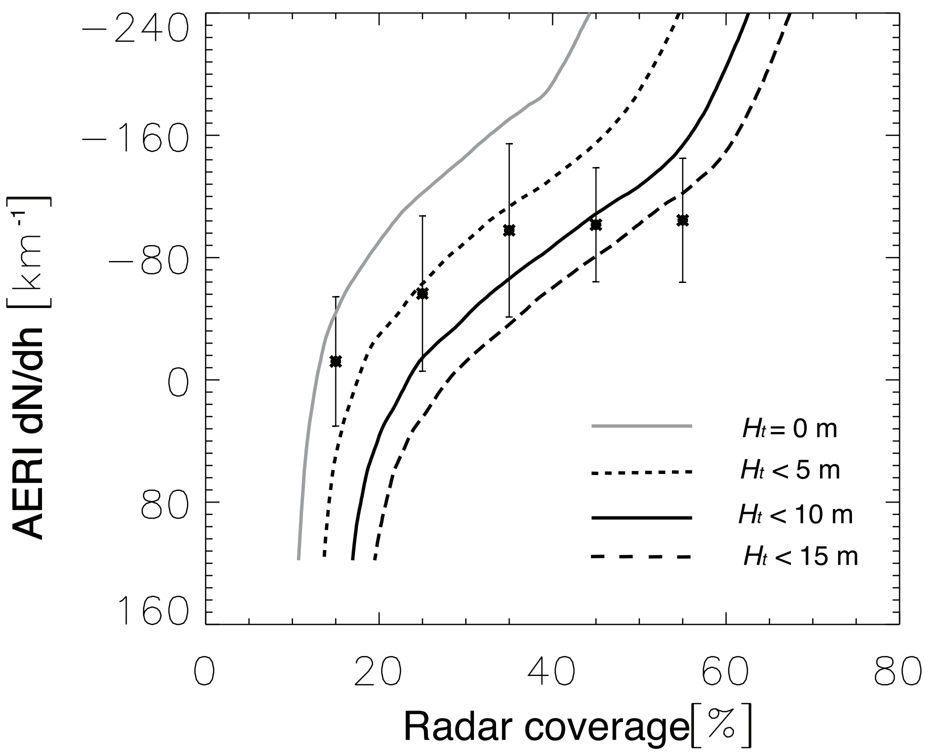

Fig. 3-6: Comparison between the observed radar ground coverage and the estimated *dN/dh* from AERI sounding observation during 45 days. The data points and bars are the average and standard deviation of 5-minute AERI *dN/dh* estimates over each 10 % intervals of ground echo coverage. The lines present the expected (simulated) area fraction as a function of *dN/dh* where the lowest ray does not exceed a certain height AGL; e.g., grey solid line for $H_t = 0$, short dashed line for $H_t < 5$ m, solid line for $H_t < 10$ m and dashed line for $H_t < 15$ m.

For the comparison between radar coverage and low-level propagation conditions estimated from soundings, we average 5-minute AERI *dN/dh* measurements as a function of the 10 % intervals of ground echo coverage in Fig. 3-4b. The result is shown as points in Fig. 3-6. The lines present the expected (simulated) area fraction within the radar domain where the lowest ray does not exceed a certain height AGL (e.g., 0, 5, 10 and 15 m depending on the maximum height allowed for the ground seen by the radar) as a function of *dN/dh.* We can see clearly that smaller coverage corresponds well to the sub-refraction, and the coverage becomes larger as *dN/dh* decreases more. However, the *dN/dh* values observed together with large echo coverage are significantly lower than expected.

This could be attributed to the small number of superrefractive cases and possibly biased AERI retrievals near ground due to erroneous first-guess information. Also, for some scans where a fraction of the area is affected by heavy rain, the precipitation echo coverage could be misclassified as ground echo coverage or the rain could locally affect *dN/dh* while AERI retrieval is still available.

b. Uncertainty in *dN/dh* measurements from soundings

As we mentioned earlier, the proposed radar estimation is representative for the entire domain whereas sounding observations are available at only single locations. This scale mismatch may create some discrepancy in the comparison of the two estimates. Hence, we have quantified the representativeness error of *dN/dh* measurements by using continuous soundings such as those provided by the Tethered Atmospheric Observation System (TAOS; Weckwerth et al. 2004) available nearby the location of AERI. The TAOS provides measurements of atmospheric variables every second from each sensor suspended at certain heights up to 1 km AGL (see Fig. 3-7a). This means that the temporal fluctuation of *dN/dh* observations from the TAOS can be approximatly used to estimate the spatial variability of *dN/dh* over the radar domain using the Taylor "frozen turbulence" hypothesis and the effect of random measurement errors on *dN/dh* estimates combined. Unfortunately, the TAOS worked only for three days during IHOP_2002 (12, 14 and 21 June 2002), and reliable time periods are highly limited due to swaying of the instruments by near-surface winds. We have selected the case of 14 June 2002 shown in Figs. 3-1c and 3-1d.

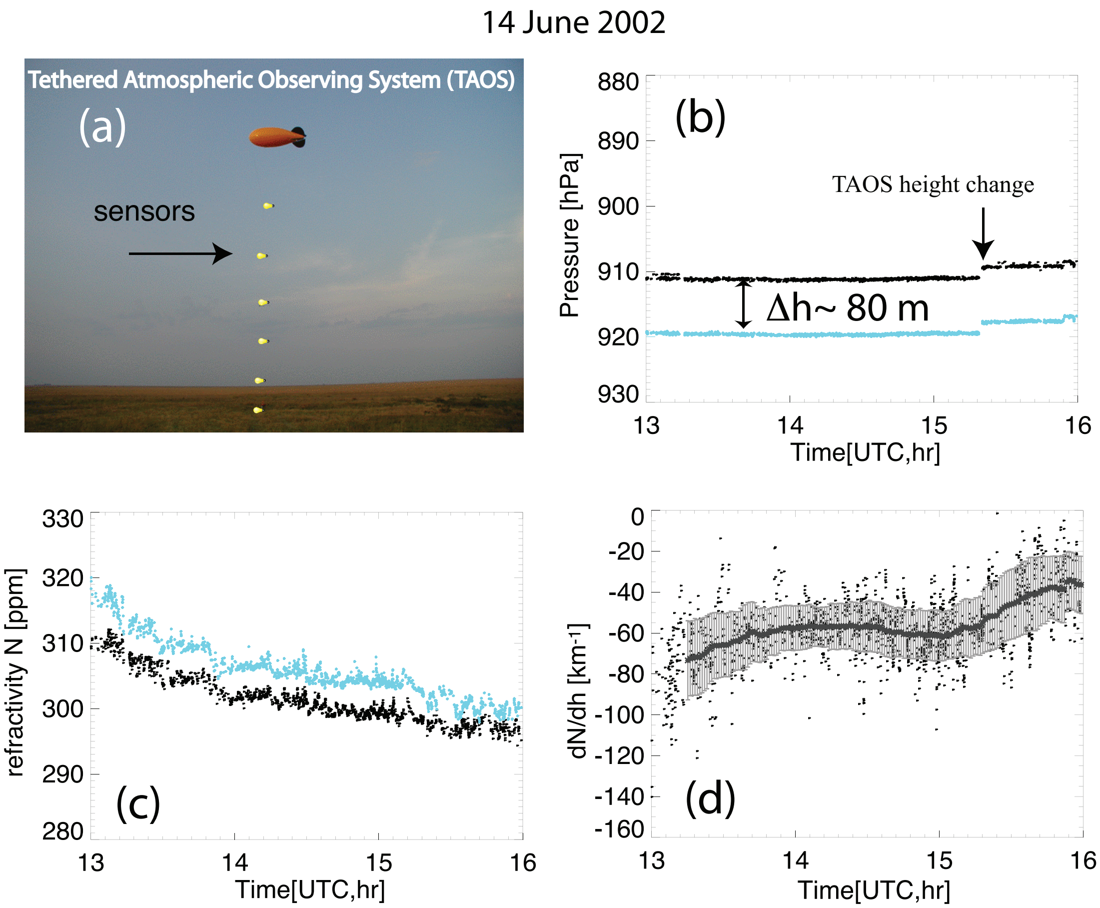

Fig. 3-7: An example of the tethered atmospheric observation system (TAOS) on 14 June during IHOP_2002. a) Picture of TAOS. Next are shown the time series of b) pressure and c) refractivity at two selected levels 80 m apart from each other. d) The *dN/dh* computed between those two levels. Instant-measurements (dots) are averaged over 30 minutes (dark grey line). The grey bars represent the values of the standard deviation.

For a mean wind of 5~10 ms^{-1} and a range of 20~40 km, one can compute a representative value of *dN/dh* over the entire domain by averaging ~ 30 min of data. If we then contrast instantaneous *dN/dh* measurement with 30 min averages, we conclude that the representativeness errors of 20~30 km^{-1} can be expected from soundings for an 80 m height difference (Fig. 3-7d). Although the value of uncertainty is mostly meaningful for the time period chosen above, it still gives us a rough estimate of the representativeness error on point values of *dN/dh*. Furthermore, this case shows the interest of the TAOS or of tower measurements over the radar domain for better uncertainty assessment.

3.5. Some results and discussion

For given radar scans, Fig. 3-8 presents the radar estimates of *dN/dh* resulting from the minimization of (3.6) by comparing them with those from the AERI retrieval. Radar estimates are plotted in black. Because radar estimates are of near-surface *dN/dh* values, the AERI estimates are also taken close to the surface and plotted in closed-triangles (respectively, light color for 80 m and dark color for 170 m AGL). In addition, the mean values for these two heights are plotted in open-triangle. Considering the availability/quality of both estimates, we present the comparison selected for the following periods.

a. Selected cases

- Dry air near the surface (18~22 May 2002)

  Those consecutive days of mid-May had no precipitation and relatively low values of surface N (and of humidity) as indicated by the histogram of refractivity fields retrieved over the radar domain (Fig. 2 in Fabry 2006). Because of similarity in the expected ground echo coverage seen in Fig. 3-6, sub- and normal refraction cases are difficult to distinguish. However, Fig. 3-8a shows the excellent agreement between the *dN/dh* estimated from radar *NIQ* coverage using the method described above and AERI observations; e.g., about 16 km^{-1} RMS difference with the mean values for both AERI heights for the period between 1200 UTC 18 to May and 2400 UTC 22 to May. Also, we can see radar and AERI estimates reproducing the diurnal cycle in this period.

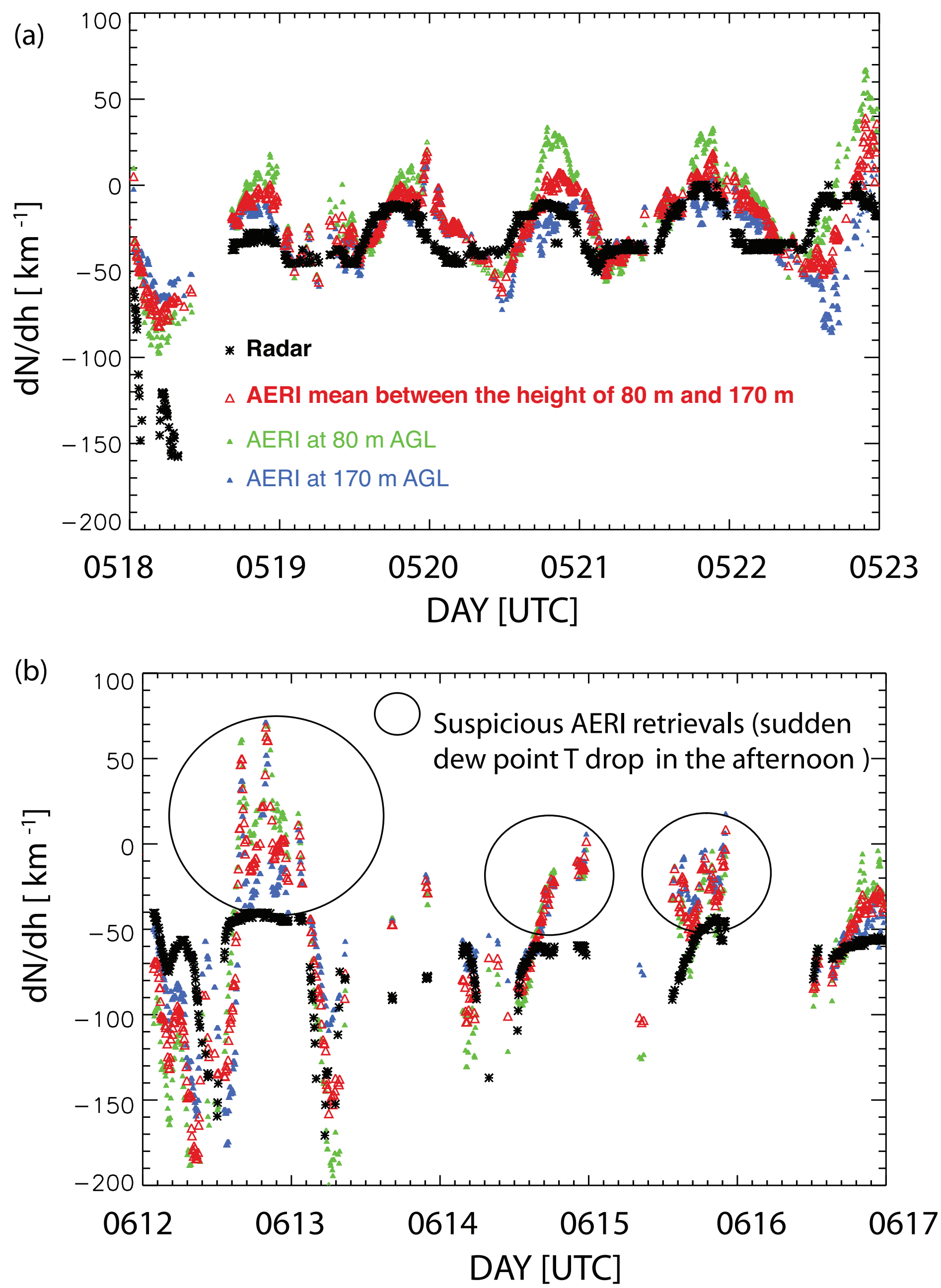

Fig. 3-8: *dN/dh* comparisons between radar estimations and AERI observations on a) 18∼22 May 2002, and b) 12∼16 June 2002. Radar estimation is in black. AERI estimations are at two different levels are in closed-triangles, 80 m AGL in light color and 170 m AGL in dark color, respectively. The mean of these two is in open-triangle.

- Surface moistening (18 May and 12∼16 June 2002)

  In the presence of precipitation outflows, air transported from the Gulf of Mexico, or nocturnal radiative cooling, more negative vertical gradients of refractivity are expected near ground. Hence, greater ground target coverage can be observed by the radar, which helps the performance of estimating propagation conditions as coverage change with *dN/dh* increases in super-refraction conditions (see Fig. 3-6). A good example is the superrefractive cases presented in Fig. 3-1b (14 June 2002) for which there is a good coincidence between radar best estimate and AERI and ISS estimates (see Fig. 3-8b and Fig. 3-9).

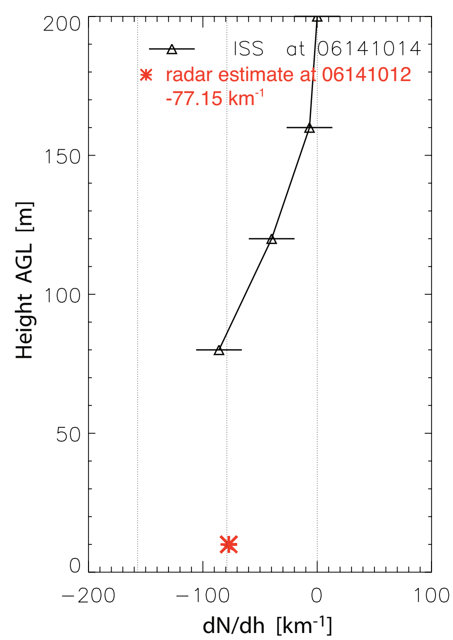

Fig. 3-9: *dN/dh* comparison between the radar estimation and the ISS observation on 1014 UTC, 14 June 2002 seen in Fig. 3-1. The error bars in the profile are based on the result presented in Fig. 3-7d.

However, if the surface is partially affected by rain within the radar domain, the comparison becomes more challenging. For example, Fig. 3-10a shows the reflectivity field observed at 0404 UTC on 18 May 2002 showing locally intense rainfall in the southwestern part of the radar domain. Reflectivity data are clutter-filtered using the default notch filter on S-Pol (Kessinger et al. 1998). Yet, if we look at the terrain maps in these areas, the echoes are certainly contaminated by the ground targets at the 0.0° elevation angle as seen in Fig. 3-10b. On the other hand, it is also possible that the *NIQ* measurements were contaminated by precipitation, though the linear texture of clutter suggests otherwise, and that the radar estimation resulted in almost ducting ($dN/dh < -150$ km^{-1}). Because of such locally biased events, the point AERI retrieval can still be obtained if it is deployed in a non-precipitating area. Hence, this situation can cause difficulty in the comparison and certainly requires better rejection of rainfall echoes contaminating ground clutter *NIQ* values.

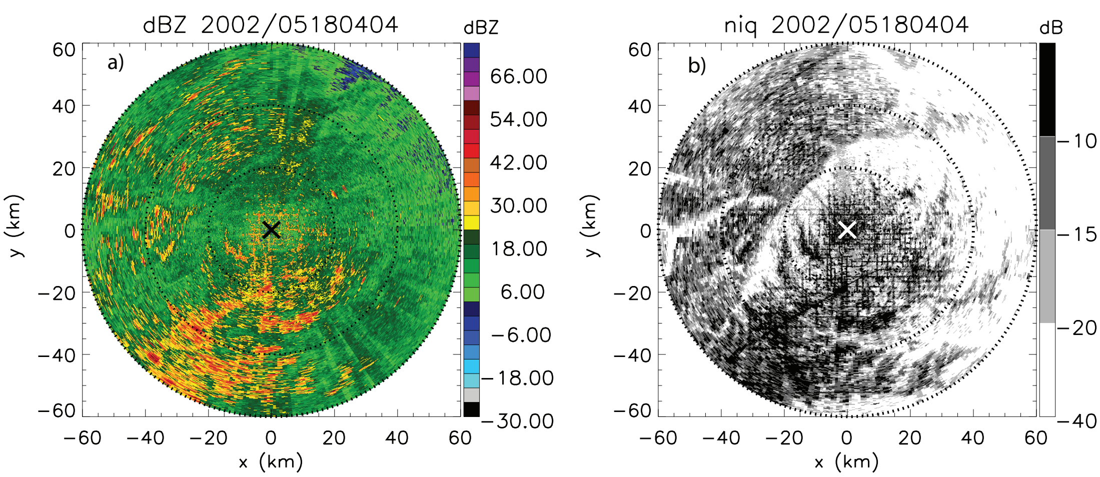

Fig. 3-10: Maps of a) clutter-filtered reflectivity [in dBZ] and b) unfiltered *NIQ* [in dB] over the same study domain on 0404 UTC, 18 May 2002. High reflectivities (above 35 dBZ) occur in regions of moderate to heavy precipitation.

- Mixing in the afternoon

Besides the uncertainty in the interpretation of radar echoes, we have also noticed systematic mismatches in the comparison due to suspicious AERI retrievals. One such mismatch occurred in the afternoon when sudden decreases in low-level estimates of dew-point temperature created peaks of sub-refraction conditions (e.g. in the afternoon on 22 May 2002 and 12-

16 June 2002, indicated with circles in Fig. 3-8b). To verify how realistic these estimates are, we have computed the expected *dN/dh* by differentiating each term in (3.2) with respect to height. If we assume a well-mixed boundary layer (considering, for instance, the frequent case of a windy afternoon in the Southern Great Plains), the lapse rate of water vapor pressure (de/dh) is expected to be very small. For example, given typical values of pressure (920 hPa), water vapor pressure (10 hPa), and temperature lapse rate (9.8 °C km^{-1}), *dN/dh* can be computed as a function of de/dh for different temperatures. Note the grey shade in Fig. 3-11 that the small vertical changes in water vapor pressure (de/dh < +/– 2 hPa km^{-1}) result in the normal conditions no matter what temperature is. In other words, the high peaks of *dN/dh* in AERI data appear suspicious. So, our conclusion is that those data require further quality checks in such periods. In fact, the AERI data have been useful so far to provide boundary layer information away from the surface and have not been much used below a few hundred meters. This suggests that there is a room to extend the usage of AERI data if their uncertainty is better known.

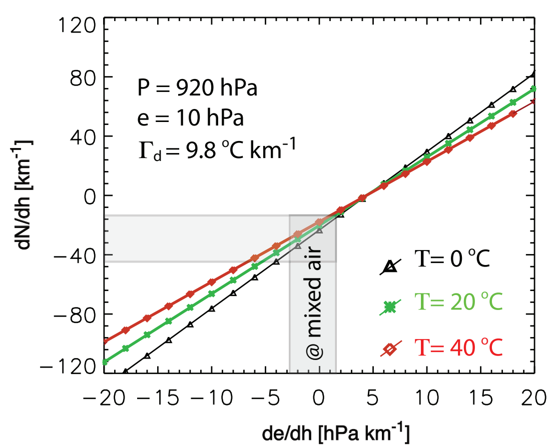

Fig. 3-11: Expected *dN/dh* computed with given conditions of pressure (P; 920 hPa), temperature (T; 0°C, 20°C, and 40°C) and water vapor pressure (e; 10 hPa) assuming a dry-adiabatic lapse rate (Γ_d; 9.8 °Ckm-1). Grey shaded values are expected for well-mixed air, suggesting that values of *dN/dh* around 0~–40 km^{-1}should be observed.

b. Applications of the radar estimated *dN/dh*

Despite several uncertain factors in the estimation and validation, the results show some ability to estimate the propagation conditions by using radar observations. How useful could these be? We have mentioned earlier in the paper that normal refraction conditions are mostly used to compute beam height for radar data quality control and many radar applications. In fact, several studies have used propagation conditions computed with real soundings (Steiner and Smith 2002; Bech et al. 2007). However, very low-level conditions have not been really considered. Because our method provides near-ground estimates of *dN/dh*, we have evaluated how sensitive the beam height is to small changes in near-ground *dN/dh.* This is done by computing the difference (or error) between the beam height determined by true soundings and those found by using four different *dN/dh* soundings approximations: i) a constant profile of normal propagation conditions ($dN/dh = -40$ km^{-1}), ii) the true average *dN/dh* between the surface and 1 km AGL (ITU 2003) and $dN/dh = -40$ km^{-1} above, iii) the true average *dN/dh* for the bottom 500 m AGL (Steiner and Smith 2002) and $dN/dh = -40$ km^{-1} above, and iv) a modified sounding using the observed *dN/dh* value up to 100 m and $dN/dh = -40$ km^{-1} above. The last modified profile was tested because we could replace the low-level *dN/dh* values by what we are estimating with the proposed method using radar observations.

Figures 3-12 and 3-13 present the results at the 0.0° and the 2.5° elevation angles respectively. We have chosen low–level soundings from ISS measured on 14 June during IHOP_2002 under conditions of a) super-refraction, b) normal-refraction, and c) sub-refraction. We computed the beam height differences by subtracting the beam heights obtained with true sounding from those with the four *dN/dh* approaches described above. From Fig. 3-12, independently of the real propagation conditions, the dash-dotted line shows the smallest errors in simulated beam heights compared to those obtained with the true sounding. This certainly shows the value of better knowing the low-level propagation conditions compared to using the average value of *dN/dh* over a deeper layer at low-elevation angle.

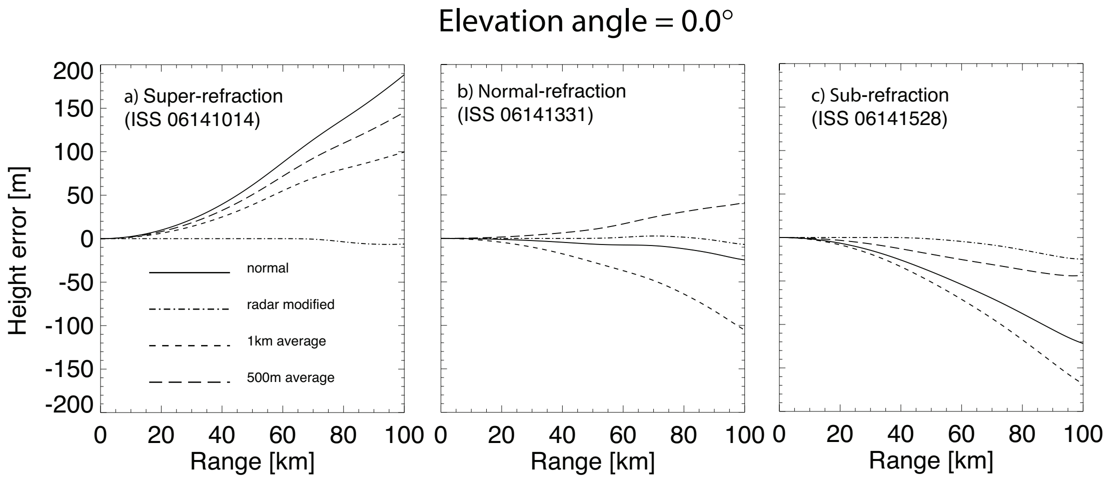

Fig. 3-12: Absolute center-beam height differences (errors) at the 0.0° elevation angle between the beam height computed with true soundings selected from ISS measurements and those computed with the following assumed *dN/dh* profiles: a normal condition of $dN/dh = -40$ km^{-1} (solid line); a modified sounding by replacing the normal condition below 100 m by the true sounding value that could be estimated by radar (dashed and dotted line); one where the bottom 1 km *dN/dh* is replaced by the true average over that layer of *dN/dh* (short dashed line), one where the bottom 500 m *dN/dh* is replaced by the true average over that layer of *dN/dh* (long dashed line). Three ISS soundings were considered: a) at 1014 UTC (super-refraction), b) 1331 UTC (normal refraction), c) 1528 UTC (sub-refraction) on 14 June 2002.

On the other hand, at the high elevation angle as shown in Fig. 3-13, the errors are generally smaller and similar for the four conditions. The dashed dotted line (radar modified) is almost superimposed with the long dashed line (500 m average) for the super-refraction and with solid lines (normal) for both normal and sub-refraction conditions. Because these results were from only one sounding for each propagation condition, we performed a similar analysis for additional soundings. Because the ISS soundings observed a very small sample of super refraction/ducting conditions, we have used sounding measurements collected by the ARM (Atmospheric Radiation Measurement) Central Facility near Lamont, Oklahoma, also during IHOP_2002. Although this site is out of the S-Pol radar domain, more frequent radio-soundings were available during the experiment, four times a day or even more as well as at regular time intervals.

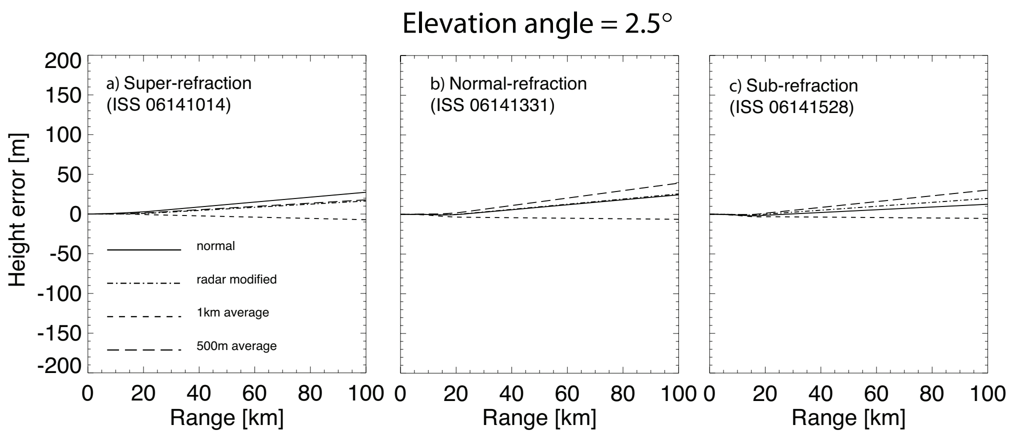

Fig. 3-13: As in Fig. 3-12 but at the 2.5° elevation angle.

As a result, Figs. 3-14 and 3-15 show statistical mean (in black lines) of center beam height errors as a function of range at the 0.0° and the 2.5° elevation angles respectively. At different times, i.e. a) 05 UTC, b) 11UTC, c) 17 UTC, and d) 23 UTC), between 22 to 28 soundings were available. For each time, the upper right corner of each panel shows the frequency of *dN/dh* values with bars. Although the total number of samples is still small, we can see that near surface ducting occurred more frequently at 05 UTC and 11 UTC than at 17 UTC and 23 UTC. This is because the location would likely experience nocturnal storm outflows around 05 UTC or radiative cooling. We chose not to combine cases by their propagation conditions given the small sample size for all anomalous conditions.

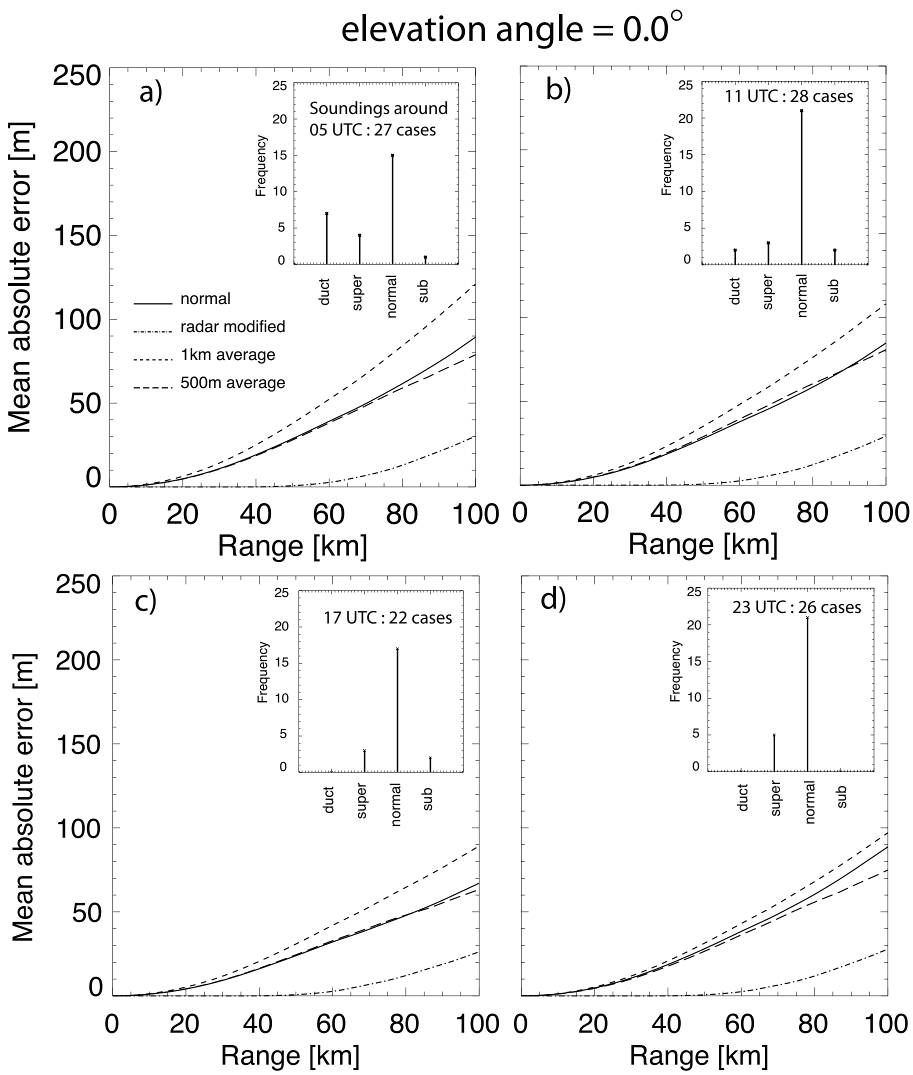

Fig. 3-14: Mean absolute error (black lines) of the center beam height at the 0.0° elevation angle as a function of range based on ARM soundings sampled four times a day -(a) 05, (b) 11, (c) 17, and (d) 23 UTC - at Lamont during IHOP_2002. In inset, a frequency distribution of the soundings providing low-level propagation conditions is shown.

However, we can clearly see the impact of near ground propagation on beam height errors; i.e., the smallest errors are shown with the dash-dotted lines at 0.0° elevation angle. The largest error of the beam heights at 100 km away from the radar in range is about 100 m when an average *dN/dh* is computed between 1km and near ground (the short-dashed line). Is this absolute error significant? The answer should be dependent on the application. One thing, however, is clear:

knowledge of low-level propagation conditions (the goal of this study -the dash-dotted lines-) would result in a more than 50 % reduction of the errors in beam height compared with the other methods for low elevation angles. Meanwhile, the beam height errors at 2.5° elevation angle are not as large as those at the 0.0° elevation angle (Fig. 3-15).

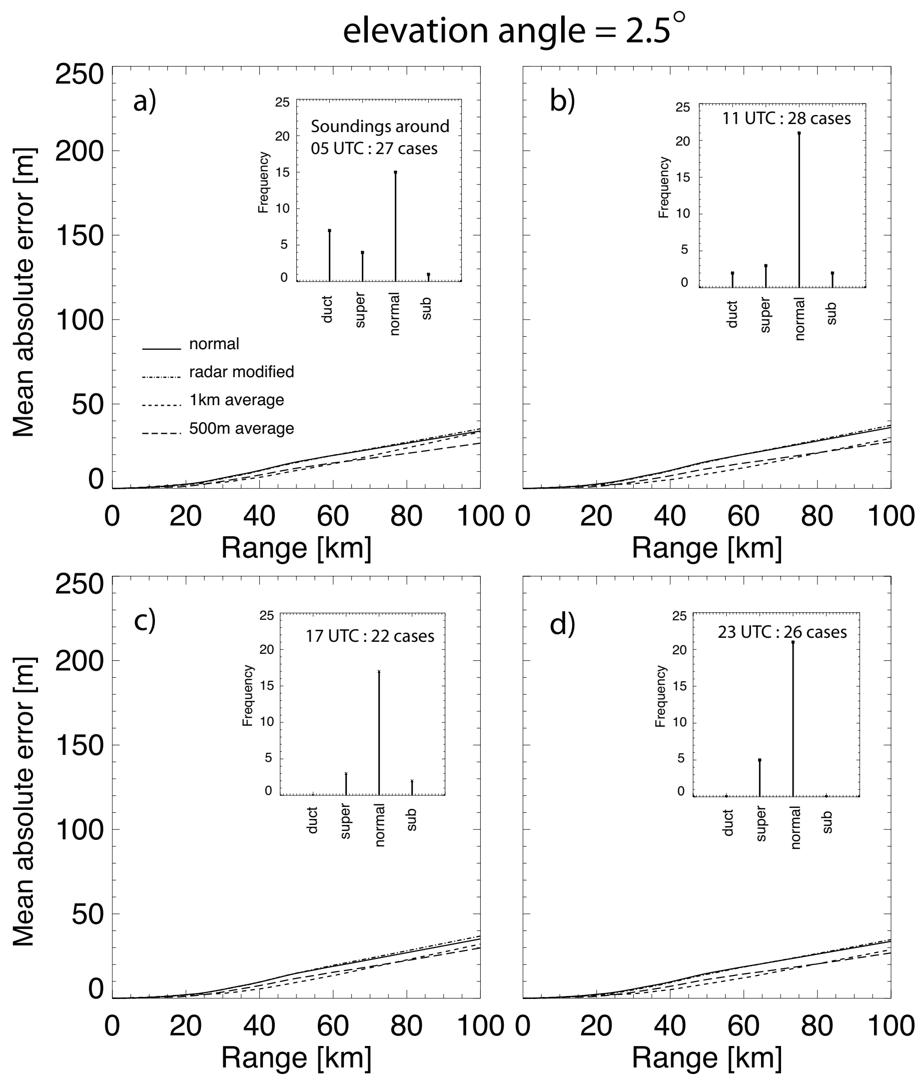

Fig. 3-15: As in Fig. 3-14 but at the 2.5° elevation angle.

At high elevation angles, the influence of low-level propagation conditions on the beam height errors was very small. This result is not surprising, because the beam trajectory will be elevated before they are influenced by the propagation conditions within 100 m, resulting in much less chance to bend toward the ground. In fact, the results are practically the same as those for normal conditions. Contrarily, using *dN/dh* averages over deeper layer (500 m and 1 km), there is an improvement in computed beam heights and thus the reduced errors with respect to the true propagation conditions.

3.6. Conclusion

Propagation conditions (*dN/dh*) play an important role in quality control of scanning radar observations and their final applications in precipitation estimation and forecasting. The echo intensity map returned from ground targets shows coverage changes associated with the changes of low-level *dN/dh.* At the same time, it is possible to simulate the map of detectable ground target heights as a function of *dN/dh* based on ray tracing. In the present work, we have compared the coverage of high *NIQ* observations with *dN/dh* estimated from soundings available during IHOP_2002. This comparison suggests that ground echo coverage increases consistently with larger negative values of the gradient of refractivity. Based on that, this study proposed a method to estimate low-level *dN/dh* values within the radar domain (~ 60 km in range) based on the observation of *NIQ*.

Several difficulties in the verification of the results were found due to 1) a limited number of soundings compared to the number of radar scans, 2) the representativeness of radar estimates of *dN/dh* (obtained based on area matching) compared with point soundings observations, 3) unclear separation of radar ground echoes from weather echoes in the presence of anomalous propagations due to precipitation outflows. However, the method showed ability in capturing the near-ground gradient of refractivity at low-level elevation angles. We also showed how retrieving such information could help better predict the height sampled by radar at all ranges.

Acknowledgements

This work was made possible thanks to the support of the Canadian Foundation for Climate and Atmospheric Sciences. The authors thank Prof. Isztar Zawadzki for his fundamental and critical questions on the subject. We are very grateful to Dr. Marc Berenguer for his valuable comments and insightful review of the first manuscript. Also, the review of the manuscript by Dr. Radha Krishna was helpful.

CHAPTER 4

Discussion

In this thesis, near-ground scanning radar measurements (in particular, returns from ground targets) were used for the estimation of the structure of near-surface refractivity and its errors extended the work of Fabry et al. (1997). Although the previous chapters contain their own conclusions of the topics above, the following will review briefly each topic and emphasize limitations and benefits for perspective future work.

The original version of the radar refractivity retrieval algorithm is based on the phase differences between two times [i.e. between the time of interest and a reference time that is chosen with a uniform refractivity field within the domain; see more detail in Park (2004)] measured from stationary ground targets such as power lines, railways or the terrain. These phase difference fields inform us about refraction conditions but are noisy due to i) all kinds of natural sources along the beam path (e.g., complexity of the terrain, properties of the targets, propagation conditions, precipitation, vegetation sway etc.) and ii) phase aliasing (i.e., phases are measured-moduleo-2π). To mitigate the noisiness of phase data, the retrieval algorithm assumes a number of idealized conditions (such as the reference homogenous field of refractivity and no height difference between the radar and the targets), which can yield errors in the retrieved refractivity. Therefore, this dissertation first investigated the sources of error causing noisiness in the phase difference field for improving the quality of the retrievals.

Considering complex terrain not flat terrain assumed in the refractivity algorithm, some noisiness in the phase differences was expected to appear by the enhanced variation of beam trajectory due to differences in target heights and propagation conditions. In fact, based on terrain heights, ground echo intensity observations, and available soundings, the target height variability coupled with the propagation conditions could be practically characterized. Moreover, these characterized factors could be conveniently simulated as additional terms to the original algorithm and examined its effect on the variability of phase difference fields. Also, in this way, the validation was straightforward by comparison with real phase measurements.

The comparisons were performed in both small (20 km by 20 km) and large (60 km by 60 km) domain sizes. However, we presented the results for the smaller domain size only. This is because we believed that the better quality of ground target should be expected in there given the high density of ground targets hit by the radar. However, the phase variability from the simulations was significantly smaller than those from the observations, which suggested that the simulated factors were not the dominant cause of the phase noisiness. Therefore, even if we expected and showed some increase in phase variability at further range due to changes of propagation conditions, because the simulation failed to reproduce results at near-range, study of far-range properties would not yield additional insights. From these results, two questions arose: i) How realistic was the statistical characterization of ground targets? ii) Were propagation conditions properly provided?

The importance of using phase returns from "stationary" targets has been already emphasized in the original refractivity algorithm. Hence, the selection of such targets have been carefully done based on two indices assigned at each radar bin according to Fabry (2004):

- Target reliability index map: It is generated at calibration time (reference time) and involves the signal to noise ratio (SNR) to remove side lobe contamination and the phase coherence (scan- to-scan phase differences) to filter moving targets such as vegetation sway.

- Target quality index map: It is generated in real-time to accompany the target reliability index map. It highlights the radar bins with high SNR, near-zero Doppler velocity, as well as narrow spectrum width.

Furthermore, both indices have been also key elements of independently developed recent versions of the refractivity retrieval algorithms applied to radar networks (Hao et al. 2006; Fritz and Chandrasekar 2009). Despite the usefulness of the target reliability index and the target quality index in the algorithms and the target characterization presented in this thesis, these did not always guarantee the existence of targets and the absence of movement. For instance, the latter could be a critical factor to cause unsatisfactory performance of the phase simulation.

Propagation conditions (*dN/dh*), on the other hand, were obtained from radiosonde and AERI soundings. Although various sources of soundings during IHOP_2002 were useful, their availability was still limited due to measurement uncertainty especially near ground on top of the coarse resolution of data in space and time. This is why the results were presented with selected cases.

Besides the quality of selected ground targets and propagation conditions, a number of other factors not considered in the simulation constitute enough degrees of freedom to completely explain the noise observed in phase measurements. In a way, thus, the complexity of the problem did not permit to attain the attempt of quantifying the errors in the refractivity retrieval based on the factors analyzed. On conclusion, the improvement of the retrieval should take a different direction, perhaps to a better characterization of ground targets, and it is left as a main question from the work of Chapter 2.

Secondly, a new method is developed for estimating near-surface vertical gradient of refractivity (*dN/dh*). Radar echo intensities measured at low elevations reflect the detection of ground targets, and the coverage of high intensity values changes depending on the propagation conditions. At the same time, knowing the orography of the domain, one can simulate the height ground targets must be to be visible with the radar as a function of *dN/dh*. This approach is similar to others done by algorithms for beam blockage mitigation (Delrieu et al. 1995; Kucera et al. 2004) that, however, usually lack of any knowledge on *dN/dh*.

To amend the information of *dN/dh*, this thesis work compared the coverage of visible ground targets varying with different *dN/dh* to the coverage of high intensity of ground echo observation. As a result, the best match could determine a value of *dN/dh* representative over the radar domain. Some difficulties were expected in the evaluation process with soundings due to measurement uncertainties. Nevertheless, during the entire period of IHOP_2002, the comparison of radar *dN/dh* estimates with near surface *dN/dh* estimates from the various sounding instruments demonstrated that the developed technique showed certain skill.

Such knowledge of propagation conditions near surface could improve the estimation of the radar beam height with respect to the usual computations that assume normal propagation conditions: it was shown that the beam height errors reduced up to 50 % at ranges of 100 km in superrefractive cases.

In perspective of the horizontal retrieval of *N* representative for a layer of 200 to 300 m above the ground, the radar estimated *dN/dh* may reveal additional small-scale variation of refractivity structure within the layer. Therefore, it could prove useful to improve the assessment of errors in the refractivity retrieval seen in Chapter 2. In this dissertation was no further analysis performed to assess the impact of such information on the study of convection initiation or its assimilation in numerical weather prediction models. However, if one is interested in these questions, one should remember that improved knowledge of this low-level structure will not be sufficient because we generally need information on the structure of the whole boundary layer for the analysis of convection initiation (e.g., Fabry 2006) and for data assimilation (Fabry and Sun 2010).

Finally, it is worth emphasizing that the performance of both horizontal refractivity and its vertical gradient estimates highly depend on the presence and quality of ground targets within the radar domain. In this sense, both techniques will fail in the absence ground targets (e.g., radars covering maritime domains). Although the identification of reliable targets in low elevation PPIs is still a challenge, recent improvements on radar signal processing or on the use of polarimetric radars (e.g. see Hubbert et al. 2009; Moisseev and Chandrasekar 2009) have shown potential for such a task.

Bibliography

Ahrens, C. D., 2000: Meteorology Today. 6th Edition. Brooks/Cole, 528 pp.

Atkinson, B. W. and M. Zhu, 2005: Radar-duct and boundary-layer characteristics over the Gulf area. Quart. J. Roy. Meteor. Soc., 131, 1923-1953.

Babin, S. M., 1995: A case study of subrefractive conditions at Wallops island, Virginia. *J. Appl. Meteor.*, **34,** 1028-1038.

______ and G. D. Dockery, 2002: LKB-based evaporation duct model comparison with buoy data. J. Appl. Meteor., 41, 434-446.

Barclay, L. W., 2003: Propagation of radiowaves. 2nd Edition. The Institution of Electrical Engineers, 460 pp.

Battan, L. J., 1973: Radar observations of the atmosphere. Univ. of Chicago Press, Chicago, III, 324 pp.

Bean, B. R. and E. J. Dutton, 1968: Radio Meteorology. National Bureau of Standards Monogr., No.92, National Bureau of Standards, 435 pp.

Bech, J., B. Codina, J. Lorente, and D. Bebbington, 2003: The sensitivity of single polarization weather radar beam blockage correction to variability in the vertical refractivity gradient. J. Atmos. Oceanic Technol., 20, 845-855.

_____, U. Gjertsen, and G. Haase, 2007: Modeling weather radar beam propagation and topographical blockage at northern high latitudes. Quart. J. Roy. Meteor. Soc., 133, 1191-1204.

Bellon, A., G. W. Lee, A. Kilambi, and I. Zawadzki, 2007: Real-time comparison of VPR-corrected daily rainfall estimates with a gauge mesonet. J. Appl. Meteor. and Climatology., 46, 726-741.

Berenguer, M., D. Sempere-Torres, C. Corral, and R. Sánchez-Diezma, 2006: A fuzzy logic technique for identifying nonprecipitating echoes in radar scans. J. Atmos. Oceanic Technol., 23, 1157-1180.

__________ and I. Zawadzki, 2008: A study of the error covariance matrix of radar rainfall estimation in stratiform rain. Wea. Forecasting, 23, 1085-1101.

Bevington, P. R, 1969: Data reduction and error analysis for the physical sciences. McGraw- Hill, Inc, 336 pp.

Bianco, L., D. Cimini, and R. Ware, 2005: Combining microwave radiometer and wind profiler radar measurements for high-resolution atmospheric humidity profiling. J. Atmos. Oceanic Technol., 22, 949-965.

Briggs, J., 2004: Target detection by marine radar. The Institution of Electrical Engineers, London, UK, pp. 652.

Burgess, D. W. and L. R. Lemon, 1990: Severe thunderstorm detection by radar. Radar in Meteorology (D. Atlas, Ed.), Amer. Meteor. Soc., 619-647.

Businger, S., and Coauthors, 1996: The promise of GPS in atmospheric monitoring. Bull. Amer. Meteor. Soc., 77, 5-18.

Caya, A., S. Laroche, I. Zawadzki, and T. Montmerle, 2002: Using single-Doppler data to obtain a mesoscale environmental field. J. Atmos. Oceanic Technol., 19, 21-36.

Cheong, B. L., R. Palmer, V. Chandrasekar and F. Junyent, Real-time Refractivity Retrieval Using the Magnetron-based CASA X-band Radar Network During the Spring 2008 Campaign. International Geoscience & Remote Sensing Symposium, Boston, Massachusetts, July 6-11, 2008.

Cho, Y.-H., G. W. Lee, K.-E. Kim, and I. Zawadzki, 2006: Identification and removal of ground echoes and anomalous propagation using the characteristics of radar echoes. J. Atmos. Oceanic Technol., 23, 1206-1222.

Chung, K-S., I. Zawadzki, M. K. Yau, and L. Fillion, 2009. Short-term forecasting of a midlatitude convective storm by the assimilation of single Doppler radar observations. Monthly Weather Review, 137, 4115- 4135.

Collier C. G., 1996: Applications of weather radar systems. John Wiley and Sons, 2nd Edition, New York, 390 pp.

Crook, N. A., 1996: Sensitivity of convection initiation to low-level thermodynamics fields. Mon. Wea. Rev., 124, 1767-1785.

Delrieu, G., J. D. Creutin, and H. Andrieu, 1995: Simulation of radar mountain returns using a digitized terrain model. J. Atmos. Oceanic Technol., 12, 1038-1049.

Doviak, R. J. and D. S. Zrnić, 1993: Doppler Radar and Weather Observations. 2nd Edition, Academy Press, Inc, 562 pp.

Fabry, F., C. Frush, I. Zawadzki, and A. Kilambi, 1997: On the extraction of near-surface index of refraction using radar phase measurements from ground targets. J. Atmos. Oceanic Technol., 14, 978-987.

_____, and C. Creese, 1999: If fine lines fail, try ground targets. 29th Int. Conf. on Radar Meteorology, Montreal, QC, Canada, Amer. Meteor. Soc., 21-23.

_____, and C. Pettet, 2002: A primer to the inter- pretation of refractivity imagery during IHOP 2002. IHOP 2002 Refractivity Manual. [Available at http://www.eol.ucar.edu/dir_off/projects/2002/IHOPrefractivityManual.pdf]

_____, and R. J. Keeler, 2003: Innovative signal utilization and processing. Radar and Atmospheric Science: A Collection of Essays in Honor of David Atlas, R. M. Wakimoto and R. C. Srivastava, Eds., Amer. Meteor. Soc., 199-214.

_____, 2004: Meteorological value of ground target measurements by radar. J. Atmos. Ocean. Technol., 21, 560-573.

_____, 2005: Peeping through the keyhole at the mesoscale variability of humidity: some IHOP_2002 observations and future challenges of radar refractivity mapping. 32nd Int. Conf. on Radar Meteorology, Albuquerque, New Mexico, USA, Amer.Meteor.Soc., J6J.1, (CD-ROM).

_____, 2006: The spatial structure of moisture near the surface: Project-long characterization. Mon. Wea. Rev., 134, 79-91.

_____, and J. Sun, 2010: For how long should what data be assimilated for the mesoscale forecasting of convection and why? Part I: On the propagation of initial condition errors and their implications for data assimilation. Mon. Wea. Rev., 138, 242-255.

Feltz, W. F., W. L. Smith, H. B. Howell, R. O. Knuteson, H. Woolf, and H. E. Revercomb, 2003: Near-continuous profiling of temperature, moisture, and atmospheric stability using the Atmospheric Emitted Radiance Interferometer (AERI). J. Applied Meteor., 42, 584-597.

Fornasiero, A., P. P. Alberoni, and J. Bech, 2006: Statistical analysis and modeling of weather radar beam propagation conditions in the Po Valley (Italy). Nat. Hazards Earth Syst. Sci., 6, 303-314.

Fritz, J. and V. Chandrasekar, 2009: Implementation and analysis of networked radar refractivity retrieval. J. Atmos. Ocean Technol., 26, 2123-2135.

Ge, G., J. Gao, K. Brewster, and M. Xue, 2010: Impacts of Beam Broadening and Earth Curvature on Storm-Scale 3D Variational Data Assimilation of Radial Velocity with Two Doppler Radars. J. Atmos. Ocean Technol., 27, 617-636.

Germann, U., G. Galli, M. Boscacci, and M. Bolliger, 2006: Radar precipitation measurement in a mountainous region. Quart. J. Roy. Meteor. Soc., 132, 1669-1692.

Gerstoft, P., L. T. Rodgers, W. S. Hodgkiss and L. J. Wagner, 2003: Refractivity estimation using multiple elevation angles. IEEE Oceanic Eng., 28, 513-525.

Gossard, E. E., D.E. Wolfe, K. P. Moran, R. A. Paulus, K. D. Anderson, and L. T. Rogers, 1998: Measurement of clear-air gradients and turbulence properties with radar wind profiles. J. Atmos. Oceanic Technol., 15, 321-342.

__________, D. E. Wolfe, and B. B. Stankov, 1999: Measurement of humidity profiles in the atmosphere by the Global Positioning System and radar wind profilers. J. Atmos. Oceanic Technol., 16, 156-164.

Guo, Y.-R., Y.-H. Kuo, J. Dudhia, D. Parsons, and C. Rocken, 2000: Four-Dimensional Varia- tional Data Assimilation of Heterogeneous Mesoscale Observations for a Strong Convective Case. Mon. Wea. Rev., 128, 618-643.

Hao, Y. D. Goeckel, R. Janaswamy, and S. Frasier, 2006: Surface refractive index field estimation from multiple radars. Radio Sci., 41, RS3003, doi:10.1029/2005RS003288.

Heinselman, P. L., B. L. Cheong, R. D. Palmer, D. Bodine, K. Hondl, 2009: Radar refractivity retrievals from KTLX: Insights into operational benefits and limitations. Wea. Forecasting, 24, 1345-1361.

Hubbert, J. C., M. Dixon, S. M. Ellis, and G. Meymaris, 2009: Weather radar ground clutter. Part I: Identification, modeling, and simulation. J. Atmos. Oceanic Technol., 26, 1165-1180.

ITU, 2003: 'The radio refractive index: its formula and refractivity data', Recommendation. International Telecommunication Union: 453-459.

Jorgensen D. P., and T. M. Weckwerth, 2003: Forcing and organization of convective systems. Radar and Atmospheric Science: A Collection of Essays in Honor of David Atlas, Meteor. Monogr. No. 52, Amer. Meteor. Soc., 75-104.

Kalbfleisch, J. G., 1985: Probability and Statistical Inference, Vol. 1: Probability. 2nd Edition, Springer-Verlag New York Inc., 343 pp.

Keeler, R. J., J. Lutz, and J. Vivekanandan, 2000: S-Pol: NCAR's Polarimetric Doppler Research Radar. Proceedings of the International Geoscience and Remote Sensing Symposium, IEEE, Honolulu, Hawaii, 1570-1573.

Kessinger, C., S. Ellis, J. V. Andel, D. Ferraro, and R. J. Keeler, 1998: NEXRAD data quality optimization. FY98 annual report, WSR-88D Operational Support Facility NEXRAD Data Quality Optimization.

Konrad, T. G. and F. L. Robison, 1972: Simultaneous measurements of radar reflectivity and refractive index spectra in clear air convection. J. Applied Meteor., 11, 1114-1119.

Kucera, P. A., W. F. Krajewski, and C. B. Young, 2004: Radar beam occultation studies using GIS and DEM technology: an example study of Guam. J. Atmos. Ocean Technol., 21, 995-1006.

Kuo, Y.-H., T. K. Wee, S. Sokolovskiy, C. Rocken, W. Schreiner, D. Hunt, and R. A. Anthes, 2004: Inversion and error estimation of GPS radio occultation data. J. Meteor. Soc. Japan, 82B, 507–531.

Laroche, S., and I. Zawadzki, 1994: A variational analysis method for retrieval of three-dimensional wind field from single–Doppler radar data. J. Atmos. Sci., 51, 2664–2682.

Lhermitte, R. 2002: Centimeter & Millimeter Wavelength Radars in Meteorology. Lhermitte Publications, 548 pp.

Moisseev, D. N. and V. Chandrasekar, 2009: Polarimetric spectral filter for adaptive clutter and noise suppression. J. Atmos. Oceanic Technol., 26, 215-228.

Montmerle, T., A. Caya, I. Zawadski, 2002: Short term numerical forecasting of a shallow storm complex using bi-static and single Doppler radar data. Weather and Forecasting, 17, 1211-1225.

Moszkowicz, S., G. J. Ciach, and W. F. Krajewski, 1994: Statistical detection of anomalous propagation in radar reflectivity patterns. J. Atmos. Oceanic Technol., 11, 1026-1034.

Nicol, J., K. Bartholemew, and A. Illingworth, 2009: A technique for deriving the humidity of air close to the surface using operational rain radar. Proceedings of the 8th International Symposium on Tropospheric Profiling, ISBN 978-90-6960-233-2.

Parent du Chatelet, J. and C. Boudjabi, 2008: A new formulation for signal reflected from a target using a magnetron radar. ERAD 2008 - The 5th European conf. on radar in Meteorology and Hydrology, Helsinki, Finland, 30 June-4 July 2008.

Park, S., 2004: *Water vapor estimation using near-surface radar refractivity during IHOP_2002*, M.Sc thesis, McGill University, 77 pp. Available at the following website: http://digitool.Library.McGill.CA:80/R/89YCIP8D2LNBABALX7415LQGYREUSNEGR6LE1M1NDUHSME9M1A-02070?func=results-jump-full&set_entry=000045&set_number=002227&base=GEN01-MCG02

Park, S. and F. Fabry, 2010: Simulation and Interpretation of the phase data used by radar refractivity retrieval algorithm. Accepted to J. Atmos. Oceanic Technol., **27**, 1286-1301.

Parsons, D. B., and Coauthors, 1994: The integrated sounding system: Description and preliminary observations from TOGA COARE. Bull. Amer. Meteor. Soc., 75, 553–567.

Pellarin T., G. Delrieu, G. M. Saulnier, H. Andrieu, B. Vignal and J. D. Creutin, 2002: Hydrologic visibility of weather radar systems operating in mountainous regions: Case study for the Ardèche catchment (France). J. Hydrometeor, 3, 539-555.

Press, W. H., S. A. Teukolsky, W. T. Vetterling, B. P. Flannery, 1999: Numerical Recipes, The Art of Scientific Computing, 2nd Edition. Cambridge University Press, 994 pp.

Roberts, R. D., F. Fabry, P. C. Kennedy, E. Nelson, J. Wilson, N. Rehak, J. Fritz, V. Chandrasekar, J. Braun, J. Sun, S. Ellis, S. Reising, T. Crum, L. Mooney, R. Palmer, T. Weckwerth, and S. Padmanabhan, 2008: REFRACTT-2006: Real-time retrieval of high-resolution low-level moisture fields from operational NEXRAD and research radars. Bull. Amer. Meteor. Soc., 89, 1535–1538.

Rogers, R. and M. Yau, 1989: A Short Course in Cloud Physics, 3rd Edition. Pergaon Press, Oxford, 293 pp.

Sauvageot, H., 1992: Radar Meteorology. Artech House, 366 pp.

Sizun, H., 2005: Radio Wave Propagation for Telecommunication Applications, Springer, Verlag Berlin Heidelberg, 414 pp.

Skolnik, M. 2001: Introduction to Radar Systems, 3rd Edition, McGraw-Hill, 772 pp.

Steiner, M. and J. A. Smith, 2002: Use of three-dimensional reflectivity structure for automated detection and removal of nonprecipitating echoes in radar data. J. Atmos. Oceanic Technol., 19, 673-686.

Sun, J., and A. Crook, 1997: Dynamical and microphysical retrieval from Doppler radar observations using a cloud model and its adjoint. Part I: Model development and simulated data experiments. J. Atmos. Sci., 54, 1642–1661.

Tabary, P., 2007: The new French operational radar rainfall product. Part I: Methodology. Wea. Forecasting, 22, 393-408.

Vasiloff, S. V., and Coauthors 2007: Improving QPE and very short term QPF: An initiative for a community-wide integrated approach. Bull. Amer. Meteor. Soc., 88, 1899-1911.

Wakimoto, R. M. and H. V. Murphey, 2009: Analysis of a dryline during IHOP: Implications for convection initiation. Mon. Wea. Rev., 137, 912-936.

Weber, R., 1997: Estimators for the Standard Deviation of Horizontal Wind Direction, J. Applied Meteor., 36, 1403-1415.

Weckwerth, T. M., V. Wulfmeyer, R. M. Wakimoto, R. M. Hardesty, J. W. Wilson, and R. M. Banta, 1999: NCAR–NOAA lower-tropospheric water vapor workshop. Bull. Amer. Meteor. Soc, 80, 2339-2357.

________, 2000: The effect of small-scale moisture variability on thunderstorm initiation. Mon. Wea. Rev., 128, 4017-4030.

________, D. B. Parsons, S. E. Koch, J. A. Moore, M. A. LeMone, B. B. Demoz, C. Flamant, B. Geerts, J. Wang, and W. F. Feltz, 2004: An overview of the International H_2O Project (IHOP_2002) and some preliminary highlights. Bull. Amer. Meteor. Soc., 85, 253-277.

________, C. R. Pettet, F. Fabry, S. Park, M. A. LeMone, and J.W. Wilson, 2005: Radar refractivity retrieval: validation and application to short-term forecasting. J. Appl. Meteoro., 44, 285–300.

________, and D. B. Parsons, 2006: A review of convection initiation and motivation for IHOP_2002. Mon. Wea. Rev., 134, 5-22.

Wilson, J. W. and R. D. Roberts, 2006: Summary of convective storm initiation and evolution during IHOP: Observational and modeling perspective. Mon. Wea. Rev., 134, 23–47.